

**Towards understanding the dissolution mechanism
of clay minerals – An ab initio simulations study**

Inauguraldissertation
der Philosophisch-naturwissenschaftlichen Fakultät
der Universität Bern

vorgelegt von

René Jens Schliemann

aus Deutschland

Leiter der Arbeit:

Prof. Dr. Sergey V. Churakov
(Institut für Geologie, Universität Bern)



This work is licensed under the a Creative Commons Attribution-Non-Commercial-No derivative works 4.0. To see the license go to <https://creativecommons.org/licenses/by-nc-nd/4.0/>.

**Towards understanding the dissolution mechanism of clay minerals
– An ab initio simulations study**

Inauguraldissertation
der Philosophisch-naturwissenschaftlichen Fakultät
der Universität Bern

vorgelegt von

René Jens Schliemann

aus Deutschland

Leiterin/Leiter/LeiterInnen der Arbeit:

Prof. Dr. Sergey V. Churakov
(Institut für Geologie, Universität Bern)

Von der Philosophisch-naturwissenschaftlichen Fakultät angenommen.

Bern, den 16.12.2022

Der Dekan

Prof. Dr. Marco Herwegh

Abstract

Clay minerals can be abundantly found in sediments, soils and argillaceous rock formations. Together with their sorption capability, pH-buffering effects and other properties they dominate the geochemistry of aforementioned soils and subsurface formations. Many applications of clay minerals rely on their specific reactivity or ability to retain transition and heavy metals through sorption, surface complexation or even incorporation. The dissolution of such structures would lead to the release of potentially hazardous elements back into the environment, which is why the knowledge of the dissolution mechanism is of utter importance to make predictions of the retention time of detained elements.

Batch experiments to determine dissolution rates in different temperature and pH conditions revealed an initial incongruent dissolution while long term observations show stoichiometric dissolution for different types of clay minerals. Quantum mechanical simulations offer the possibility to investigate phenomena at the atomic scale to gain deeper insight into the reaction mechanism.

This study utilizes ab initio simulations to investigate the atomistic scale dissolution mechanism of pyrophyllite in pure water at neutral pH, where the pyrophyllite is considered as a proxy for 2:1 clay minerals. The dissolution has been studied starting from the two most stable edge faces (110) and (010) with different water pressure configurations. The Metadynamics approach was used to sample the free energy surface of the system with three different coordination numbers of the detaching species as collective variables that span the reaction space.

The results show a clear preference for octahedral Al over tetrahedral Si detachment in either configuration. The dissolution reaction itself is a multistep process with several reaction intermediates in which the connectivity of the detaching complex to the edge surface changes step-by-step. The overall mechanism in all setups can be considered as a sequence of concurrent, reversible elementary reactions:

- 1) H₂O molecules or OH groups perform a nucleophilic attack on the dissolving surface site.
- 2) One or more ligand exchange reactions in the first coordination shell of the reacting sites lead to changes of its conformation and denticity at the mineral edge surface.
- 3) Collective proton transfer reactions between acidic and basic oxygen sites mediated via a chain of the hydrogen bonded molecules in the first and second coordination shell of the reacting site binds otherwise dangling bonds of the exchanged ligand.

Some specific phenomena connected to the pressure settings of the bulk water molecules are otherwise rarely observed octahedral coordinated Si and tetrahedral coordinated Al sites as intermediate complexes during the respective detachment reaction.

Table of Content

Abstract	iii
Table of Content.....	iv
1. Introduction.....	2
1.1 Structure of clay minerals.....	3
1.2 Motivation	5
1.3 Outline of the thesis	7
1.4 References	9
2. Theory.....	12
2.1 Kohn-Sham equation	12
2.2 Pseudopotential approximation.....	15
2.3 Basis Set and periodic boundary conditions.....	17
2.4 Ab initio molecular dynamics	18
2.5 Metadynamic simulations (MetaD).....	19
2.6 References	23
3. Dissolution mechanism of Pyrophyllite starting at the (110) edge.....	26
3.1 Introduction	26
3.2 Methods.....	29
3.2.1 System setup.....	29
3.2.2 Ab initio MD	30
3.2.3 Uncertainties.....	32
3.3 Results.....	32
3.3.1 Atomic scale dissolution mechanism.....	32
3.3.2 Activation energies	43
3.4 Discussion	44
3.4.1 Activation energies	48
3.5 Conclusion.....	49
3.6 Supporting Information	50
3.7 References	56
4. Dissolution mechanism of Pyrophyllite under metamorphic pressure conditions	64
4.1 Introduction	64
4.2 Methods.....	66
4.2.1 System setup.....	66

4.2.2 Ab initio MD	67
4.3 Results.....	68
4.3.1 The mechanism of Al edge surface leaching from the octahedral sheet	69
4.3.2 The mechanism of Si edge surface leaching from the tetrahedral sheet.....	71
4.3.3 Activation energies	75
4.4 Discussion	76
4.5 Conclusion.....	79
4.6 Supporting Information	81
4.7 References	86
5. High pressure dissolution mechanism of Pyrophyllite from the (110) edge	94
5.1 Introduction	94
5.2 System and simulation setup.....	94
5.3 Results.....	95
5.4 Conclusion.....	99
5.5 References	99
6. Conclusion and Outlook	100
6.1 References	104
Acknowledgements	106
Declaration of consent	107

1. Introduction

Clay minerals can be found in sedimentary rocks and soils. Their field of application is broad, bringing together a variety of disciplines like agriculture, history, life sciences and art (as ceramics) (Bergaya and Lagaly 2006).

Clay minerals often form by chemical or physical weathering, diagenesis or hydrothermal alteration processes of rocks (Churchman et al. 2006, Galán 2006). They determine the geochemistry of soils in the earth's crust due to their redox, hydraulic and other properties (Amram and Ganor 2005, Pusch 2006). Their capability for cation exchange in the interlayer and the adsorption of ions, for example, have a strong impact on pore water chemistry and determine their pH buffering effect. The protonation and deprotonation ability of the edge surface sites, which depends strongly on the elemental composition of the phyllosilicate, is the reason of their strong redox potential (Pusch 2006, Stucki 2006). Thus, the reactivity of clay minerals and understanding the kinetic and thermodynamic behaviour is of key importance, not only to predict soil properties but also to assess the effectiveness of their applications as well. Two of the main reactions altering the surfaces and therefore its reactivity are crystal growth and dissolution, both of which either add or dissolve groups from the minerals surface. Whereas the dissolution of a mineral is especially interesting in terms of estimating the time scales for the release of incorporated elements with potential negative effects on environment and living beings.

In general, the dissolution of a mineral is triggered by the step-by-step hydration of terminal groups at the surfaces of the bulk mineral, and subsequent breaking of the bonds connecting them to the bulk (Furrer and Stumm 1986, Nagy 1995). The valency of those terminal sites determines how many bonds need to be hydrated before the detachment from the surface occurs. The dissolution reaction then proceeds with the dissolution of the terminal group, surrounded by a hydration shell, into the surrounding solution. The exact order of the reaction steps depends on the minerals' composition and the topology of the surrounding surface, i.e. if it is a step, kink, edge or terrace site. If the topologies have fewer bonds to the bulk surface – like for kink or step sites for example – the hydrolysis of the surface bonds should have smaller activation barriers than those sites with a higher number of surface connections.

In order to obtain insight into the mechanisms of the clay minerals reactivity two possibilities are available: Experimental methods and computational simulations. The first option includes methods like batch dissolution experiments (Amram and Ganor 2005, Bauer and Berger 1998, Cama et al. 2000, Cappelli et al. 2018, Komadel et al. 1996), Atomic Force Microscopy (Aldushin 2006, Bickmore 2001, Bosbach 2000, Brandt 2003, Kuwahara 2006, Rufe 1999) and others that shed a light on the macroscopic kinetic and thermodynamic features of the materials and their reactions. While the experimental insight is of utmost importance, it fails to show the detailed mechanism at the atomistic scale, especially if the time scale of a single reaction step is much smaller (pico- or nanoseconds) than what is empirically observable.

Computational simulations help to investigate reaction events at the molecular level, but to get accurate results it is important to include a good representation of bond breaking and bond formation events that occur during each reaction. Crystal growth as well as dissolution is believed to react in a step-by-step addition/removal of polyhedral units. As these polyhedra have a central ion with multiple bonds to the oxygen corners all these bonds need to be formed or broken for each addition/removal step. For the dissolution process this would mean

each detachment step of a polyhedral coordinated ionic species undergoes a step-by-step rearrangement of the bonds connecting the ion to the bulk. Consequently, the accuracy of the mechanism depends on the precise calculation of the individual bond strengths. This can be achieved with *ab initio* molecular dynamic (AIMD) simulations, that are able to calculate nearly exact energies of the particles in the system of interest. Moreover, a realistic surface and explicit solvent should be considered to get a more accurate solution for dissolution, growth and sorption reactions. This increases the particle number in the system considerably, due to the number of water molecules in bulk water and the atoms needed to represent the clay minerals bulk and edge structure. A compromise between accuracy and efficiency in calculation time are density functional theory (DFT) based calculations. While Force-field (FF) based calculations are less time consuming their accuracy depend on empiric parameters and are thus only applicable to a limited number of systems similar to the one used for the FF calibration. All electron calculations, on the other hand, would provide highest possible accuracy but very high computational time consumption as well and were therefore not considered.

In this work, the dissolution reactions of clay minerals were investigated. Chemical reactions like the dissolution are activated events with an activation barrier, that needs to be crossed by the system to continue reacting. These barriers are often higher than the typical temperature fluctuations that can be mapped in a classical AIMD simulation, hence a more enhanced sampling method for the free energy surface (FES) is necessary. That is the reason why the Metadynamics (Churakov et al. 2004, Laio and Parinello 2002, Laio et al. 2005, Laio and Gervasio 2008) approach is applied. This approach is able to fill the free energy well in order to overcome the smallest nearby activation barriers and maps the complete FES over time by moving the system from one minimum to another. Of key importance for the accuracy of the approach are the selected reaction coordinates or so-called collective variables, which should be selected carefully in order to minimize the influence of the bias potential on the reaction mechanism.

1.1 Structure of clay minerals

The term "clay mineral" refers to phyllosilicates and to minerals which impart plasticity to clay and which harden upon drying or firing. This definition was formalised by a joint meeting of the AIPEA and CMS nomenclature committees in 1995 (Guggenheim and Martin, 1995). Thus, the most common clay minerals can be characterized as phyllosilicates with different compositions. Clay minerals consist of tetrahedral (T) and octahedral (O) sheets. The tetrahedral sheet typically contains silicon tetrahedra connected via three of the four coordinating oxygens (basal oxygen (O_b) in Fig. 1.1) forming a hexagonal arrangement. The octahedral sheet is directly connected to the tetrahedral sheet via the fourth oxygen of the silicon tetrahedra (O_a). The centre of the octahedra are commonly aluminium ions and all six coordinating oxygens are shared between either three or two octahedra in case of a trioctahedral or dioctahedral sheet (see Fig. 1.1), respectively. Two oxygens (O_a in Fig. 1.1) connect the octahedral with the tetrahedral sheet. In case of a dioctahedral sheet, vacant cavities are present, and the dangling bonds of the oxygens created through these cavities are saturated by protons. Depending on the number of sheets that are stacked together, the so-called 1:1 and 2:1 layers with TO and TOT stacking can be formed, respectively. Whereas the basal plane of one tetrahedral sheet in the TOT structure (2:1) is facing the opposite direction

compared to the other (O is sandwiched between two T) (Fig. 1.2). In this study, only the 2:1 phyllosilicates are considered.

The interlayer refers to the space between the TOT layers. Depending on the structural charge in the TOT layer, the interlayer is occupied by charge compensating ions (mostly cations). The more substitutions in the clay mineral sheets the higher charge compensation is needed in the interlayer i.e. more cations or higher charged cations. Thus, the layers are held together by either the van der Waals forces between basal oxygen atoms in the charge neutral TOT layer or by the combination of van der Waals and coulombic attraction of the charged layer with the interlayer cations. The most common interlayer cations are alkali and earth alkali elements. The interlayer cations have strong affinity to hydration and thus promote the uptake of water molecules into the interlayer.

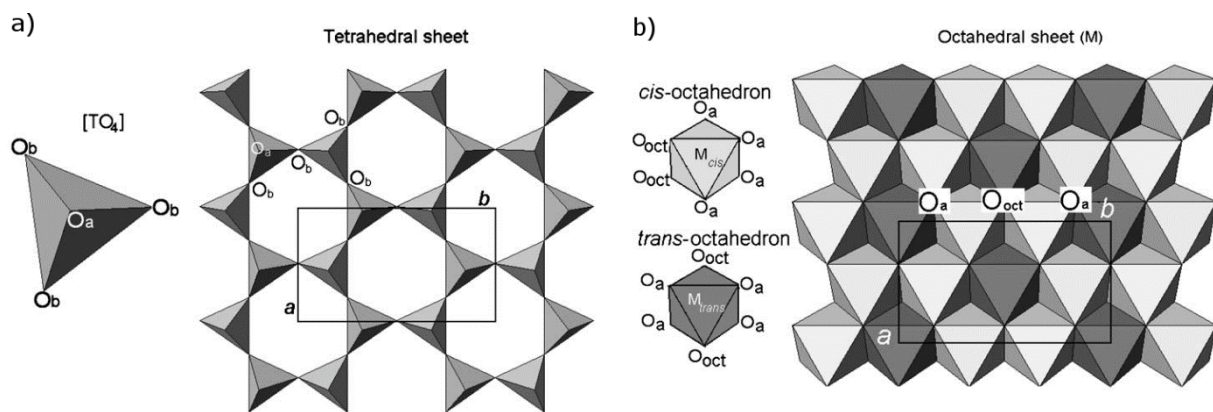


Figure 1.1: Structural units of the sheets that form the various types of clay minerals. a) The tetrahedral sheet consists of tetrahedrally coordinated M_x (mainly Si^{4+}) that are connected to neighbouring tetrahedra via three of the oxygen (O_b). The fourth oxygen (O_a) functions as connector to the octahedral sheet. b) The octahedral sheet consists of six-fold coordinated M_y (mainly Al^{3+}) that are connected via the oxygen. There are two types of oxygen, one is a possible bridge to the silicon sheets (O_a) and the other are only shared with octahedra (O_{oct}). a and b show the unit-cell parameters. Image modified and taken from Handbook of Clay Science (Brigatti et al. 2006).

Pyrophyllite (dioctahedral) and talc (trioctahedral) are ideal charge-neutral 2:1 clay minerals without any substitutions neither in the tetrahedral nor in the octahedral sheets. The structure of other clay minerals can be derived from these ideal structures. Isomorphic substitutions either in the tetrahedral sheet (by Al, Fe(III) or other trivalent cations) or in the octahedral sheet (by Mg, Fe(II) and other divalent cations) lead to a structural layer charge. The charge compensating cations in the interlayer are highly hydrophilic and favour hydration in the interlayer space. The uptake of water in the interlayer is responsible for the swelling property of clay minerals. On top of that, the stacking of the layers varies and results in different polytypes with different possible stacking sequences. Mixed layer structures are built up by at least two different phyllosilicate layers.

The clay mineral particles have different crystallographic facets and form terminal edge surfaces with preferred orientations depending on the surface stability. These are part of the overall surface area of clay particles (Schoonheydt and Johnston 2006), but in contrast to the chemical inert basal (001) planes the edge sites are reactive and pH sensitive: for this reason, mineral growth and dissolution mainly takes place at the clay mineral edges.

The stability, speciation and the charge of the edge surfaces is pH-dependent. The protonation state of the edge sites determines their reactivity as well as their stability and in consequence have an impact on the sorption capability and activation barriers for mineral growth or dissolution. Because of the low crystallographic symmetry of clay minerals, the structure of different edge surfaces and the reactivity of the corresponding edge sites shows a high variability.

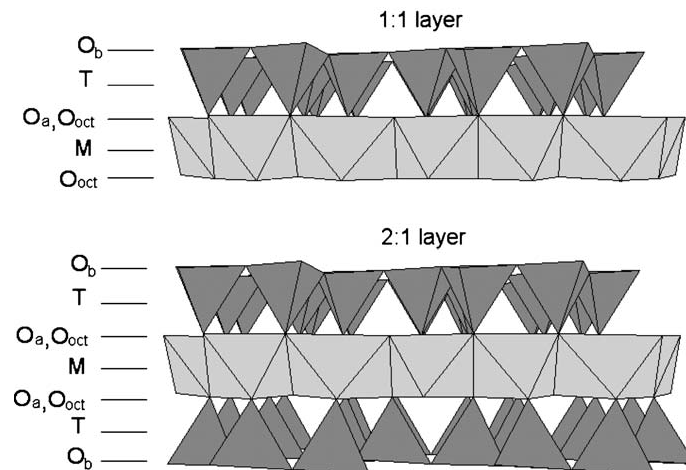


Figure 1.2: The two types of layers in clay minerals. Image modified and taken from Handbook of Clay Science (Brigatti et al. 2006).

The most common edges of 2:1 clay particles of pyrophyllite, montmorillonite and other smectites are the (110) and (010) edges, as found by AFM studies (Kraevsky et al. 2020) and calculations (Bickmore et al. 2003, Liu et al. 2012a, Liu et al. 2012b, White and Zelazny 1988). The surface structure of both edge surfaces differs distinctly. While the (010) edge is covered with terminal monodentate OH_x groups only, the (110) edge also includes bridging oxygen sites that connects Si-tetrahedral with Al-octahedral sites as well as bidentate OH groups shared by neighbouring Al octahedra.

1.2 Motivation

A good proxy for the clay minerals is pyrophyllite with an ideal 2:1 phyllosilicate structure without defects or substitutions and thus without structural charge or interlayer water molecules. This is an efficient compromise between the system size, including the high number of solvent molecules plus the atoms of the layered clay structure, and a reasonable simulation time, which would increase with higher number of elements and localized charges.

The ab initio simulations are expected to give detailed insight into the clay mineral dissolution mechanism at an atomistic scale. The experimental studies of clay mineral dissolution (Amram and Ganor 2005, Bauer and Berger 1998, Bickmore et al. 2001, Bosbach et al. 2000, Brandt et al. 2003, Cama et al. 2000, Cappelli et al. 2018, Komadel et al. 1996, Kuwahara 2006, 2008) suggest initial non-stoichiometric dissolution. The octahedral sheet is preferentially dissolved, as demonstrated by the leaching of the ions that occupied the octahedral sites. When reaching steady-state conditions the dissolution proceeds in a congruent fashion and both clay mineral sheets dissolve stoichiometrically in 1:2 ratio for octahedral to tetrahedral sites according to their ratio in the sum formula. The simulations can now be used to understand the mechanism

of bond breaking and together with its activation barriers determine which species is more likely to dissolve.

The metadynamic simulations applied in this thesis are plotting the free energy surfaces of the dissolution reactions and maps the hills and wells nearby the initial state of the system. As soon as the free energy surface is known, a minimum energy path can be found that connects the educt state with the product state. On this path every hill corresponds to a transition state and each well resembles an intermediate state. The difference between minima to adjacent maxima on the minimum energy path corresponds to the activation free energy that needs to be overcome to advance with the reaction. Once the height of each barrier is known they can be compared to other relevant reactions like sorption of ions, ion incorporation or mineral growth. With a catalogue of each barrier a probability for each reaction event can be calculated and predictions of the macroscopic behaviour can be made. Furthermore, simulations reveal the molecular mechanism of the clay mineral dissolution. This information can be used for specific surface moderation aimed to enhance or passivate a certain favourable reaction behaviour. The prediction of retention times of pollutants in soils and clay formations, the mechanism and activation barriers, that determine the kinetics of the dissolution reaction are of particular importance.

1.3 Outline of the thesis

This PhD thesis is organised as a collection of manuscripts, which are fully or in part published. Chapter 3 to 5 present the results of the PhD project and chapter 6 will provide the conclusion of this work and open question that are worth further investigating.

Chapter 1:

Introduction

Schliemann, R.

The first chapter above gave the introduction to the topic of the thesis and defines the structure of the clay minerals as well as the objectives and motivation of this study.

Chapter 2:

Theory

Churakov, S. V.; Schliemann, R.

The second chapter describes the theoretical background of the ab initio simulations. The material presented there is part of the publication “Churakov, S.; Schliemann, R.; (2021) Ab initio simulations of clay minerals reactivity and thermodynamics, in C.I. C.I. Sainz-Díaz (Editor). Computational Modeling in Clay Mineralogy, AIPEA Educational Series, Pub. No. 3, Chapter 6, Digilabs, Bari, Italy.” The theoretical part has been jointly written by both authors.

Chapter 3:

Theoretical study:

Dissolution mechanism of pyrophyllite starting at the (110) edge

Schliemann, R.; Churakov, S. V.

Chapter 3 summarises the ab initio study on pyrophyllite dissolution published as René Schliemann & Sergey V. Churakov (2021) “Atomic scale mechanism of clay minerals dissolution revealed by ab initio simulations” *Geochimica et Cosmochimica Acta*, 293, 438-460. The study gives new insight into the molecular mechanism of pyrophyllite dissolution as obtained by Metadynamic simulations. The educt state was represented by a monolayer pyrophyllite with the size of 2x2 unit cells and a slab of 60 water molecules in periodic boundary conditions. The FES was scanned with the help of three coordination numbers of one edge site used as collective variables for the FES mapping.

The first author performed and prepared all the Metadynamics simulations. The main part of the first manuscript version was completely written by R. Schliemann and the second author contributed paragraphs in the introduction, methods and discussion chapters.

Chapter 4:

Theoretical study:

Dissolution mechanism of Pyrophyllite under metamorphic pressure conditions

Schliemann, R.; Churakov, S. V.

The fourth chapter presents the results of the ab initio simulations regarding the pyrophyllite dissolution at elevated pressure and is published as René Schliemann & Sergey V. Churakov “Pyrophyllite dissolution at elevated pressure conditions: An ab initio study” *Geochimica et Cosmochimica Acta* 307, 42–55. Another study on the dissolution mechanism of pyrophyllite was performed, this time starting at the (010) edge surface and water pressure in the range of metamorphic conditions.

The first author performed and prepared all the Metadynamics simulations. The main part of the manuscript was written by the first author and the second author contributed paragraphs in the introduction and discussion parts.

Chapter 5:

Theoretical study:

High pressure dissolution of Al from Pyrophyllite at the (110) edge

Churakov, S. V.; Schliemann, R.

The fifth chapter presents the results of an investigation of the dissolution of pyrophyllite under extreme water pressure conditions at the (110) edge and has been published as part of the chapter: “Churakov, S.; Schliemann, R.; (2021) Ab initio simulations of clay minerals reactivity and thermodynamics, in C.I. Sainz-Díaz (Editor). *Computational Modeling in Clay Mineralogy*, AIPEA Educational Series, Pub. No. 3, Chapter 6, Digilabs, Bari, Italy.” The part included in this thesis was entirely written by the second author.

Chapter 6:

Conclusion and Outlook

Finally, chapter 6 summarises the main findings of the studies presented in this thesis, addressing the open questions and proposing strategies for further investigation.

1.4 References

- Aldushin K., Jordan G. and Schmahl W. W. (2006) Basal plane reactivity of phyllosilicates studied in situ by hydrothermal atomic force microscopy (HAFM). *Geochimica et Cosmochimica Acta* **70**, 4380–4391.
- Amram K. and Ganor J. (2005) The combined effect of pH and temperature on smectite dissolution rate under acidic conditions. *Geochimica et Cosmochimica Acta* **69**, 2535–2546.
- Bauer A. and Berger G. (1998) Kaolinite and smectite dissolution rate in high molar KOH solutions at 35 degrees and 80 degrees C. *Applied Geochemistry* **13**, 905–916.
- Bergaya F. and Lagaly G. (2006) Chapter 1 General Introduction: Clays, Clay Minerals, and Clay Science. In (eds. B. K. G. T. Faïza Bergaya and G. Lagaly). *Developments in Clay Science*. Elsevier. pp. 1–18.
- Bickmore B., Bosbach D., Hochella M., Charlet L. and Rufe E. (2001) In situ atomic force microscopy study of hectorite and nontronite dissolution: Implications for phyllosilicate edge surface structures and dissolution mechanisms. *American Mineralogist* **86**, 411–423.
- Bickmore B., Rosso K., Nagy K., Cygan R. and Tadanier C. (2003) Ab initio determination of edge surface structures for dioctahedral 2 : 1 phyllosilicates: Implications for acid-base reactivity. *Clays and Clay Minerals* **51**, 359–371.
- Bosbach D., Charlet L., Bickmore B. and Hochella M. (2000) The dissolution of hectorite: In-situ, real-time observations using atomic force microscopy. *American Mineralogist* **85**, 1209–1216.
- Brandt F., Bosbach D., Krawczyk-Barsch E., Arnold T. and Bernhard G. (2003) Chlorite dissolution in the acid pH-range: A combined microscopic and macroscopic approach. *Geochimica et Cosmochimica Acta* **67**, 1451–1461.
- Brigatti M. F., Galan E. and Theng B. K. G. (2006) Chapter 2 Structures and Mineralogy of Clay Minerals. In (eds. B. K. G. T. Faïza Bergaya and G. Lagaly). *Developments in Clay Science*. Elsevier. pp. 19–86.
- Cama J., Ganor J., Ayora C. and Lasaga C. (2000) Smectite dissolution kinetics at 80 degrees C and pH 8.8. *Geochimica et Cosmochimica Acta* **64**, 2701–2717.
- Cappelli C., Yokoyama S., Cama J. and Huertas F. J. (2018) Montmorillonite dissolution kinetics: Experimental and reactive transport modeling interpretation. *Geochimica et Cosmochimica Acta* **227**, 96–122.
- Churakov S., Iannuzzi M. and Parrinello M. (2004) Ab initio study of dehydroxylation-carbonation reaction on brucite surface. *Journal of physical Chemistry B* **108**, 11567–11574.
- Churchman G. J., Gates W. P., Theng B. K. G. and Yuan G. (2006) Chapter 11.1 Clays and Clay Minerals for Pollution Control. In (eds. B. K. G. T. Faïza Bergaya and G. Lagaly). *Developments in Clay Science*. Elsevier. pp. 625–675.
- Furrer G. and Stumm W. (1986) The coordination chemistry of weathering .1. Dissolution kinetics of Delta-Al₂O₃ and BeO. *Geochimica et Cosmochimica Acta* **50**, 1847–1860.
- Galán E. (2006) Chapter 14 Genesis of Clay Minerals. In (eds. F. Bergaya, B. K. G. Theng, and G. Lagaly). *Developments in Clay Science*. Elsevier. pp. 1129–1162.

- Guggenheim S. and Martin R. T. (1995) Definition of clay and clay mineral - Joint report of the AIPEA nomenclature and CMS nomenclature committees. *Clays and Clay Minerals* **43**, 255–256.
- Komadel P., Bujdak J., Madejova J., Sucha V. and Elsass F. (1996) Effect of non-swelling layers on the dissolution of reduced-charge montmorillonite in hydrochloric acid. *Clay Minerals* **31**, 333–345.
- Kuwahara Y. (2006) In-situ AFM study of smectite dissolution under alkaline conditions at room temperature. *American Mineralogist* **91**, 1142–1149.
- Kuwahara Y. (2008) In situ observations of muscovite dissolution under alkaline conditions at 25-50 degrees C by AFM with an air/fluid heater system. *American Mineralogist* **93**, 1028–1033.
- Laio A. and Gervasio F. L. (2008) Metadynamics: a method to simulate rare events and reconstruct the free energy in biophysics, chemistry and material science. *Reports on Progress in Physics* **71**.
- Laio A. and Parrinello M. (2002) Escaping free-energy minima. *Proceedings of the national Academy of Sciences of THE UNITED STATES OF AMERICA* **99**, 12562–12566.
- Laio A., Rodriguez-Forteza A., Gervasio F., Ceccarelli M. and Parrinello M. (2005) Assessing the accuracy of metadynamics. *Journal of physical Chemistry B* **109**, 6714–6721.
- Liu X., Lu X., Meijer E. J., Wang R. and Zhou H. (2012) Atomic-scale structures of interfaces between phyllosilicate edges and water. *Geochimica et Cosmochimica Acta* **81**, 56–68.
- Liu X., Lu X., Wang R., Meijer E. J., Zhou H. and He H. (2012) Atomic scale structures of interfaces between kaolinite edges and water. *Geochimica et Cosmochimica Acta* **92**, 233–242.
- Nagy K. (1995) Dissolution and precipitation kinetics of sheet silicates. In *Chemical Weathering rates of Silicate Minerals* (eds. A. White and S. Brantley). Reviews in Mineralogy. pp. 173–233.
- Pusch R. (2006) Chapter 6 Mechanical Properties of Clays and Clay Minerals. In (eds. B. K. G. T. Faïza Bergaya and G. Lagaly). *Developments in Clay Science*. Elsevier. pp. 247–260.
- Rufe E. and Hochella M. (1999) Quantitative assessment of reactive surface area of phlogopite during acid dissolution. *Science* **285**, 874–876.
- Schoonheydt R. A. and Johnston C. T. (2006) Chapter 3 Surface and Interface Chemistry of Clay Minerals. In (eds. B. K. G. T. Faïza Bergaya and G. Lagaly). *Developments in Clay Science*. Elsevier. pp. 87–113.
- Stucki J. W. (2006) Chapter 8 Properties and Behaviour of Iron in Clay Minerals. In (eds. B. K. G. T. Faïza Bergaya and G. Lagaly). *Developments in Clay Science*. Elsevier. pp. 423–475.
- White G. N. and Zelazny L. W. (1988) Analysis and implications of the edge structure of dioctahedral phyllosilicates. *Clays and Clay Minerals* **36**, 141–146.

2. Theory

Quantum mechanical simulations of minerals, interfaces and aqueous systems are performed by using different approximations to the exact solution of the Schrödinger equation:

$$H\Psi = E\Psi \quad (2.1)$$

with the Hamiltonian H , the wavefunction Ψ and the energy E . There are several ways to get an approximate solution of eq. 2.1. The following part is focused on the practical aspects of the Density Functional Theory (DFT). DFT and Hartree-Fock based methods are often confronted to a comparative analysis with respect to accuracy and the level of empiricism. Either approach has advantages and limitations. Modelling on mineral interfaces usually requires the consideration of a large number of atoms and molecules in order to realistically represent the bulk solution and mineral structure as well as the interface. For the reasons of computational efficiency and the complexity of the system setup, the use of the DFT approach combined with periodic boundary conditions is the method of choice in such modelling.

2.1 Kohn-Sham equation

DFT maps the multi-electron Schrödinger equation on to an one-electron equation with an effective electrostatic field. This mapping is exact in theory, but in practice requires several approximations e.g. the Kohn-Sham equation (Hohenberg and Kohn 1964, Kohn and Sham 1965). The Kohn-Sham Hamiltonian \hat{H}^{KS} includes kinetic energy of electrons T_{kin} , nuclei-nuclei \hat{V}_{nn} , nuclei-electrons \hat{V}_{ne} , electron-electron \hat{V}_{ee} term which are simple classical columbic interactions and the exchange-correlation energy \hat{E}_{XC} :

$$\hat{H}^{KS} = T_{kin} + \hat{V}_{nn} + \hat{V}_{ne} + \hat{V}_{ee} + \hat{E}_{XC} \quad (2.2)$$

The modern DFT approach uses electron orbitals to calculate the kinetic energy contributions and apply different semi-empirical approximations for the exchange and the correlation energy. To deal with known limitations of the DFT the original Kohn-Sham equations can be augmented with a number of semi empirical corrections, which are known to be essential for the accurate predictions of material properties. In general, an extended Hamiltonian \hat{H}^{ext} can be written as a contribution of Kohn-Sham terms.

The major theoretical developments in the field of DFT are focused on formulating an accurate description of the exchange-correlation functional \hat{E}_{XC} , which should in principle cover all relevant quantum mechanical effects without need for additional corrections.

The exchange-correlation energy term \hat{E}_{XC} is a lump contribution, which accounts for both the static and dynamic electron–electron correlations, and the Pauli exchange interaction. The first widely successful formulation of the exchange correlation functional \hat{E}_{XC} used was based on the so-called local spin density approximation (LSDA). In this approximation, the theoretically calculated $\hat{E}_{XC}(\rho)$ of a homogeneous electron gas with the density ρ is used to evaluate the properties of heterogeneous multi electronic system with space dependent electron density $\rho(r)$. A formally exact description of the exchange correlation energy can be obtained using concept of the exchange correlation hole $\bar{h}_{XC}(|\vec{r} - \vec{s}|, \rho(\vec{s}))$ located at an electron in the position \vec{s} (non locality):

$$\varepsilon_{XC}(\rho(\vec{r})) = \frac{1}{2} \int d\vec{s} \frac{\bar{h}_{XC}(|\vec{r} - \vec{s}|, \rho(\vec{s}))}{|\vec{s} - \vec{r}|} \quad (2.3)$$

On average, the electron within a molecule or a solid has a non-zero electron density. In each moment of time, every electron maintains a private space preventing other electrons to be in its proximity due to the electrostatic repulsion and Pauli exclusion. This local decrease of density around each electron creates an additional stabilization energy expressed in the \hat{E}_{XC} . The exchange correlation hole is however non-local and not necessary fully localized at the electron.

In the local density approximation truly nonlocal $\bar{h}_{XC}(\vec{r}, \vec{s})$ is replaced with local exchange correlation hole of a homogeneous electron gas $\bar{h}_{XC}^{hom}(|\vec{r} - \vec{s}|, \rho(\vec{r}))$ at position \vec{r} (locality):

$$\varepsilon_{XC}^{LDA}(\rho(\vec{r})) = \frac{1}{2} \int d\vec{s} \frac{\bar{h}_{XC}^{hom}(|\vec{r} - \vec{s}|, \rho(\vec{r}))}{|\vec{s} - \vec{r}|} \rightarrow \text{closed form function of } \rho \quad (2.4)$$

$$E_{XC}^{LDA} = \frac{1}{2} \int d\vec{s} \rho(\vec{r}) \varepsilon_{XC}^{LDA}(\rho(\vec{r})) \quad (2.5)$$

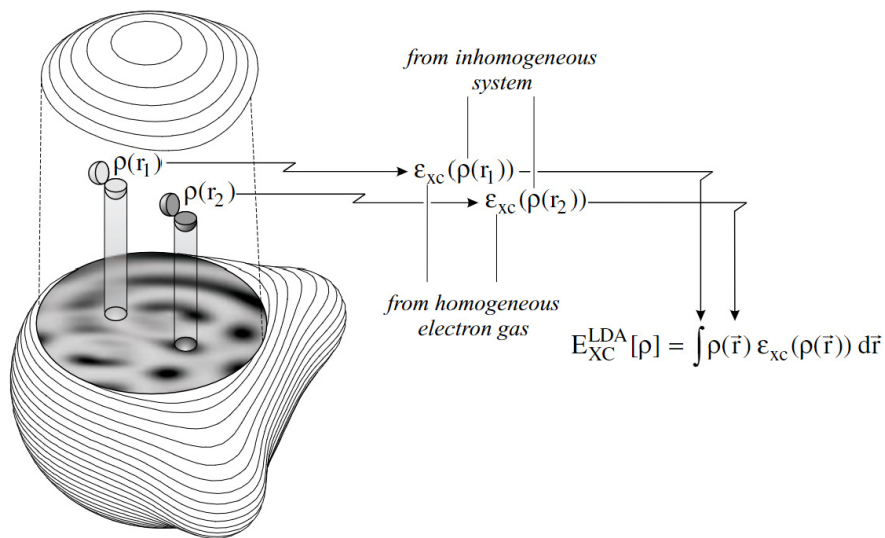


Figure 2.1: Illustration of the local density approximation for \hat{E}_{XC} of an inhomogeneous system such as a H_2O molecule, taken from (Koch and Holthausen 2015). $\varepsilon_{XC}(\rho(\vec{r}))$ represents the exchange correlation energy per particle of a homogeneous electronic gas with the density ρ .

This approximation has been particularly successful for the systems with weakly varying electron density and even for the complex inhomogeneous systems such as molecules and solids. Such an unexpected success of the LSDA is explained by the fact that its formulation satisfies a number of fundamental relationships imposed on the general properties of the electron exchange-correlation.

The LSDA can in principle be systematically improved by taking into account local gradients of electron density, and kinetic energy density (Perdew et al. 1996). These functionals are referred to as Generalized Gradient Approximations (GGA) and meta-GGA approximations, respectively. The next level of complexity and accuracy requires the consideration of partial contributions from non-local Hartree-Fock exchange and multi-electron correlation in Random Phase Approximation (RPA) taking into account non-occupied orbitals. The last two functionals are referred to as hybrid and double-hybrid functionals, respectively. If \hat{E}_{XC}

depends only on the local electron density and its derivatives at the same point the functional is called semi-local. These functionals provide accurate description of the system with the localized (single minima centrosymmetric) exchange correlation hole.

The nonlocal \hat{E}_{XC} - functionals, depend on the local density and the proximity typically expressed in an integral form. The exact, albeit unknown explicitly, exchange-correlation energy is truly nonlocal by its physical nature. The non-local exchange and correlation potentials should be more accurate but are more computationally expensive.

The Pauli exchange interaction can in fact be calculated exactly within the Hartree-Fock theory. This allows for the formulation of so-called hybrid potentials, which uses a linear combination of non-local exchange interaction obtained in HF-approximation and local, usually gradient corrected, exchange and correlation functional. The B3LYP and PBE are the two \hat{E}_{XC} potentials currently most commonly applied to geochemical systems:

$$\hat{E}_{PBE0}^{hybrid} = \hat{E}_{XC}^{PBE} + 0.25 \times (\hat{E}_X^{HF} - \hat{E}_X^{PBE}) \quad (2.6)$$

$$\hat{E}_{B3LYP}^{hybrid} = \hat{E}_{XC}^{LDA} + a_0 \times (\hat{E}_X^{HF} - \hat{E}_X^{LDA}) + a_x \times \Delta\hat{E}_X^{B88} + a_c \times \Delta\hat{E}_C^{PW91} \quad (2.7)$$

where \hat{E}_X^{HF} is the exact Hartree – Fock exchange, $a_0 = 0.20$, $a_x = 0.72$ and $a_c = 0.81$ are empirical coefficients fitted to the experimental data, $\Delta\hat{E}_X^{B88}$ and $\Delta\hat{E}_C^{PW91}$ are the gradient corrections to the LDA exchange and correlation after (Becke 1988, Perdew and Wang 1992), respectively.

A large number of functionals has been proposed for specific applications. Extensive benchmarks and tests are available in literature (Goerigk and Grimme 2011, Peverati and Truhlar 2014).

Despite the significant progress in the development of the advanced \hat{E}_{XC} approaching chemical accuracy on the top hierarchy of the functionals, most of the calculations are performed at GGA level of theory. The LDA typically underestimates lattice constants by 1% or 2% and predicts rather realistic surface geometry. In general, LSDA tends to overestimate binding energies in the molecules and solid. However, the calculation of the relative energies, which do not involve breaking bonds, such as cohesion energy are convincingly accurate. GGA is substantially improved over LDA. It has the tendency to slightly overestimate interatomic bond lengths in molecules and the lattice constants in solids. The cohesive energies and surface energies are well reproduced. In comparison with GGAs, some meta-GGAs have been shown to improve the accuracy of lattice constants and bond distances for solids alone with accurate surface and binding energies. Semi-local potentials are known to have low accuracy in description of the geometry and energies of the activated complexes in chemical reactions, which are associated with strong stretching of chemical bonds. In such atomic configuration, where bonds are about to break, the exchange correlation hole typically becomes delocalized and the semi-local approximation is not accurate. For similar reasons semi-local functionals may show a pure performance in description of compounds with *d*- and *f*- elements, where chemical bonds are formed by combination of the extended *s*- or *p*- electronic states with localized *d*- or *f*- electronic states.

Whereas diffuse (extended in space far from nucleus) *4s*- and *4p* valence states in the first *3d* elements block can naturally overlap to form covalent bonds, the compact *3d*- states located closer to the core need to be “stretched out” to form an efficient bond overlap. Such deformation of *3d* orbitals leads to de-localization of the exchange correlation hole and the

partial failure of the semi local functionals, which tend to overestimate the electron hole localization for such electronic configurations.

Dispersion interaction arises due to instantaneous correlation between induced dipoles in the electron density. This type of interaction is a truly non-local property of the system and cannot be accounted for by a semi-local density functional. Several approaches have been considered to include dispersion correction into DFT theory. The approximation embarks on the development of non-local density functional which could account for the Van der Waals type interaction (Peverati and Truhlar, 2012). This fundamental approach is however related to a substantial computational overhead. Another, more pragmatic approach has been developed by Grimme (Grimme et al., 2016) and employs a semi empirical correction for the parameters using the screened inverse power law expansion. The coefficients of these expansions are parametrized based on highly accurate correlated QM calculations. The approach of Grimme has been shown to be very successful in the simulations of various geochemical systems including aqueous solution.

The major advantage of using the semi-local exchange correlation functionals is their computational efficiency. In general, GGA and meta-GGA are only 2 to 3 time slower than LSDA. In contrast, non-local exchange correlation functionals require numerical integration of Eq. 2.3 and can be 10 to 100 times computationally more expensive compared to LSDA (Compare the subtle difference between the Eq. 2.3 and 2.4, which is manifested in the non-local $\rho(\vec{s})$ v.s. local $\rho(\vec{r})$ dependence of the exchange correlation hole on the density). In practice, such functionals are only applied to small molecular systems or for benchmarking.

2.2 Pseudopotential approximation

Each electron in the atom is filling a specific electronic state described by a wave function and the corresponding state energy. In ground state, the lowest energy levels are filled first. On the basis of orbital energy, the electronic states in an atom can be subdivided into core and valence states. The energy of core electrons is much lower compared to the energy of the possible interatomic bond energy. For these reasons, the wave functions of the core electrons remain unchanged upon formation of chemical bonds between atoms in molecules and solids. In contrast, the energy of the valence electrons is comparable with the energy of chemical bonds or interatomic interactions. The spatial distribution and the energy of these electronic states is changing upon formation of chemical bonds. Since core electrons are insensitive to the chemical bonding these electronic states can be excluded from the explicit computations for the sake of computational efficiency using the pseudo-potential (PP) approximations.

Fig. 2.2 shows the atomic wave functions of a Si atom and the wave functions overlap of two Si atoms located at the bonding distance. The core state $1s$, $2s$ and $2p$ are spatially localized close to the centres of the corresponding Si atoms. The energy of these states is much larger than the Si-Si bonding energy (~ 4 eV). When two Si atoms come to the bonding distance the core electronic state densities do not overlap and thus do not contribute to the chemical bonding. In contrast $3s$ - and $3p$ - states are extended far beyond the core region and overlap with the electron wave functions of neighbouring atoms leading to covalent bonding.

Full electron wave functions have oscillatory behaviour inside the core region, which follows from requirements of the orthogonality to the lower energetic electronic states. This oscillatory behaviour can be smeared out to improve computational efficiency by the construction of a smooth, node-free pseudo wave function.

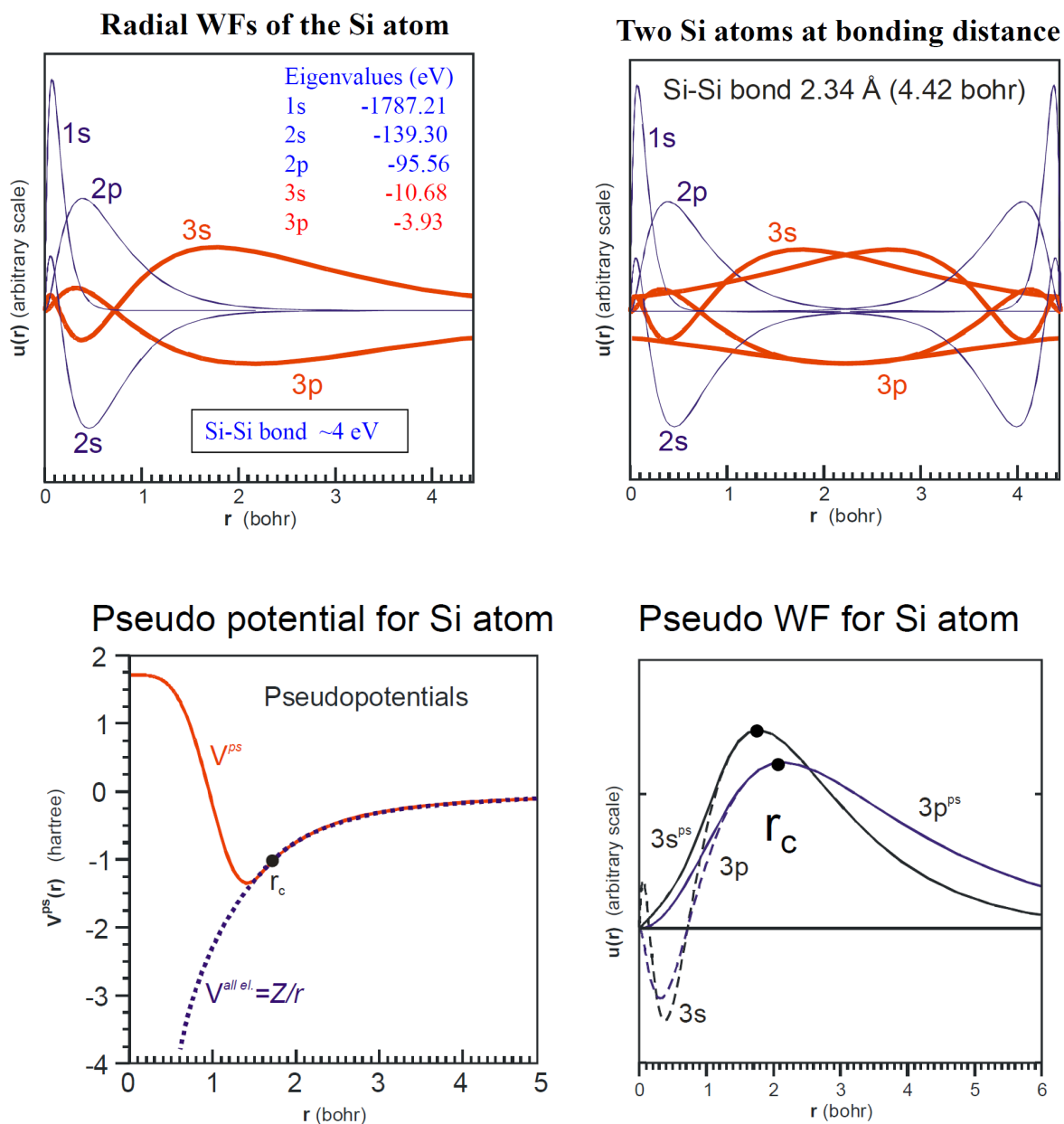


Figure 2.2: Full electron wave functions of an isolated Si atom (top left) and wave function overlap in Si₂ dimer (top right). Bare coulomb potential from Si atom and an effective pseudopotential (bottom left). Corresponding pseudo wave functions for 2s and 2p orbitals (bottom right).

The pseudopotential and pseudo wave functions are constructed to reproduce properties of valence electrons for an isolated atom in the ground and, if necessary, in the excited states based on the data from full electron calculations and at the same time to satisfy several boundary conditions (See Dolg and Cao 2012 for a review). The pseudo-wave functions are forced to reproduce true wave functions beyond a specific cut-off distance and to maintain a smooth node-less shape within this core radius (Fig. 2.2 bottom right, r_c). The node-less pseudo WF can be accurately reproduced using a small number of basis set functions. The smaller the core radius, the more accurate the pseudopotential. However, the smaller core radius typically requires a larger number of basis set functions. The pseudo-wave functions (squared) of a norm-conserving pseudopotential integrate to the same electron density as

true wave functions (Troullier and Martins 1991). The norm conservation condition is not imposed in the ultra-soft pseudopotential for the sake of the extra smooth behaviour of the pseudopotential in the core region. The lack of norm conservation conditions brings about additional computational overhead (Vanderbilt 1990). The choice between the norm-conserving and ultra-soft potential is often a compromise between the availability of the implementation in one or another computational code or the computational trade-off between the basis set size of computational overhead for the use of the ultra-soft PP.

2.3 Basis Set and periodic boundary conditions

The number of atoms (and electrons) which can be explicitly considered in the simulations are limited by computational costs. To mimic the behaviour of the macroscopic materials, the periodic boundary conditions are applied in the simulation of solids, liquids and their interfaces. In this approach the entire 3D space is filled with translationally equivalent periodic replica of the explicit simulation cell (see Fig. 2.3). In such a setup, it is convenient to use a periodic basis set function for electron orbitals and density, which are consistent with the periodicity of the system. The plane wave basis set is a natural choice for the system subjected to periodic boundary conditions. Fig. 2.3. illustrates the performance of the plane wave approximation for a parabolic function in one dimension at $[0,1]$ interval using $\cos(n2\pi x/L)$, where $n=0,1,2,\dots$. In this specific case, a very accurate description is already obtained using the first 6 plane waves.

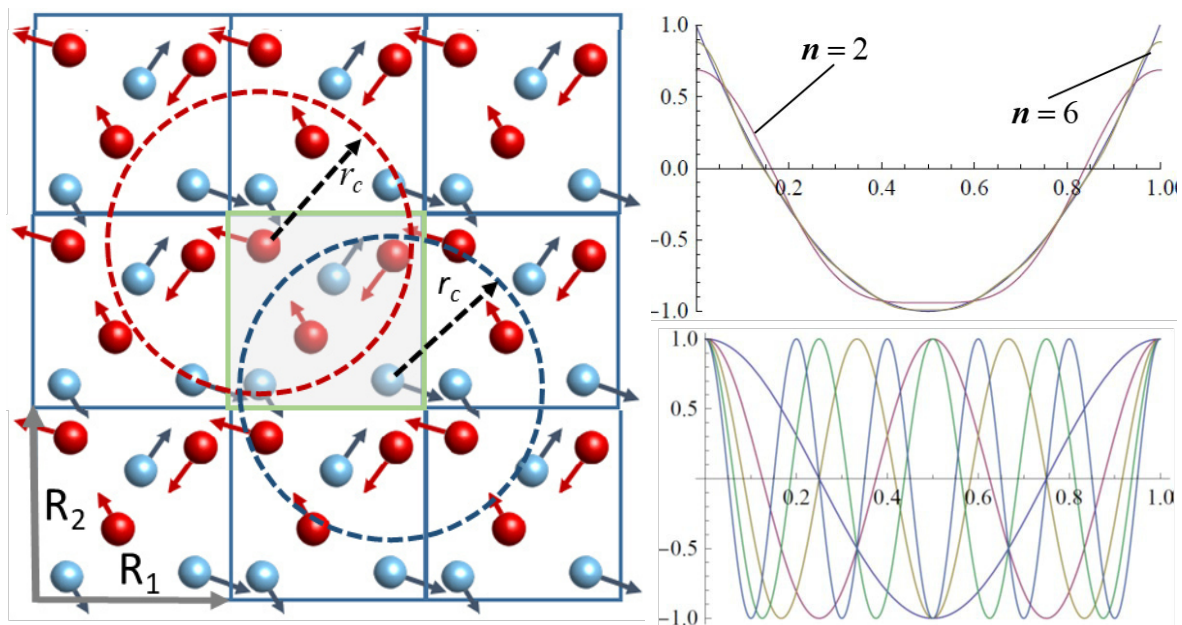


Figure 2.3: Left: Illustration of periodic boundary conditions in 2D. Simulation cell, shown as shaded box with green boxes contains three red and blue particle each, is replicated by lattice translational vectors R_1 and R_2 to fill the entire space. Arrows illustrate particle's instantaneous momentum. Dashed circles with radius r_c , shows coordination shell of particle with their periodic images. Right Top: An example showing the one-dimensional approximation of the parabolic function on an interval $L \in [0,1]$ with $\cos(n2\pi x/L)$ functions. Right Bottom: Individual basis set functions used to approximate the parabolic function.

A general form of the 3D plane wave basis set for a periodic wavefunction $\Psi(\vec{r})$ can be written as

$$\Psi_{\vec{k}}(\vec{r}) = \Psi(\vec{r} + n\vec{R}) = \sum_G c_{G+\vec{k}} e^{i(\vec{G}+\vec{k})\cdot\vec{r}} \quad (2.8)$$

where \vec{k} is the vector confined to the first Brillouin zone of the reciprocal cell, \vec{G} is the reciprocal lattice vector satisfying the condition $(\vec{G} \cdot \vec{R}) = 2\pi n$, with \vec{R} being the translational vectors of the real space periodic lattice and n is an integer. Since the $\vec{G} + \vec{k}$ vector is related to the energy of plain wave the number of the plane wave is restricted to satisfy the energy cut-off criteria

$$|\vec{G} + \vec{k}|^2 < E_{cutoff} \quad (2.9)$$

In polyatomic and molecular systems, the so-called basis set superposition error (BSSE) arises when atom localised wave functions are used. To understand the nature of BSSE error consider the calculation of binding energy for a Si₂ dimer, which can be calculated as energy difference between the total energy of Si₂ molecule and the energy of two isolated Si atoms. The Fig. 2.2. illustrates the atomic wave function of a Si atom and the wave function overlap at the bonding distance. In this example, the electron density of a single isolated atom of Si would be represented by the 3s and 3p basis functions. When two silica atoms form a dimer the electron total density distribution is represented by two 2s and two 3p basis functions. The effective number of basis set function is doubled compared to the calculations for an isolated atom. Better basis set quality for used in the composite system will result in artificial lowering of the dimer binding energy, referred to as BSSE. In contrast to the atom centred molecular orbitals, the particular property of the plane wave basis sets allow a smooth monotonic convergence of the basis set accuracy with an increasing number of plane waves. Plane wave basis functions do not depend on atomic positions (delocalized) and therefore provides an equally accurate representation of the election wave functions and density everywhere in the computational domain independent of the particular atomic configuration. For these reasons the plane wave basis set is free of the basis set superposition error (BSSE). This property is illustrated in Fig. 2.3 showing that every point in space is approximated by the same number of basis functions.

The plane wave basis set is almost exclusively used in conjunction with the pseudopotential approximation. Pseudo wave functions do not have oscillatory behaviour close to the core of the nuclei and allow achieving high accuracy of the interpolation with a small number of plane wave basis functions. The use of the fast Fourier transform technique allows having $n \cdot \log(n)$ scaling of the computational costs with the number of plane waves (n). The computational efficiency can be further improved by combining reciprocal space representations of the electron density based on plane waves with the real space Gaussian-like basis set for atomic orbitals. The latter approaches allow the short-range locality of electron distributions to be exploited (Kuehne et al. 2020).

2.4 Ab initio molecular dynamics

Time evolution of atoms and electrons can be described by a set of differential equations, which in principle need to be solved simultaneously. The electrons are lighter by more than a factor of 10³ than the nuclei and thus move much faster. Solving equations of motion for both nuclei and electrons simultaneously would need a very small integration step. Born-Oppenheimer (BO) and Car-Parrinello (CP) MD are two methods taking advantage of scale separation in the position of electrons and nuclei.

The BO molecular dynamics assumes that the electrons in the system are adiabatically decoupled from the motion of slow atoms and stay in the ground state as atom moves in the mean electrostatic potential. Thus, for every atomic configuration, the ground state distribution of electrons and total energy of the system is obtained solving the corresponding Schrödinger equation. Knowing the ground state of electrons, the forces acting on the nuclei can be calculated. These forces are used to obtain the molecular dynamics trajectory of Newton equation of motion for atomic cores. The accuracy of the BO molecular dynamics trajectories is particularly sensitive to the convergence of the wave functions to the ground state.

In Car-Parrinello-MD methods electrons are considered as classical particles with a fictitious mass which is 100-1000 times heavier than the actual rest mass of an electron. A system of coupled differential equations for electrons and nuclei taking into account the orthogonality of the electronic wave functions using Lagrange multipliers approach is solved simultaneously. The Car-Parrinello approach impose several conditions on the integration time step which need to be fulfilled to ensure adiabatic separation for the dynamics of electrons and nuclei. These conditions may depend on several specific parameters of the system, such as band gap and the basis set. In general, one can argue that CPMD is most appropriate for large band gap insulation materials. A more detailed analysis of the CPMD and a guideline for the appropriate choice of parameter can be found in extensive literature (Grossman, Schwegler et al. 2004, Schwegler, Grossman et al. 2004). The numerical schemas for the simulation of various thermodynamic ensembles is essentially the same as the one used in classical simulations and thus described in the previous chapter.

2.5 Metadynamic simulations (MetaD)

Reactants and products of chemical reactions, first order phase transitions and structural conformations are separated by large activation barriers, which are much higher than the energy amplitude characteristic to the thermal fluctuation in the system at the conditions close to reaction equilibrium. Accordingly, such transformations cannot be observed as spontaneous events in a conventional molecular dynamic trajectory even if the initial system is in metastable high energy state. The activation energy of the free energy barrier and transition mechanism of such a specific event can be studied using different methods of accelerated dynamics.

In either method, the evolution of the system needs to be described by a reaction coordinate. The reaction coordinate is a descriptive variable that is able to discriminate the difference between the initial and final state of the system, generally speaking referred to as the collective variable (CV). One of the main requirements for the collective variable used for the identification of reaction mechanisms of the system is the ability to quantitatively discriminate between the reaction products, reactants, and the reaction intermediates. A collective variable is thus a numerical indicator discriminating the actual state of the system. In principle any structural parameters can be used, such as interatomic distances, angles of coordination, or a more general cumulative function or state variable like electric field, energy, mean square displacement of an atomic group, the order parameter etc.. The nature of the method is such that only those free energy states of the system, which are discriminated by the collective variables, can be sampled. Various choices of collective variable are feasible.

The Metadynamics (MetaD) method allows to calculate the free energy of the system as function of reaction coordinates. At thermal equilibrium the system tends to stay in the low

energy state. In MetaD simulations, the system is systematically pushed away from the local or global energy minimum, which it is currently occupying, by means of a time dependent external potential composed of the sum of Gaussian like functions in the space of selected CVs. Such hill-like Gaussian penalty functions are added progressively to the external potential boosting the system to explore the configurational space. For a sufficiently long simulation run the collected external potential has been shown to represent the free energy surface of the system in the space spanned by the CVs (Laio and Parrinello, 2002). The trajectories obtained in MetaD simulations resemble the minimum energy path (MEP) between the reaction intermediates. Detailed analysis of the FES allows to reveal the multiple competitive reaction mechanisms. The method has been successfully applied to reactions on mineral surfaces and structural transformation in clay minerals (Molina-Montes et al., 2010; Molina-Montes et al., 2013).

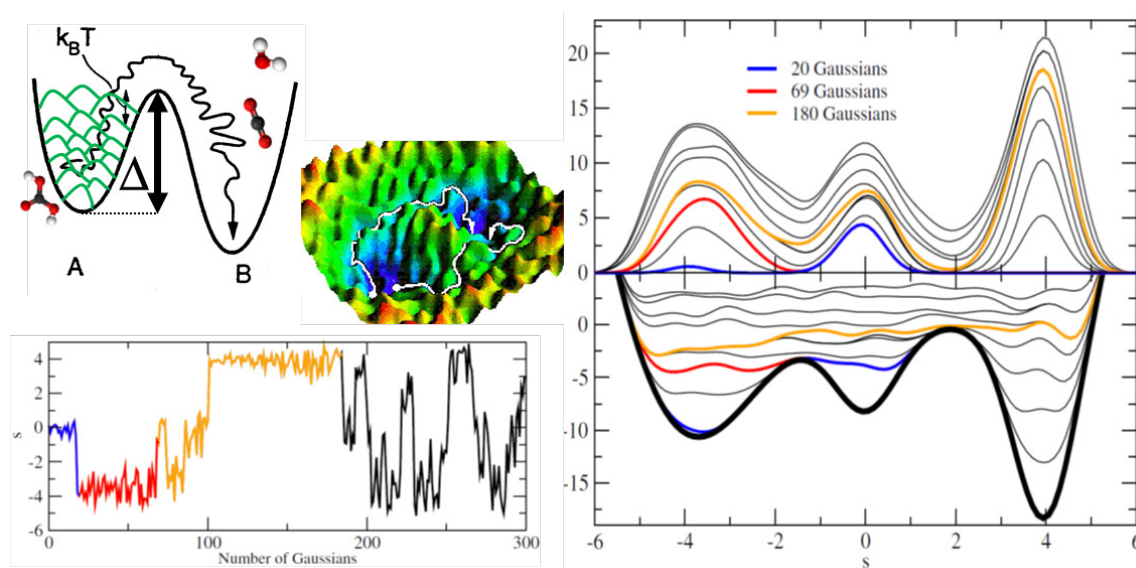


Figure 2.4: Schematic representation of activation barrier for dissociation reaction of H_2CO_3 molecule into CO_2 and H_2O . The activation energy of the reaction is several times the thermal energy vibrations. $\Delta \gg k_B T$. The dissociation can occur instantaneously, if the barrier is eliminated by an external potential. In metadynamics the external potential is incrementally built up by small Gaussian-shaped functions, schematically shown by green lines in the upper left figure. Lower left and right figures show metadynamics based reconstruction of free energy surface for a model system with 2 local and one global minima along the reaction coordinate s . Initially the system is in the state with $s = 0$, an intermediate local minimum. This minimum is filled with first 20 Gaussian functions and the system moves to the state with $s = 3.5$. This second minimum is filled with additional 49 Gaussian functions and the system explores the region in the range of reaction coordinate values from -5 and 3 till global minima is discovered. In total 180 Gaussian functions are needed to rebuild the free energy surface. Continuation of the simulation does not change the relative energy of the minima and the activation barriers, this in the accuracy of the simulation setup. Figure is reproduced with permission (Laio and Gervasio 2008).

The free energy calculations are prone to a number of uncertainties which can significantly influence the simulation results. A thorough discussion of the free energy sampling accuracy by metadynamics is given by Laio et al., 2005 and Laio and Gervasio, 2008. Using a model stochastic system, they have proposed an empirical estimate of the free energy sampling error $\varepsilon(d)$ in analytical form:

$$\varepsilon = C(d) \sqrt{\frac{w\delta s T S}{D\tau_G}} \quad (2.10)$$

w , and δs are the height and width of the Gaussian functions used to sample the free energy, τ_G is the time interval between the deposition of Gaussian functions. The T and D are the effective temperature and diffusivity of the collective variables, respectively. The S is the size of the system, in the space of collective variables, explored by meta-dynamics, and $C(d)$ is a constant proportional to the system dimensionality.

Obviously, T , D and S are the parameters defined by the intrinsic properties of the system. Contrary, the w , δs and τ_G are the simulation parameters, which can be tuned by the simulation setup as natural compromise between the accuracy and efficiency. This semi-empirical equation does not necessary reflect all the details of the complex interplay between the system specifics and simulation setup. Based on the analysis of system dynamics and dependencies of the system parameters it has been suggested that metadynamics could be a very efficient approach for estimations of the energy barriers for a single reaction step and the elucidation of most favourable reaction mechanism. In the same time metadynamics is less suited method for reconstructions the large domains containing numerous local minima basins connected by narrow paths (Laio et al. 2005, Laio and Gervasio 2008).

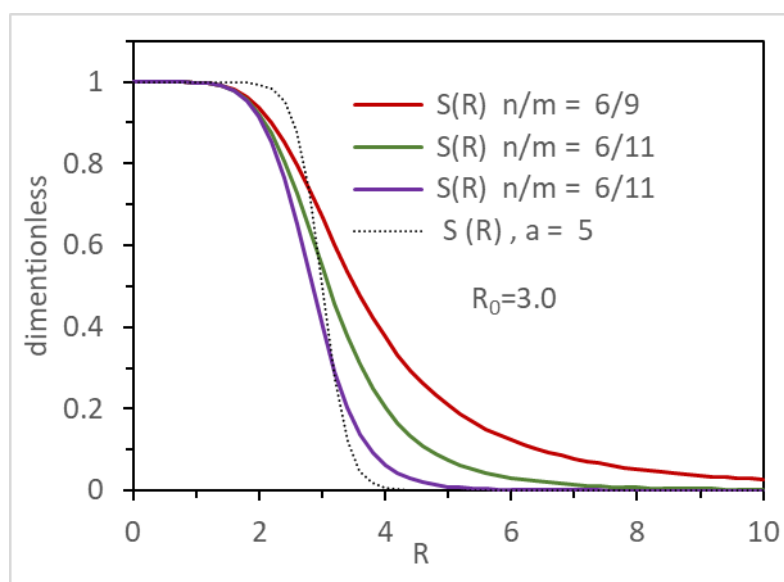


Figure 2.5: Illustration of rational coordination number function (coloured line) with different values of the exponents and Fermi like function (dotted line).

The reaction mechanism in a complex system is a priori unknown and can follow several concurrent reaction pathways. The collective variables (reaction coordinates) should be as general as possible and introduce the least bias to the system description. Coordination number is a useful indicator for the studies of surface complexation phenomena and chemical reactions. The mathematical representation of the coordination number is implemented with a smooth step like function of the interatomic distance, which is close to one when two atoms are coordinating each other and asymptotically go to zero when atoms are apart beyond the coordination distance (see Fig. 2.5). Such distance indicator functions are summed up for all atoms of a specific type in the system to give an integral coordination number on the specific atom(s) or functional groups.

$$S_{ij}^{n,m}(R) = \frac{1-(R_{ij}/R_{0,ij})^n}{1-(R_{ij}/R_{0,ij})^m} \quad (2.11)$$

$$S_{ij}^a(R) = \frac{1}{\exp[\alpha(R_{ij}/R_{0,ij})]+1} \quad (2.12)$$

$$CN_i = \sum_j S_{ij}(R) \quad (2.13)$$

Several mathematical representations of the coordination number functions are possible. Expressions for rational functions and a Fermi like function are given in Eqs. 2.11 and 2.12. These functions are plotted in Fig. 2.5 for a set of different parameters. The parameters $R_{0,ij}$, n and m in the rational function control the steepness and the position of the gradual transition between the coordinated (value close to 1, at short distance) and uncoordinated (approaching zero, long distance). The Fermi function (Eq. 2.12) has a symmetric shape relative to the $R_{0,ij}$. This can be useful for the accurate description of the exchange between the first and the second coordination shell. The rational function (Eq. 2.11) on the other hand is more versatile for the description of the interaction in a complex system due to the asymmetric long-range tail allowing to probe coordination environment beyond the second coordination shell. The coordination number is an integral quantity. The individual atoms are indistinguishable, and the system is thus not biased for the interaction with a particular atom in the system. It is also important to realize that the exact value of such a collective coordination number does not need to be identical to the integer valued structural definition of coordination.

2.6 References

- Becke A. (1988) Density-Functional exchange-energy approximation with correct asymptomatic-behaviour. *Physical Review A* **38**, 3098–3100.
- Dolg M. and Cao X. (2012) Relativistic Pseudopotentials: Their Development and Scope of Applications. *Chemical Reviews* **112**, 403–480.
- Goerigk L. and Grimme S. (2011) A thorough benchmark of density functional methods for general main group thermochemistry, kinetics, and noncovalent interactions. *Physical Chemistry Chemical Physics* **13**, 6670–6688.
- Grimme S., Hansen A., Brandenburg J. G. and Bannwarth C. (2016) Dispersion-Corrected Mean-Field Electronic Structure Methods. *Chemical Reviews* **116**, 5105–5154.
- Grossman J., Schwegler E., Draeger E., Gygi F. and Galli G. (2004) Towards an assessment of the accuracy of density functional theory for first principles simulations of water. *Journal of chemical Physics* **120**, 300–311.
- Hohenberg P. and Kohn W. (1964) Inhomogenous Electron Gas. *Physical Review B* **136**, B864.
- Koch W. and Holthausen M. C. (2015) *A Chemist's Guide to Density Functional Theory.*, Wiley.
- Kohn W. and Sham L. (1965) Self-consistent equations including exchange and correlation effects. *Physical Review* **140**, 1133pp.
- Kuehne T. D., Iannuzzi M., Del Ben M., Rybkin V. V., Seewald P., Stein F., Laino T., Khaliullin R. Z., Schutt O., Schiffmann F., Golze D., Wilhelm J., Chulkov S., Bani-Hashemian M. H., Weber V., Borstnik U., TAILLEFUMIER M., Jakobovits A. S., Lazzaro A., Pabst H., Mueller T., Schade R., Guidon M., Andermatt S., Holmberg N., Schenter G. K., Hehn A., Bussy A., Belleflamme F., Tabacchi G., Gloss A., Lass M., Bethune I., Mundy C. J., Plessl C., Watkins M., VandeVondele J., Krack M. and Hutter J. (2020) CP2K: An electronic structure and molecular dynamics software package - Quickstep: Efficient and accurate electronic structure calculations. *Journal of chemical Physics* **152**.
- Laio A. and Gervasio F. L. (2008) Metadynamics: a method to simulate rare events and reconstruct the free energy in biophysics, chemistry and material science. *Reports on Progress in Physics* **71**.
- Laio A. and Parrinello M. (2002) Escaping free-energy minima. *Proceedings of the national Academy of Sciences of the United States of America* **99**, 12562–12566.
- Laio A., Rodriguez-Forteza A., Gervasio F., Ceccarelli M. and Parrinello M. (2005) Assessing the accuracy of metadynamics. *Journal of physical Chemistry B* **109**, 6714–6721.
- Molina-Montes E., Donadio D., Hernandez-Laguna A. and Ignacio Sainz-Diaz C. (2010) Exploring the Rehydroxylation Reaction of Pyrophyllite by Ab Initio Molecular Dynamics. *Journal of physical Chemistry B* **114**, 7593–7601.
- Molina-Montes E., Donadio D., Hernandez-Laguna A., Parrinello M. and Ignacio Sainz-Diaz C. (2013) Water Release from Pyrophyllite during the Dehydroxylation Process Explored by Quantum Mechanical Simulations. *Journal of physical Chemistry C* **117**, 7526–7532.

- Perdew J. P. (2013) Climbing the ladder of density functional approximations. *Mrs Bulletin* **38**, 743–750.
- Perdew J., Burke K. and Wang Y. (1996) Generalized gradient approximation for the exchange-correlation hole of a many-electron system. *Physical Review B* **54**, 16533–16539.
- Peverati R. and Truhlar D. G. (2012) M11-L: A Local Density Functional That Provides Improved Accuracy for Electronic Structure Calculations in Chemistry and Physics. *Journal of physical Chemistry Letters* **3**, 117–124.
- Peverati R. and Truhlar D. G. (2014) Quest for a universal density functional: the accuracy of density functionals across a broad spectrum of databases in chemistry and physics. *Philosophical transactions of the royal society A-Mathematical physical and Engineering Sciences* **372**.
- Schwegler E., Grossman J., Gygi F. and Galli G. (2004) Towards an assessment of the accuracy of density functional theory for first principles simulations of water. II. *Journal of chemical Physics* **121**, 5400–5409.
- Troullier N. and Martins J. (1991) Efficient pseudopotentials for plane-wave calculations. *Physical Review B* **43**, 1993–2006.
- Vanderbilt D. (1990) Soft self-consistent pseudopotentials in a generalized eigenvalue formalism. *Physical Review B* **41**, 7892–7895.

3. Dissolution mechanism of Pyrophyllite starting at the (110) edge

The text of this chapter is published as:

René Schliemann & Sergey V.Churakov (2021) "Atomic scale mechanism of clay minerals dissolution revealed by ab initio simulations" *Geochimica et Cosmochimica Acta*, 293, 438-460.

Abstract

Large-scale ab initio Meta-Dynamics simulations were applied to elucidate the molecular mechanism and reaction free energies of pyrophyllite dissolution at the (110) edge surface in pure water at close to neutral pH under far from equilibrium conditions. The simulation setup allows realistic representation of the clay mineral surface and explicit consideration of solvent dynamics at finite temperature. The simulation reveals that dissolution of a single tetrahedral or an octahedral unit from the clay mineral edge is a complex multi-step process with several reaction intermediates. Typically, each reaction step changes denticity of the reacting site in a step-by-step manner and leads, eventually, to the leaching of ions forming octahedral and tetrahedral sheets of the phyllosilicate. The solvent rearrangement and the proton transfer reactions in the first and the second coordination shell of the dissolving unit play a critical role in the stabilization of reaction intermediates and the net progress of the dissolution reactions. The overall reaction mechanism can be rationalized as sequence of concurrent and reversible elementary reaction events, which are:

- 1) the nucleophilic attack of H₂O molecules or OH groups on the dissolving surface site
- 2) ligand exchange reactions in the first coordination shell of the reacting sites leading to changes of its conformation and denticity at the mineral surface
- 3) collective proton transfer reactions between the acidic and basic oxygen sites mediated via a chain of the hydrogen bonded molecules in the first and second coordination shell of the reacting site.

The results obtained in this study are general and applicable to the group of 2:1 phyllosilicates in a wide range of chemical and thermodynamic conditions.

3.1 Introduction

Clay minerals are ubiquitously present in soils, fine-grained argillaceous sediments and shales. They are formed through weathering and hydrothermal alteration of felsic and mafic rocks respectively or by direct sedimentation in marine environment (Brigatti et al., 2006). Due to high specific surface area and large pH buffering capacity, clay minerals play an important role in supporting bio-geochemical and low-grade metamorphic reactions (Dong et al., 2003; Kamp, 2008; Voinot et al., 2013a). It has been speculated that clays could have contributed to the prebiotic synthesis of simple amino acids and sugars or assisted in the enrichment of L-over R-optical isomers of amino acids as a result of the chiral selective adsorption (Ponnamperuma et al., 1982). Various hazardous metal can be efficiently immobilized on the surface of clay mineral or even incorporated in the clay mineral structure (B Baeyens and Bradbury, 1997; Bradbury and Baeyens, 2005, 2011; Fernandes et al., 2015; Wick et al., 2018).

This property of clay is used in the engineered disposal site for deposition of radioactive waste or for the protection of the environment from chemical pollution (Altmann, 2008).

Clay minerals belong to a larger group of phyllosilicates. The phyllosilicates possess a common structural motif represented by the sheets of octahedral coordinated cations, mainly Al and Mg (octahedral sheet, (O)), and tetrahedrally coordinated Si and Al (tetrahedral sheet, (T)). Mineral pyrophyllite (Fig. 3.1) can be considered as a structural prototype for a large variety of 2:1 phyllosilicates, such as smectites, illites and micas. In pyrophyllite, two thirds of octahedral sites are occupied by Al and one third of octahedral sites are vacant. The octahedral sheet is sandwiched between two Si tetrahedral sheets forming a TOT layer altogether. The TOT layer of pyrophyllite is electrostatically neutral. The structure of other 2:1 phyllosilicates can be derived from pyrophyllite by substituting certain amount of Al^{3+} in the octahedral sheet with divalent cations such as Mg^{2+} and Fe^{2+} (common for smectites) and/or substituting Al^{3+} for Si^{4+} in the tetrahedral sheet (common for illites and micas). These substitutions contribute to the permanent structural charge of the TOT layer, which are compensated by cationic species entering the interlayer space between the TOT layers. The electrostatic and van-der-Waals interactions contribute to the stacking of the TOT layers parallel to the {001} crystallographic plane. In smectites (low structural charge, less than 0.2 per formula unit), the interaction energy between neighbouring interlayers is weak compared to the hydration of the interlayer cations (Whitley and Smith, 2004; Smith et al., 2006; Rotenberg et al., 2009). These minerals show free swelling behaviour caused by H_2O molecules entering the interlayer space (Mooney et al., 1952; Eypert-Blaison et al., 2002; Paineau et al., 2011a, b).

Platelet morphology of smectite and illite minerals results in an exceptionally large surface area, which can be as high as $800\text{ m}^2\text{g}^{-1}$ (Tournassat et al., 2003). The main contribution to the total measurable surface area has the basal {001} plane enclosing the interlayer space. This surface is fairly unreactive in a wide range of pH conditions (Bickmore et al., 2001; Brandt et al., 2003; Kuwahara, 2008). Moreover, in the highly compacted smectites at low hydration state and in illites, the interlayer space remains inaccessible to the pore water solution. The external basal surface of stacked illite-smectite particles comprise only $30\text{-}120\text{ m}^2\text{g}^{-1}$ (Tournassat et al., 2003; Metz et al., 2005b).

The basal surface has a strong tendency to adsorb water (Mooney et al., 1952; Salles et al., 2009) due to the interaction with surface structural charge and the ions in diffuse double layer. (Wang et al., 2005; Botan et al., 2011; Churakov, 2013; Tournassat et al., 2013; Szczerba et al., 2020). The basal surface contributes to cation sorption by electrostatic interaction. In contrast, the lateral edge surfaces of phyllosilicate platelets, only $4\text{-}9\text{ m}^2\text{g}^{-1}$ (Tournassat et al., 2003; Metz et al., 2005b) are highly reactive and change its electrochemical properties as a function of pH. The morphology and preferential stability of edge facets in clays has been investigated experimentally and by theoretical modelling (Bosbach et al., 2000; Bickmore et al., 2001, 2003; Kuwahara, 2006a; Kurganskaya et al., 2012). Quantum mechanical simulations based on geometry optimization revealed preferential stability of (010) and the (110) surfaces (Bickmore et al., 2003; Churakov, 2006, 2007; Churakov and Liu, 2018). The preferred occurrence of the (010) and the (110) edge sites is related to the high density and the strength of the bond chain running parallel to these lattice planes (Hartman and Perdok, 1955; White and Zelazny, 1988). These edges were found to be responsible for the adsorption of transition metals (Liu et al., 2008; Churakov and Dähn, 2012; Kremleva et al., 2012; Zhang et al., 2017, 2018). Depending on pH, the surface sites participate in protonation and deprotonation reactions (Bart Baeyens and Bradbury, 1997; Duc et al., 2006; Bradbury and Baeyens, 2009). These reactions change the surface charge and control the dominant sorption mechanism of the cations. At low pH the surface site becomes preferentially protonated and the edge has

net positive charge density. At high pH, the basal plane possesses net negative charge due to the deprotonation of dangling OH sites coordinating Si tetrahedra and Al octahedra. The net negative surface charge and deprotonation promote adsorption of cations at the edge surface by the sorption complexation mechanism (Bradbury and Baeyens, 2005).

The surface complexation of metals is closely related to the reactivity and dissolution/precipitation processes at the edge sites. There are a number of experimental evidences indicating that the surface complexation act as a precursor for neo-formation of phyllosilicates (Dähn et al., 2002, 2003; Schlegel and Manceau, 2006; Soltermann et al., 2014b, a). Both, neo-formation of phyllosilicates and concurrent dissolution/precipitation reactions are particularly important for the irreversible retention of hazardous cations. The structural incorporation requires recrystallization of the solid leading to dissolution of pristine material and precipitation of a new phase.

Macroscopic dissolution kinetics of phyllosilicate has been studied in batch sorption experiments at ambient and elevated temperatures in wide range pH conditions (Walther, 1996; Bauer and Berger, 1998; Bickmore et al., 2001; Amram and Ganor, 2005; Metz et al., 2005a; Brantley et al., 2008; Marty et al., 2011a; Robin et al., 2016). Measured dissolution rates exhibit a typical V-shape variation as a function of pH. The dissolution rate is minimal close to neutral pH. The exact position of the minima is, however, varying from mineral to mineral and may depend on the extent of isomorphic substitutions in the octahedral and tetrahedral sheets of phyllosilicates (Oelkers et al., 2008). The apparent dissolution rates decrease with increasing pH at acid conditions and increase with increasing pH at basic conditions (Köhler et al., 2003). The pH dependence is typically stronger for basic than for acidic conditions. The rate controlling mechanism has been a subject of debate. Several experimental studies observe the reaction rate to decrease with time. The initial dissolution is often found to deviate from congruent dissolution (Turpault and Trotignon, 1994; Amram and Ganor, 2005; Marty et al., 2011b; Voinot et al., 2013b), which is typically observed for long term dissolution rates. These observations are explained by changes of the overall reactive surface area upon alteration of the clay particle morphology while dissolving. Fast initial nonstoichiometric dissolution rate can also be attributed to the dissolution of initial fine grain particles or the presence of surface coating (Köhler et al., 2003).

The aqueous speciation sampled in long-term dissolution was on the other hand found to be consistent with the congruent dissolution model (Cama et al., 2000; Metz et al., 2005a; Robin et al., 2016). The existence of the steady state rate has been questioned however, since the surface topography undergo a complex transformation as the reaction proceeds (Köhler et al., 2005). It has been generally argued that the dissolution advances with a step-by-step removal of tetrahedral and octahedral units at TOT layers from the edge surfaces of clay particles. An important precursor for this mechanism is the nucleation of etch pits associated with point defects and screw dislocations at the basal surface (Kurganskaya et al., 2012; Kurganskaya and Luttge, 2013). This view is strongly supported by in situ and ex situ AFM observations of phyllosilicate reactivity (Snowdeniff et al., 1993). The observations of zig-zag patterns on the basal plane of illite particles suggest the presence of screw dislocation responsible for spiral growth or dissolution mechanism (Kuwahara et al., 1998, 2001). The observed morphology of the clay particles is consistent with the preferential stability of the most common {110} and {010} edge sites surfaces (Kuwahara, 2006a). Various functional relationships proposed for the pH and temperature dependent description of phyllosilicate mineral dissolution (Köhler et al., 2003; Amram and Ganor, 2005; Golubev et al., 2006; Voinot et al., 2013b) can be reduced to a linear dependence on the activity of H_2O , H_3O^+ and OH^- . The measured reaction order 0.2-0.6 for phyllosilicate, indicates a complex reaction mechanism, involving several reaction

steps. These values are consistent with the one reported for other aluminosilicates (Brantley et al., 2008).

Analysis of kinetic data for various aluminium silicates suggest that the pH dependence of the dissolution rate is primarily related to the change in the surface charge density as the charged surface complexes polarize and weaken the Al-O and Si-O bonds and thus facilitate the dissolution (Walther, 1996). The intrinsic acidity of the surface group at the edge sites was investigated in detail by ab initio simulation (Churakov, 2006; Liu et al., 2013, 2014, 2015a). The modelling results demonstrate large variability of the surface OH group's acidity constants depending on their structural position and the presence of isomorphic substitutions in the tetrahedral or octahedral sites (Churakov and Liu, 2018). The effective acidity of the surface sites is known to be influenced by the presence of adsorbed ions (Kubicki et al., 2012; Pfeiffer-Laplaud et al., 2016) and this will depend on the ionic strength of the solution and the surface speciation (Delhorme et al., 2010). Additional complexity is related to water dynamics and proton transfer reactions at the surface of 2:1 phyllosilicates (Churakov et al., 2004; Churakov, 2007; Molina-Montes et al., 2013). It is generally accepted that the rate-limiting step for dissolution of aluminium silicates is thought to be the hydrolysis of Si-O-Si and Si-O-Al bonds (Xiao and Lasaga, 1994). While the broad experimental evidence for the proton assisted dissolution mechanism of silicate exists (Brantley et al., 2008), the detailed mechanism of this process remains unresolved. An adequate description of these phenomena needs application of large-scale quantum mechanical simulations, which are computationally expensive. Finally, the slow dynamics of water and ions at the mineral fluid interface makes the direct observation of dissolution phenomena by direct quantum mechanical simulation in presence of water and electrolyte virtually impossible.

In this work, we apply ab initio MetaDynamics (MetaD) simulations (Laio and Parrinello, 2002; Laio et al., 2005) to directly evaluate the dissolution mechanism and the activation energy of Al and Si leaching on an idealized (110) edge surface of pyrophyllite in pure water. The MetaD approach is able to integrate the degree of freedom related to water dynamics and to describe the dissolution mechanism in terms of a few collective variables related to the change of the coordination and speciation of aluminol and silanol groups. The simulations mimic far from equilibrium leaching in aquatic environment. The pyrophyllite can be seen as the simplest structural prototype for the large variety of 2:1 phyllosilicates. In contrast to the majority of the studies of mineral reactivity performed for cluster calculation, our work does explicitly account for the mineral surface geometry as well as finite temperature dynamics of solvent molecules in first and second coordination shell of reacting surface sites. The simulations provide deep insight into atomic scale details on the step by leaching of tetrahedral and octahedral units at phyllosilicate surface.

3.2 Methods

3.2.1 System setup

The simulation system was represented by one TOT-layer with (110) edge surfaces built on the basis of an ideal pyrophyllite structure (Fig. 3.1). A slit pore between (110) edge surfaces was filled with water molecules to represent the interface with bulk water. 3D periodic boundary conditions were applied throughout the simulations. The initial system dimension between the TOT layers was set to 10 Å. The independent simulations were performed using supercells with two unit cells in [100] crystallographic direction of pyrophyllite corresponding to (10.4 Å). The size of the slit pore was adjusted to accommodate a necessary amount of water molecules (60 molecules) between the edge surfaces, so that the fluid in the center of

the pore resembles bulk water properties. This scoping calculations and pre-equilibration of the system were performed with classical simulation as described in the next paragraph. The supercell dimension in direction normal to the interface was 39.3 Å.

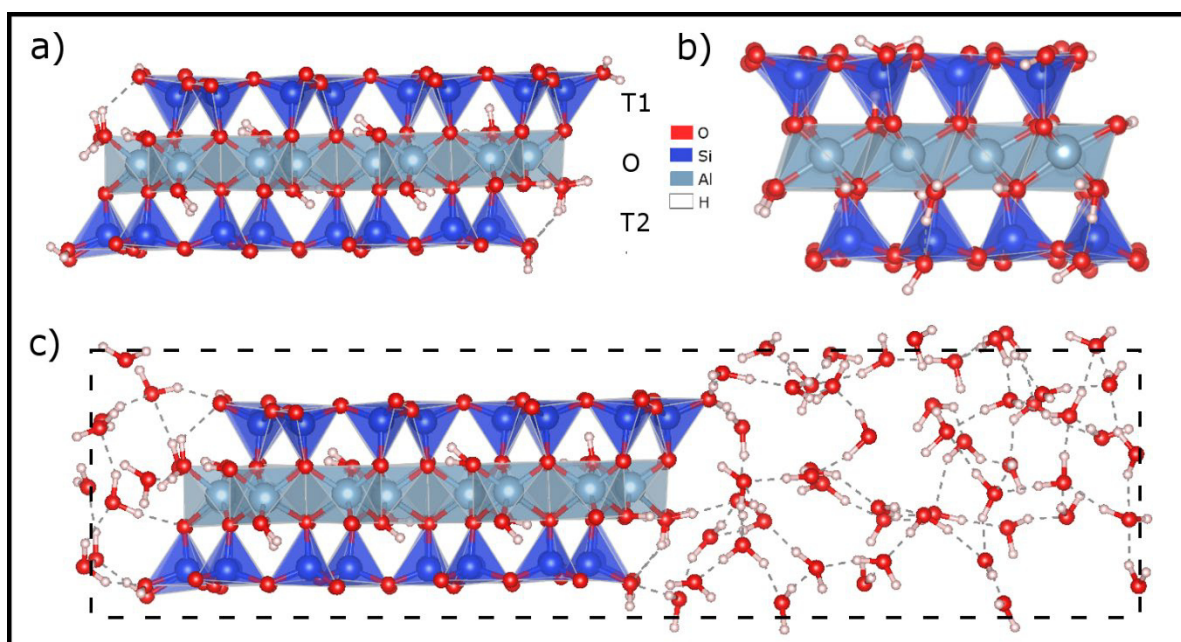


Figure 3.1: A snapshot from MD simulations showing the structure of (110) edge surface of Pyrophyllite a) side view and b) front view of clay platelet without water for the sake of clarity, c) Side view of supercell showing the slit pore filled with water and the bounding box of the super cell. Si tetrahedra with different surface symmetry, investigated in this work are indicated as T1 and T2 (Si_{T1} and Si_{T2} , respectively) and O (octahedral sheet with $\text{Al}(\text{O})$). The color code of the species is given next to the side view in a).

Prior to the ab initio equilibration and production MD runs, the distribution of water molecules in the slit pore was pre-equilibrated in NVT ensemble (constant Volume, Temperature and Number of particles) at 300K for at least 1 ns using the CLAYFF force field (Cygan et al., 2004a) keeping the atomic positions of the clay particle frozen at their equilibrium position obtained by ab initio geometry optimization. This classical pre-equilibration runs were used to adjust the box size in b(y)-direction adjusting number of water molecules in the system until water-like density in the middle of the water layer was obtained. Further detail of the simulation setup is provided in the Supporting Information. The obtained molecular configuration was used as initial conditions for actual equilibration of the system by the ab initio simulations described in the next section.

3.2.2 Ab initio MD

Ab initio molecular dynamic calculations were conducted using the density functional theory (DFT) with the PBE-D3 exchange-correlation functional (Perdew et al., 1996) augmented with dispersion correction after Grimme (Grimme, 2004). The core electrons were described using norm-conserving dual space Goedecker-Teter-Hutter pseudopotentials (Goedecker et al., 1996). The valence electron wave-functions were represented by DZVP Gaussian basis set (VandeVondele and Hutter, 2007). The auxiliary electron density was represented with plane wave (PW) basis sets up to the kinetic energy cutoff 400 Ry. The MD simulations were performed in the Born-Oppenheimer approximation. Equations of motion for atoms was integrated with 0.5 fs time step. The simulations were performed at 300 K in the NPT

ensemble, thermostating the system using the Canonical Sampling Velocity Rescaling (CSVR)-thermostat (Bussi et al., 2007). This setup model parameters have been proven to reproduce structural data for clay minerals in our previous simulations (Keri et al., 2017, 2019). Before the start of the ab initio MetaDynamics run the system was equilibrated for 2 ps. The equilibration was monitored by convergence of thermodynamic properties of the system to the constant averages.

3.2.2.1 MetaDynamic simulations

The activation energy for the dissolution of aluminosilicate minerals is expected to be on the order of 50 to 100 kJ · mol⁻¹ (Bauer and Berger, 1998; Amram and Ganor, 2005; Aldushin et al., 2006; Kuwahara, 2006a, 2008), which is much larger than the typical magnitude of thermal fluctuations at room temperature ($k_B T \sim 2.5 \text{ kJ} \cdot \text{mol}^{-1}$). Therefore, a spontaneous dissolution of clay minerals cannot be observed by standard MD simulations (Churakov, 2007; Churakov and Kosakowski, 2010). In this study, the free energy surfaces (FES) for the detachment of tetrahedral and octahedral sites were directly sampled by the MetaD method (Laio and Parrinello, 2002; Iannuzzi et al., 2003). With this approach, the progress of reaction is monitored by a set of reaction coordinates or more generally collective variables (CV). The CVs are generic functions of atomic positions that are able to discriminate the configurations corresponding to reactants, products and transition states of interest. The CVs used in this work are the coordination numbers (CN) for atom I given by the following equation:

$$CN_I = \sum_{j=1}^{N_j} \frac{1 - \left(\frac{R_{Ij}}{R_{0Ij}}\right)^i}{1 - \left(\frac{R_{Ij}}{R_{0Ij}}\right)^k}, \quad (3.1)$$

where j is the index of the species coordinating the atom of interest, i and k are exponents, R_{0Ij} , are the characteristic bond length parameters depending on the atom types involved and R_{Ij} is the actual bond distance between atoms I and j.

Table 3.1: Parameters used for the CN of different neighbouring elements during MetaD run.

	Al-Al	Al-Si	Al-O	Si-O	O-H
R_0 in Å	3.4	3.4	2.4	2.4	1.2
i	20	21	18	18	25
k	12	12	10	10	20

The parameters used for the different combinations of atom types I and j in equation 3.1 are given in Table 3.1. The choice of i, k and R_{0Ij} was made in order to have a smooth change from a bonded to the disrupted state between two atoms and vice versa (see further explanation and Fig. 3.S9 in supplementary). For the MetaD simulations a multiplication of two equations like Eq. 3.1 was used to specifically consider the coordination with hydroxyl groups (one with Si-O and the second with O-H), which corresponds to coordination with oxygen and number of hydrogens surrounding these. In our previous work, a similar set of collective variables was applied to elucidate the de-hydroxylation reaction on brucite surface (Churakov et al., 2004). The four MetaD simulations discussed in this study all took three CVs into account to scan the free energy surface. The three CVs used were CN(Si-OH), CN(Si-OSi) and CN(Si-Al) or CN(Al-OH), CN(Al-Si) and CN(Al-Al) in case of the Al detachment.

In MetaD simulations, the system is pushed away from the local energy minima configuration, which it is currently occupying, by means of a time dependent external potential composed

of the sum of Gaussian like functions in the space of selected CVs. Such hill-like Gaussian penalty functions are added progressively to the external potential boosting the system to explore the configurational space. For a sufficiently long simulation run the collected external potential has been shown to represent the free energy surface of the system in the space spanned by the CVs (Laio and Parrinello, 2002). Moreover, the generated trajectories typically resemble the minimum energy path (MEP) between the reaction intermediates. Further analysis of the FES allows to reveal the multiple competitive reaction mechanisms. The method has been successfully applied to reactions on mineral surfaces and structural transformation in clay minerals (Molina-Montes et al., 2010, 2013).

Typically, a successful detachment and solvation of an atomic site could be obtained in a 50-100 ps long MetaD trajectory. In this study, several ab initio MD trajectories with total length of nearly 300ps were simulated for the detailed analysis of pyrophyllite dissolution mechanism on (110) edge. The code we use to conduct the MetaD calculations is CP2K with Quickstep (VandeVondele et al., 2005) and the thermostat together with the barostat applied is the canonical sampling through velocity rescaling (CSVR) (Bussi et al., 2007).

3.2.3 Uncertainties

The calculation of thermodynamic quantities from first principles is challenging and can be prone to a number of systematic errors. Therefore, possible uncertainties in the simulation results need to be carefully examined. The errors associated with the DFT are well documented and are mainly related to the performance of exchange and correlation functionals. The PBE functional combined with the dispersion correction is expected to reproduce the structural parameters of the clay mineral within 1% accuracy (Tunega et al., 2012) and the mean square deviation of bonding energy was estimated by different datasets to be within $2.9\text{--}10.5 \text{ kJ} \cdot \text{mol}^{-1}$ (Grimme et al., 2016). These are the minor uncertainties compared to the intrinsic errors related to the limited sampling and the parameter choice for the MetaD simulations. The nature of uncertainties in MetaD simulations are thoroughly discussed in a number of studies from (Laio et al., 2005; Laio and Gervasio, 2008). The major sources of the modelling uncertainty are related to the Gaussian's hill size and the time interval between the hills sampling. The equilibration interval between hills sampling is closely linked to the diffusivity in the system. For the system considered in this study the slow diffusive motion of solvation molecules is the main limiting factor. The hill size used in the modelling was $7.88 \text{ kJ} \cdot \text{mol}^{-1}$. Thus, the uncertainty in FES estimate is at best $15.8 \text{ kJ} \cdot \text{mol}^{-1}$. Substantial error can be associated with neglecting the necessary degree of freedom relevant to the reaction mechanism. The errors are particularly difficult to estimate since relevant CVs are not known a priori. In general, weak selectivity of CV with respect to different reaction intermediates leads to an overestimate of the activation barrier.

3.3 Results

3.3.1 Atomic scale dissolution mechanism

In this work we investigate the initial stage of etch pitting on idealized fully hydrated (110) surface of pyrophyllite. This edge surface has two structurally different Si tetrahedra referred as $\text{Si}_{\text{T}1}$ and $\text{Si}_{\text{T}2}$, and Al octahedral position (Fig. 3.1). If started from a lowest energy configuration, the sequence of structures obtained in MetaD simulations would typically follow the MEP. Sequence of snapshots illustrating reactants, products, intermediates and activation complexes (transition states) corresponding to the detachment of Si-tetrahedra and

Al-octahedra from the surface are shown in Figs. 3.2-3.27. Given the system complexity, the reaction mechanism observed in the simulation trajectory may be not unique. Instead, it may represent one of the possible concurrently occurring reaction pathways. Alternative reaction mechanisms, described in terms of collective variables and the activation barrier values, could be inferred from the analysis of the cumulative FES at the end of the simulations. The following section provides a detailed analysis of the molecular trajectories leading to Si and Al detachment from the surface.

3.3.1.2 Si_{T1} detachment mechanism

On an ideal (110) surface, Si_{T1} is coordinated with two Si-O_b-Si bridging oxygen atoms, one Si-O_b-Al bridging oxygen (O(i) + O(iv) and O(iii), respectively) and one dangling OH group (see Fig. 3.2 a and d). Following notation (OH) – Si_{T1}(2) – O – Al is used to describe the coordination of reacting unit (Si_{T1}(2)), where number in brackets indicates the count of bridging oxygen sites coordinating the corresponding silicon atom, if they are not explicitly written in the formula. The same notation is applied to the Al species, where the number in brackets indicates the count of bridging oxygens and bridging OH groups. Such counting of bridging oxygen sites is consequently used in the reaction equations throughout the chapter.

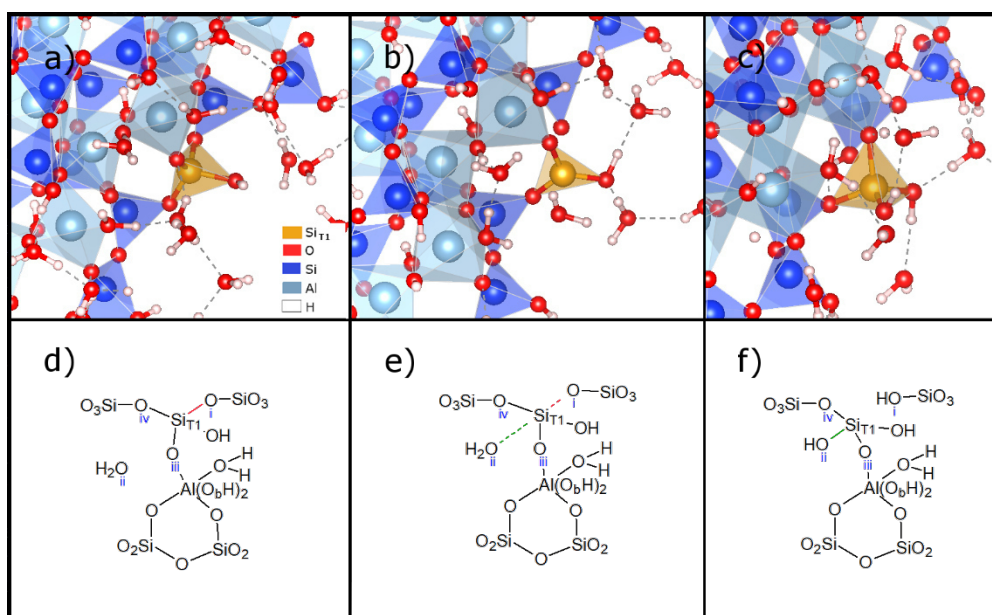


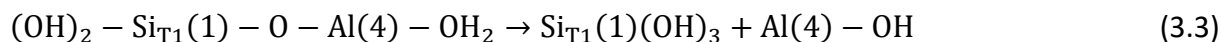
Figure 3.1: First step of the Si_{T1} leaching, in which a bidentate complex (c and f) is formed as a result of a nucleophilic attack of a water molecule (b and e), the rupture of Si_{T1}-O(i) bond and the subsequent protonation of the dangling oxygen site O(i)-Si site (see Eq. 3.2).

The leaching of a Si_{T1} site from the (110) edge surface starts with a nucleophilic attack by a water molecule approaching from the slit pore. The silicon atom moves towards the water oxygen (O(ii)) and elongates its Si-O(i) bond (Fig. 3.2). After the breaking of Si-O(i) bond, a proton from the (O(ii)H₂) group is transferred to the dangling oxygen site (O(i)) through a chain of hydrogen bonds. This reaction step can be formalized as follow:



In the second step, the bidentate complex of Si_{T1} (two bridging oxygen connected to the surface) transforms to a monodentate (one oxygen bridge to the surface) complex by breaking the O(iii)-Al bridging bond to the octahedral sheet (Fig. 3.3). The under-coordinated oxygen

O(iii) accepts a proton from the O(viii)H₂ group coordinating Al site. The proton transfer event is mediated through a chain hydrogen bonds (HB) formed by water molecules in the first and the second coordination shell. The resulting reaction intermediates are illustrated in Fig. 3.3 (c) and (f), where the detaching tetrahedra is pointing towards the pore space. This reaction step can be expressed with the following equation:



In the subsequent reaction steps the Si tetrahedra tilts and forms hydrogen bonds to the surface oxygen sites of the tetrahedral sheet (Fig 3.4 b,e). The mono-dentate tetrahedral complex accepts HB from the surface hydroxy group (O(v)H) and donated O(ii)H hydrogen bond to the O(v). Further conformational changes of Si_{T1} lead to a neo-formation of Si-O(ii) bond, after which O(ii) donate the proton to O(v)H group. The neo-formed H₂O(v) leaves the surface, thus regaining the fourfold coordination of the Si site. This reaction step can be written as the following equation:

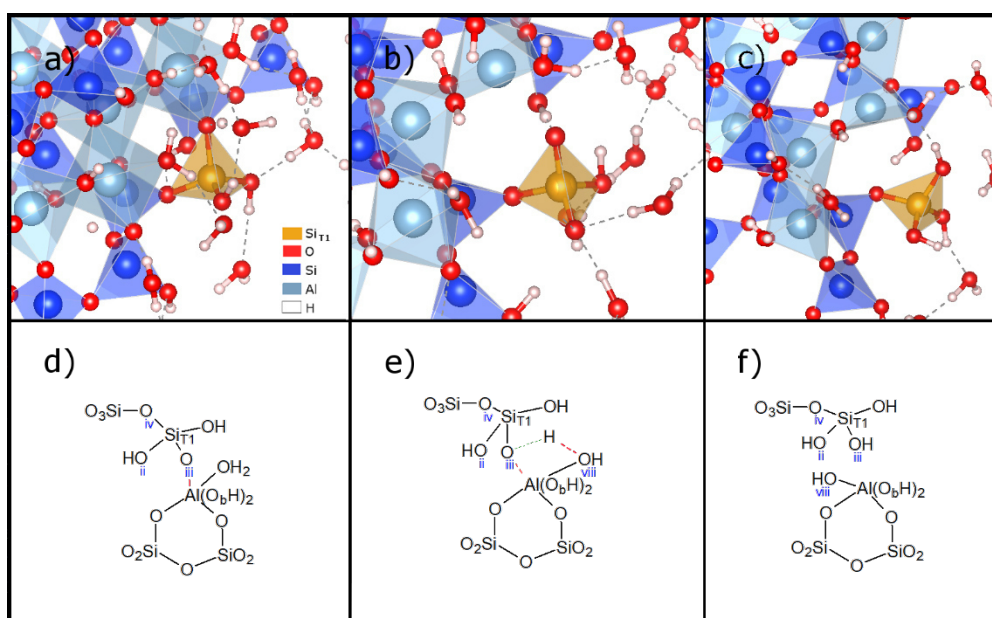
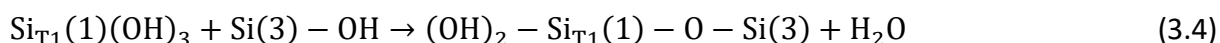


Figure 3.2: Intermediate step of the Si_{T1} detachment reaction (see Eq. 3.3). In this step the bond to the octahedral sheet breaks and the dangling oxygen site O(iii) (see b and e) becomes protonated by one of the protons from the O(viii)H₂ group. The reaction step result in formation of an intermediate structure with a mono-dentate Si_{T1} complex (in c and f).

The neo-formed bidentate Si_{T1} is exposed to a nucleophilic attack by a water molecule (O(vi)H₂) (Fig. 3.5). In this intermediate reaction step, the detaching Si is located between the bridging oxygen and the approaching water molecule. Similar to the reaction described in Eq. 3.2 water molecule enters the coordination of the Si_{T1}. This increases the coordination of Si_{T1} and leads to the elongation and subsequent rupture of the Si_{T1}O(iv) bond. As a follow up of the bond breaking event, the under coordinated O(iv) accepts a proton from O(vi) site by a collective proton transfer through a chain of hydrogen bonds (HBs) (Eq. 3.5).

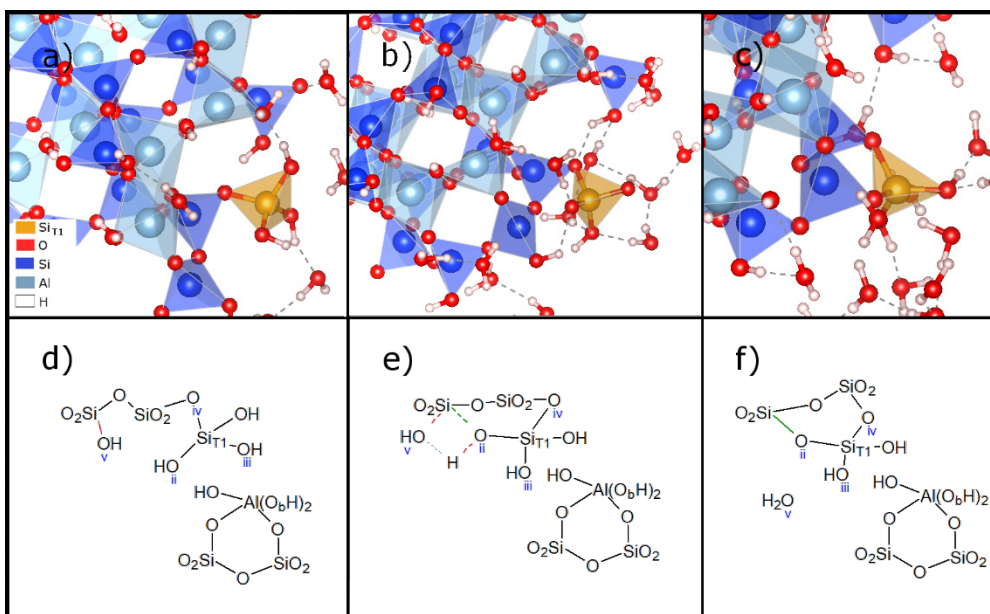


Figure 3.3: Intermediate step of the $\text{Si}_{\text{T}1}$ detachment, in which the detaching Si re-adsorb to the tetrahedral sheet and forms a bidentate complex again (see Eq. 3.4). The precursor to the bond formation is the hydrogen bonding between $\text{HO}(\text{ii})\text{-Si}_{\text{T}1}$ and neighbouring $\text{Si-O}(\text{v})\text{H}$, respectively (see a and d).

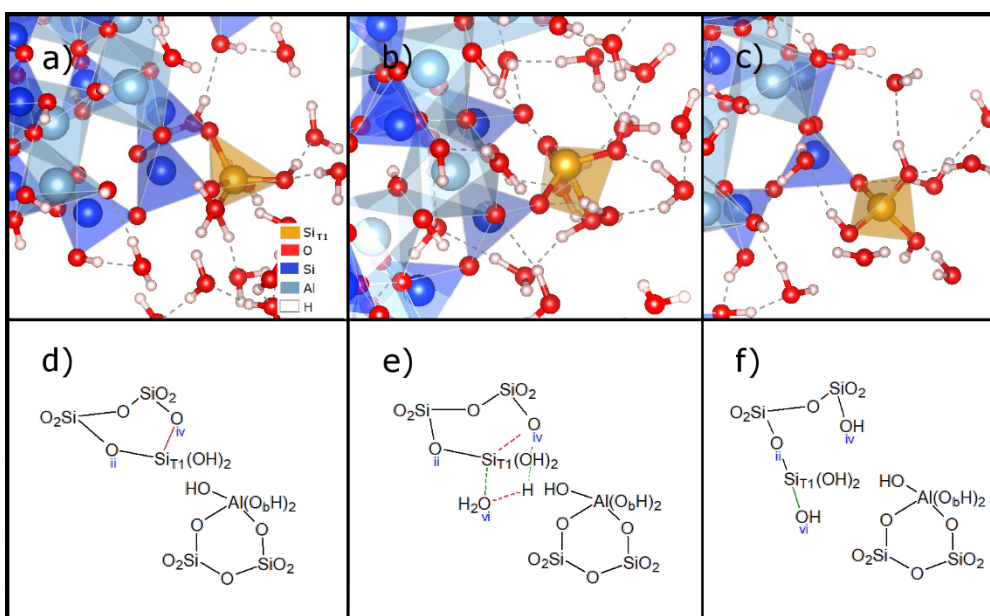
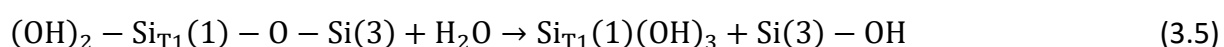


Figure 3.4: Nucleophilic attack on a bidentate $\text{Si}_{\text{T}1}$ complex by a water oxygen ($\text{O}(\text{vi})$), that triggers the rupture of the $\text{Si}_{\text{T}1} - \text{O}(\text{iv})$ bond (see Eq. 3.5). The monodentate complex resulting can be seen in c and f.

The resulting mono-dentate reaction intermediate is the precursor to the last reaction step leading to the detachment of Si tetrahedra from the surface.



In the last reaction step, another water molecule attracts the mono-dentate $\text{Si}_{\text{T}1}$ complex causing elongation of the remaining $\text{Si}_{\text{T}1}\text{-O}$ bond, which connects the complex to the surface. The $\text{Si-O}(\text{ii})$ bond breaks and an aqueous complex $\text{Si}(\text{OH})_4$ forms. In the rest of the molecular dynamics trajectory $\text{Si}(\text{OH})_4$ undergoes a series of structural transformations form an

hydrogen bonded inner-sphere complex to a solvent separated outer-sphere complex and eventually leaves the surface. The last reaction step can be written as the following equation:

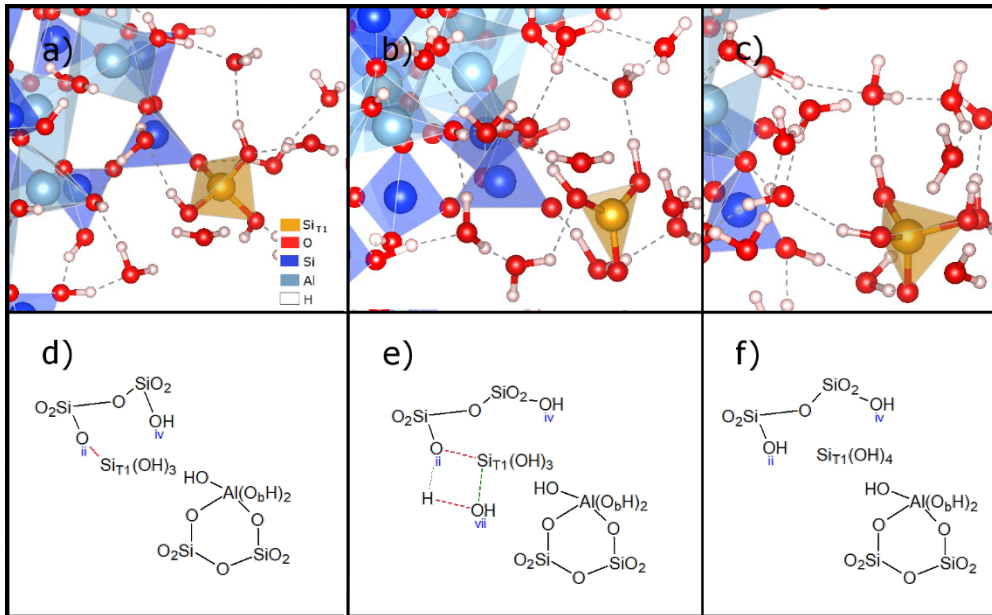
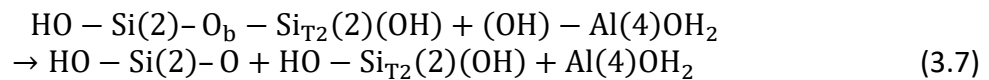


Figure 3.5: Last step of the $\text{Si}_{\text{T}1}$ detachment reaction finalizing the multi-step leaching of $\text{Si}_{\text{T}1}$ tetrahedra (see Eq. 3.6). In this reaction step, the $\text{Si}_{\text{T}1}$ undergoes a nucleophilic attraction by a water molecule ($\text{O}(\text{vii})\text{H}_2$) leading to the local increase of the coordination and subsequent elongation of the $\text{Si}_{\text{T}1}\text{-O}$ bonds. Eventually, $\text{Si}_{\text{T}1}\text{-O}(\text{ii})$ bond breaks and the neo-formed $\text{Si}(\text{OH})_4$ molecule leaves the surface.

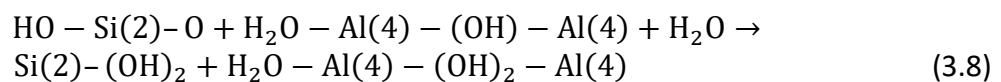
3.3.1.3 $\text{Si}_{\text{T}2}$ detachment mechanism

Due to the monoclinic symmetry of the pyrophyllite crystal, the access of water to the $\text{Si}_{\text{T}2}$ site at the (110) edge is sterically hindered (Churakov, 2006). Consequently, water molecules cannot participate in the initial step of the hydrolysis at the pristine surface and the dissolution follows an alternative pathway compared to the $\text{Si}_{\text{T}1}$ detachment described in the previous section.

The first reaction step observed in the simulations is the hydrolysis of $\text{O}_\text{b} - \text{Si}_{\text{T}2} - \text{O}_\text{b}$ bond assisted by an OH-group donated by the octahedral sheet of the clay mineral (see Eq. 3.7). The intermediate five-fold coordination of $\text{Si}_{\text{T}2}$ site reduces to four-fold again when $\text{Si-O}_\text{b}\text{-Si}$ bond breaks and $\text{O}_\text{b}(\text{v})$ oxygen leaves the coordination shell of the $\text{Si}_{\text{T}2}$ site (see Fig. 3.7). The neo-formed bidentate complex is stabilized by strong hydrogen bonds between the $\text{HO}(\text{v}) - \text{Si}_{\text{T}2}$ group and the dangling oxygen site.



In the next step, another water molecule enters the coordination shell of $\text{Al}(4)\text{OH}_2$ and, a proton is transferred from $\text{Al}(4)\text{O}(\text{ii})\text{H}_2$ to the dangling oxygen site $\text{Si}(2) - \text{O}(\text{v})$. The six-fold coordination of the Al site is restored (Fig. 3.8), whereas $\text{Si}_{\text{T}2}$ site retains bidentate configuration. The reaction step can be summarized as follow:



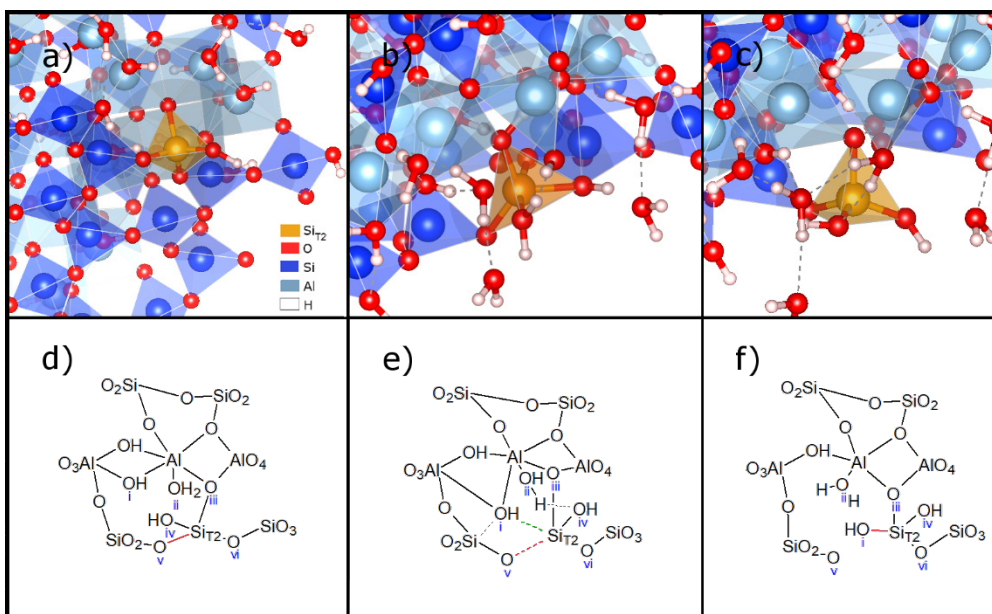


Figure 3.6: First step of the $\text{Si}_{\text{T}2}$ leaching reaction (see Eq. 3.7). The $\text{Si} - \text{O}_{\text{b}}(\text{v})$ bond to one of the neighbouring $\text{Si}(\text{t})$ breaks after a nucleophilic attack of the hydroxyl group ($\text{OH}(\text{i})$) donated by the octahedral sheet. The CN of $\text{Si}_{\text{T}2}$ activated complex increases to five (b and e) whereas the CN of the two $\text{Al}(\text{o})$ sites decreases from six to five. The resulting bidentate complex of $\text{Si}_{\text{T}2}$ regains the CN of four (c and f).

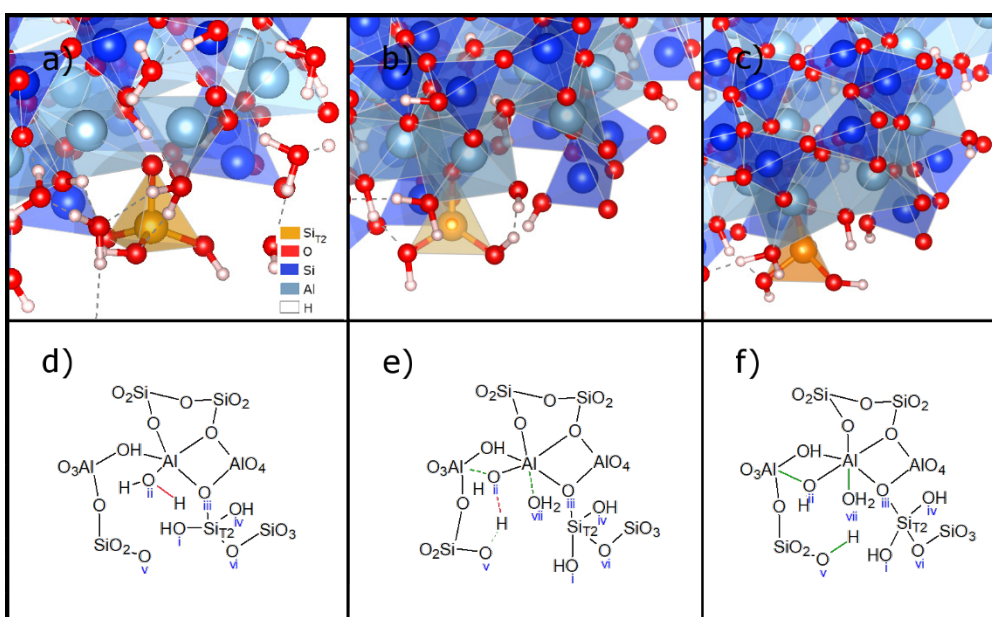
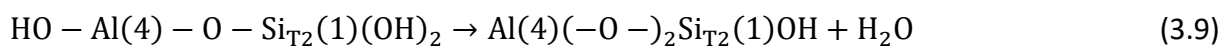


Figure 3.7: Intermediate step of the $\text{Si}_{\text{T}2}$ leaching reaction (see Eq. 3.8). The six-fold coordination of the under-coordinated $\text{Al}(\text{o})$ sites is restored. A water molecule from the slit pore approaches the central $\text{Al}(\text{o})$ site (e). The H_2O group donates a proton to the $\text{O}(\text{v})$ that was attached to $\text{Si}_{\text{T}2}$ in the previous reaction step (Fig. 3.7, Eq. 3.7). The $\text{Al}(\text{o})$ sites regain their CN of 6 (see c and f).

In the next step $\text{Si}_{\text{T}2}$ site forms a second bond to the octahedral sheet and becomes a tri-dentate surface complex (Fig. 3.9). This transformation is accomplished by a proton transfer from the $\text{Si}_{\text{T}2} - \text{O}(\text{iv})\text{H}$ site to the $\text{Al}(4)\text{OH}$ site and the consecutive detachment of H_2O (Eq. 3.9).



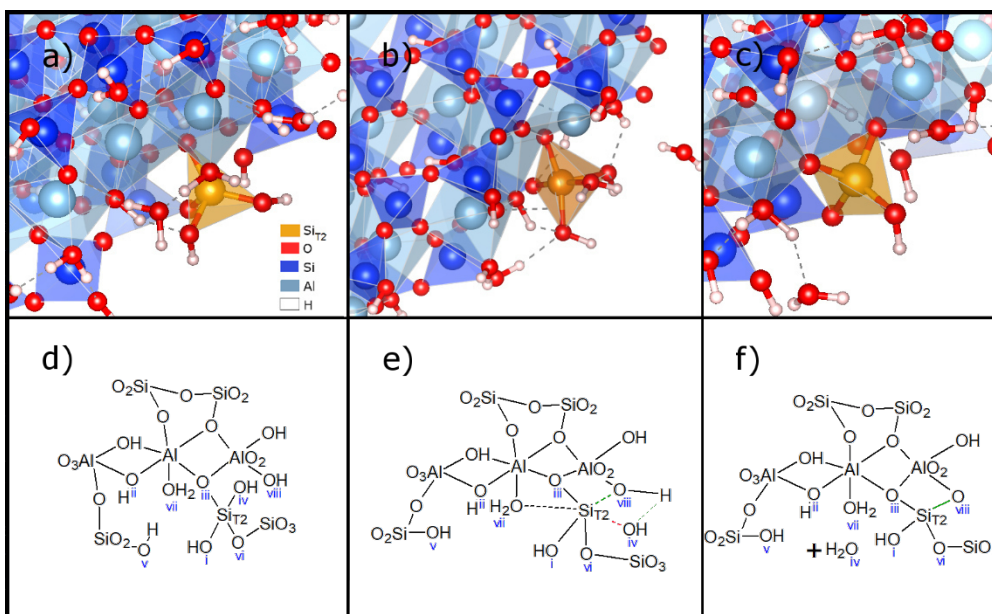


Figure 3.8: Intermediate step of the $\text{Si}_{\text{T}2}$ detachment (see also Eq. 3.9). In this step $\text{Si}_{\text{T}2}$ reattaches to the octahedral sheet to form a tridentate state. The new bond formed by the hydroxyl group bridging two Al(o) sites. The OH group donates the proton to O(iv) and that group detaches as H_2O from the surface. In c) and f) the product with two O_b to the octahedral and one O_b to the tetrahedral sheet is depicted.

In the next reaction step (Fig. 3.10), the oxygen of Al – OH_2 initiate a nucleophilic attack on $\text{Si}_{\text{T}2}$ site, which become an intermediate five-fold coordinated complex. One proton of the H_2O is then transferred to the oxygen bridge between the silicon atoms (O(vi)). The bridging bond breaks and a bidentate $\text{Si}_{\text{T}2}$ complex with two bonds to the octahedral sheet is formed.

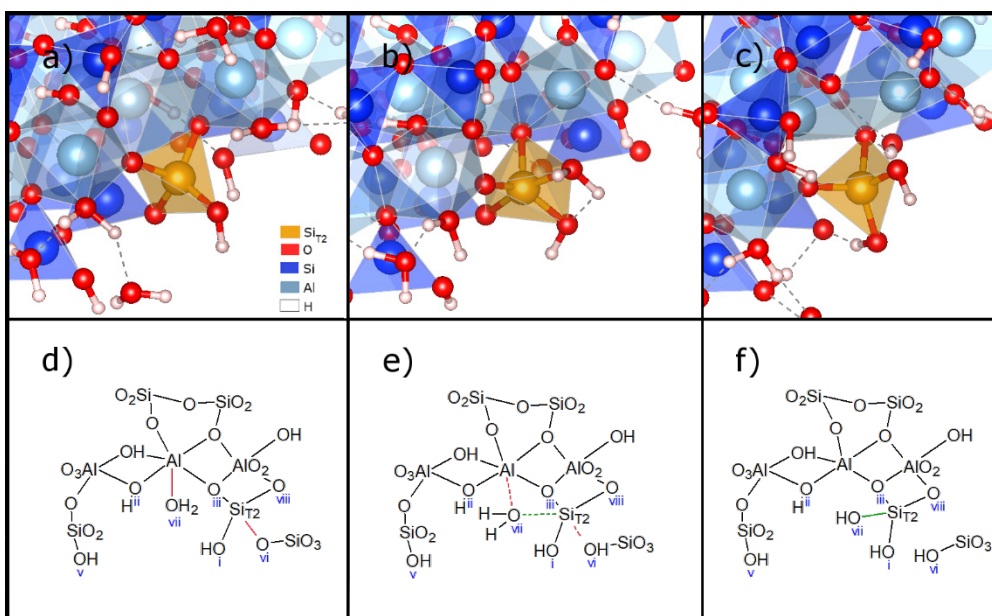
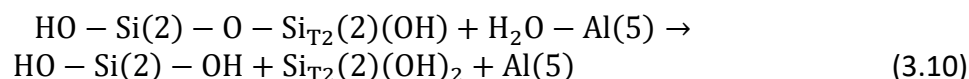


Figure 3.9: Intermediate step of the $\text{Si}_{\text{T}2}$ detachment (see Eq. 3.10). The last O_b bond of the $\text{Si}_{\text{T}2}$ to the T-sheet breaks in this step. The reaction step is mediated through a nucleophilic attack by $\text{O}(\text{vii})\text{H}_2$ on $\text{Si}_{\text{T}2}$ from the neighbouring Al – $\text{O}(\text{vii})\text{H}_2$ group (see a, d and b, e). While the $\text{O}(\text{vii})\text{-Si}_{\text{T}2}$ bond is formed one proton is transferred from $\text{O}(\text{vii})\text{H}_2$ to $\text{O}(\text{vi})$ (see the product state in c and f). The reaction product is a bidentate $\text{Si}_{\text{T}2}$ complex bonded with two O_b to the octahedral sheet.



The neo-formed bi-dentate complex is newly accessible to the interaction with the interfacial water molecules. Consequently, one H₂O molecule attacks on the Si_{T2} site and promotes the formation of a mono-dentate Si_{T2} complex (Fig. 3.11). In the same time, water molecules in

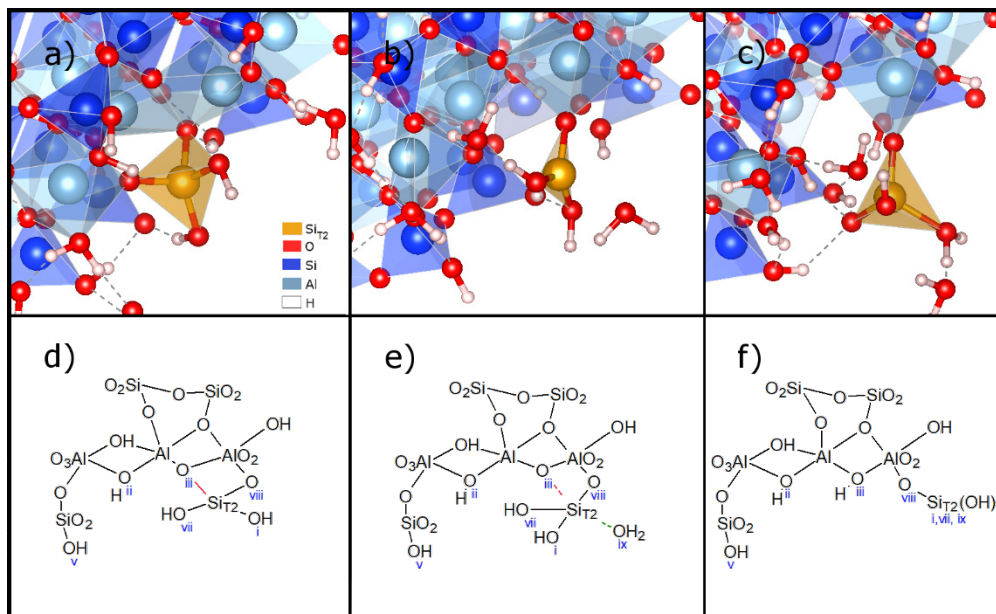


Figure 3.10: Intermediate step of the Si_{T2} detachment (see Eq. 3.11). In this step the bidentate state of Si_{T2} transforms to a monodentate state via a nucleophilic attack of another H₂O molecule from the coordination shell. The bond that breaks is the connection to the octahedral sheet which was stable since the start of the trajectory (O(iii)).

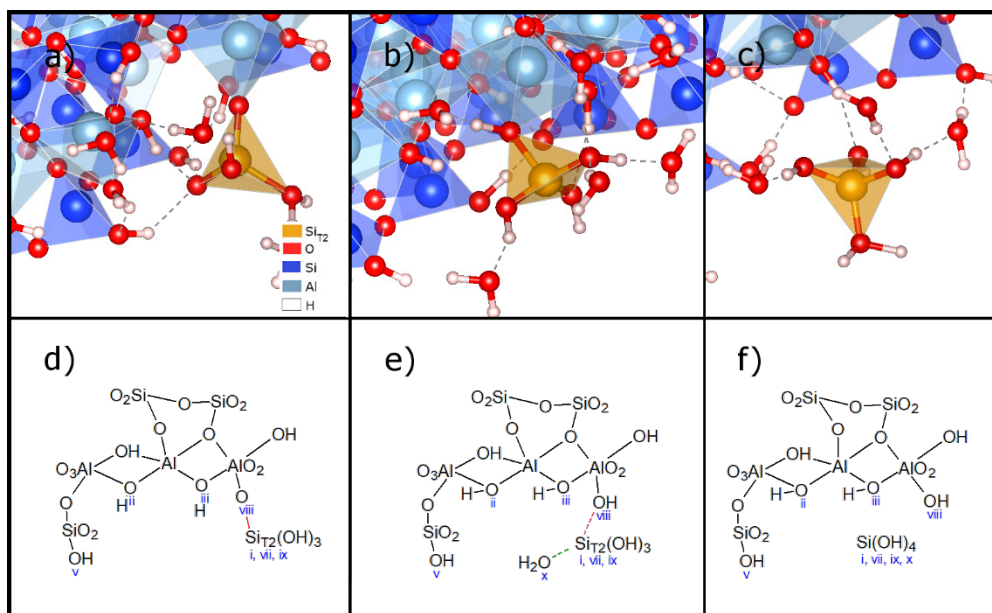
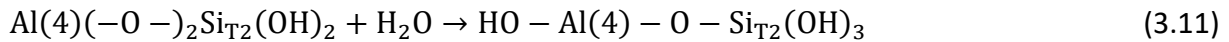
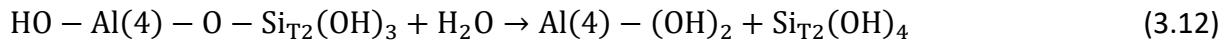


Figure 3.11: Detachment step of the mono-dentate Si_{T2} complex (see Eq. 3.12). Alike the intermediate reaction steps in Fig. 3.8, 3.10 and 3.11 the reaction is triggered by a nucleophilic attack by a H₂O(ix) molecule. Upon the formation of an intermediate five-fold coordinated Si_{T2} complex, the Si_{T2}-O(iii) bond breaks and a proton from H₂O(ix) is transferred to dangling the oxygen site O(iv).

the solvation shell of $\text{Si}_{\text{T}2}$ site rearrange to form a chain of hydrogen bonds enabling the proton transfer from the $\text{Si}_{\text{T}2} - \text{OH}_2$ site to the dangling bond at the edge surface (O(iv)):



The last reaction step, namely the detachment of the mono-dentate complex $\text{Si}_{\text{T}2}(\text{OH})_3$ is again triggered by a nucleophilic attack by a water molecule (Fig. 3.12). The formation of the $\text{Si}_{\text{T}2}(\text{OH})_4$ molecule is mediated by a proton transfer from $\text{Si}_{\text{T}2}\text{O}(\text{ix})\text{H}_2$ to the under-coordinated oxygen site at the octahedral sheet (O(iv)). Eventually, the silicic acid complex is detaching from the surface.



3.3.1.4 Al detachment mechanism

The outermost Al(o) of the (110) edge surface is connected to four Si and two neighbouring Al via bridging oxygen sites O_b . The Al(o) is coordinated with six oxygen atoms including two O_bH and one OH_2 groups. Three O_b sites are threefold coordinated with two Al and one Si, while the fourth O_b is only connected to $\text{Si}_{\text{T}1}$. The hydroxyl group is shared by two neighbouring Al atoms. The hydrogen atoms of OH_2 group are oriented towards the mineral water interface. The notations used in the following section for the reaction equations is analogues to those used for description of Si detachment. Due to the complexity of Al site dynamics, the illustrations of the reaction mechanisms are shown only by schematic diagrams without snapshots from MD simulation.

The first reaction step observed in the Al detachment run is the desorption of a water molecule from six-fold coordinated surface site (see Fig. 3.13; Eq. 3.13).



The re-adsorption of H_2O molecule destabilizes the Al- O_b bonds in the Al coordination shell. The Al-O(ii) and Al-O(iii) bonds elongate and break (see Fig. 3.14). A bidentate complex is formed, which has one bond to $\text{Si}_{\text{T}1}$ site and one bond to the neighbouring octahedral aluminium site. The bidentate Al complex is four coordinated by one H_2O molecule, one OH group and two O_b bridging oxygen sites. The H_2O and OH in the Al coordination shell form HBs to the neighbouring oxygen sites in the octahedral sheet.

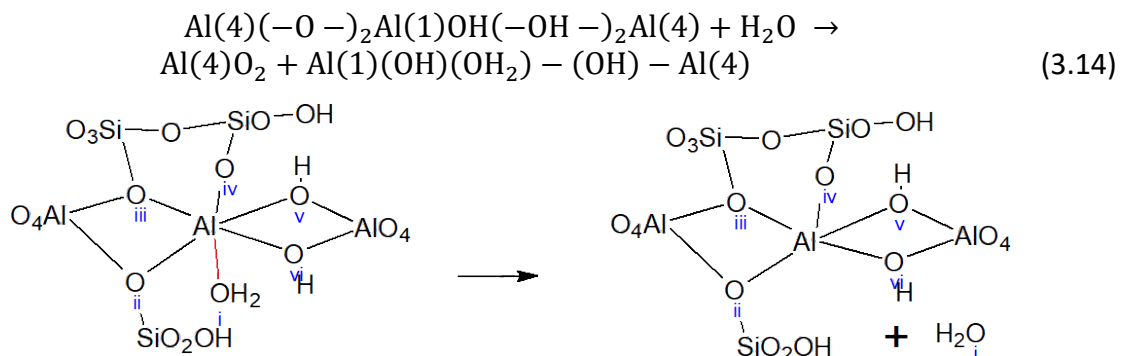


Figure 3.13: First reaction step of Al(o) detachment (Eq. 3.13). In this step, the OH_2 group detaches.

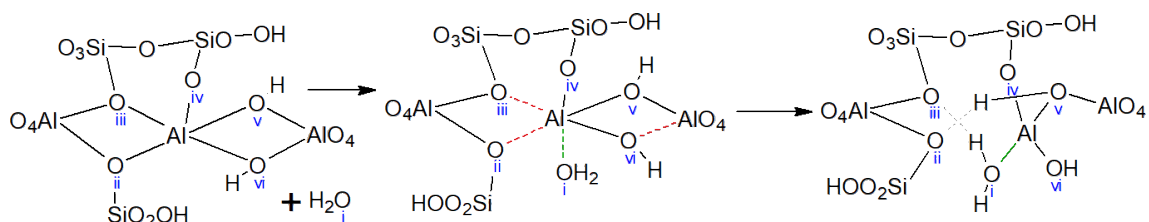


Figure 3.14: Nucleophilic attack of H_2O on the Al(o) site (see Eq. 3.14). The reactant, intermediate state and product of the reaction are shown from left to right. An H_2O enters the coordination shell of Al(o) causing elongation of aluminium-oxygen bonds to O(ii), O(iii) and O(vi) sites. Eventually the Al- O(ii) and Al-O(iii) bonds break, resulting in formation of a bidentate complex. This bidentate reaction intermediate has one bond aluminium-oxygen bond to the tetrahedral sheet and one to the octahedral sheet via O(iv) and O(v) sites, respectively.

In the next step another water molecule enters the coordination shell of the detaching Al(o) and increases the site's CN of from four to five (Eq. 3.15). This bidentate Al(o) complex is thus coordinated with two H_2O , one OH and two O_b (Fig. 3.15).

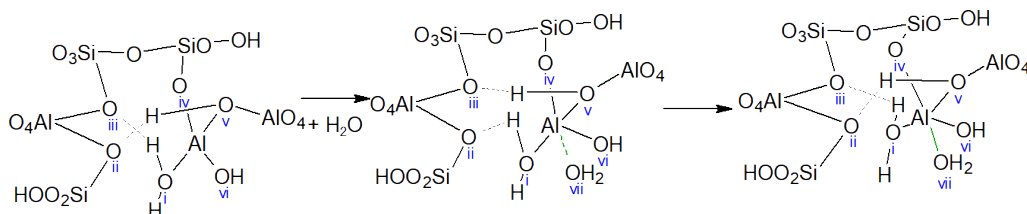
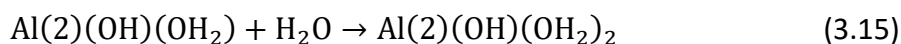
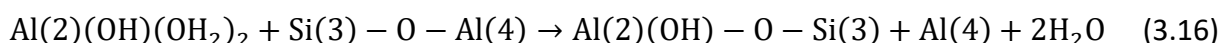


Figure 3.15: A nucleophilic attack of a water molecule on the bi-dentate Al(o) complex. The reaction product consists of a bidentate complex coordinated by two H_2O molecule, one hydroxyl group and two bridging oxygen (O_b) sites (see Eq. 3.15).

In the following reaction step, two water molecules leave the hydration shell of the bidentate Al(o), see Eq. 3.16. The Al complex changes its conformation at the surface and turns into a tri-dentate four-fold coordinated complex with Al- O_b (viii) and Al- O_b (iv) bonds to the tetrahedral sheet and one Al- O_b (v)H bond to the octahedral sheet (Fig. 3.16). The complex is four-fold coordinated with three surface oxygen sites and OH group.



In the next intermediate reaction step, the tri-dentate Al complex undergoes a conformational change on the surface (Fig. 3.17). Initial reactant has two Al- O_b (O(iv) and O(viii)) bonds to the tetrahedral sheet and one Al- O_b (v) bond to the octahedral sheet. The result of the conformational change is another tridentate complex forming one Al- O_b (O(iv)) bonds to the tetrahedral sheet and two Al- O_b bond (O(v) and O(ix)) to the octahedral sheet.

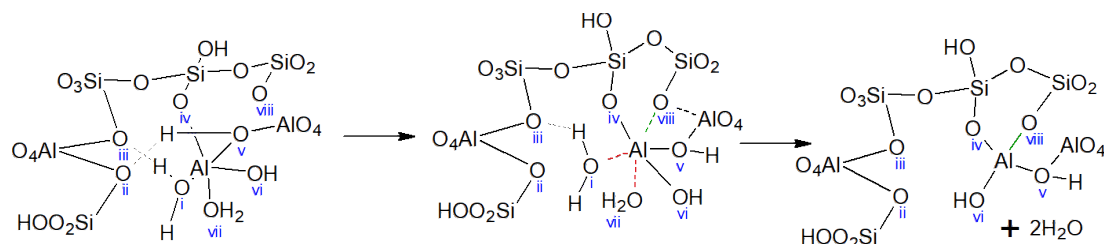


Figure 3.16: Two H_2O molecules leave the coordination of Al(o) site (see Eq. 3.16). The complex transforms from bi-dentate to a tri-dentate configuration.

Both reactant and product remain four-fold coordinated. In the course of the conformational change $O(ix)H_2$ molecule dissociates and the proton is transferred to $O(vi)H$, which becomes an OH_2 group:

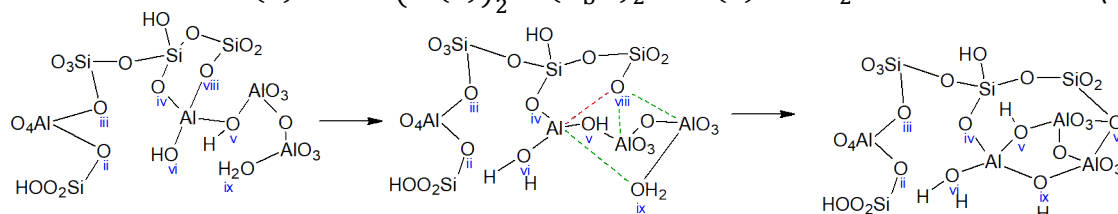
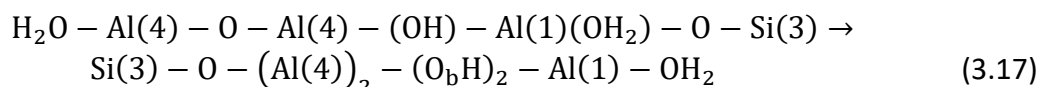


Figure 3.17: Conformational change in the structure of a tridentate Al complex (see Eq. 3.17). Reactant has two $Al-O_b$ ($O(iv)$ and $O(viii)$) bonds to the tetrahedral sheet and one $Al-O_b(v)$ bond to the octahedral sheet. Product forms one $Al-O_b$ ($O(iv)$) bond to the tetrahedral sheet and two $Al-O_b$ bonds ($O(v)$ and $O(ix)$) to the octahedral sheet. Both reactant and product are four-fold coordinated.

The next reaction step is again triggered by a nucleophilic attack of a water molecule on the four-fold coordinated tridentate surface complex (Fig. 3.18). Water enters the hydration shell of the Al complex and cause elongation of $Al-O_b$ bonds in the coordination shell of the five-fold coordinated activated complex.

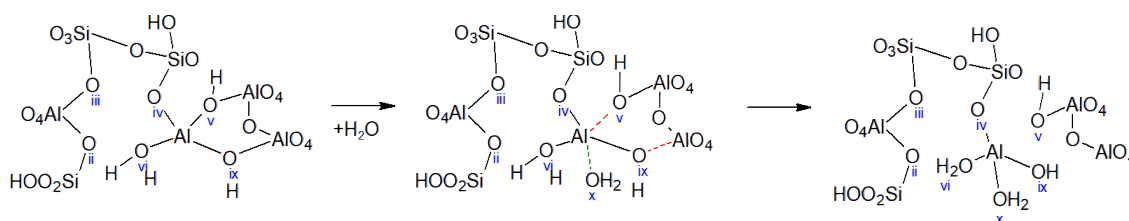
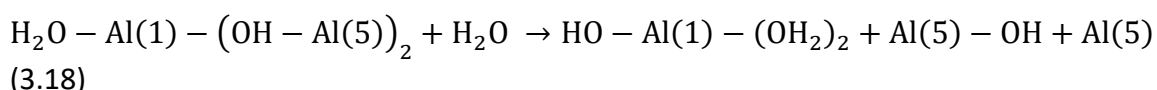


Figure 3.18: Nucleophilic attack of a water molecule on a four-fold coordinated tridentate surface complex (see Eq. 3.18). Water enters the hydration shell of the Al complex and cause elongation of $Al-O_b$ bonds in the coordination shell. The $Al-O_b$ bonds to the octahedral sites result in a mono-dentate four-fold coordinated complex attached to tetrahedral sheet (Si_{T1}) via $O_b(iv)$ oxygen site.

Two $Al-O_b$ bridging bonds to the octahedral sheet breaks resulting in formation of a four-fold coordinated mono-dentate complex attached to tetrahedral sheet (Si_{T1}) via $O_b(iv)$ oxygen site. The coordination shell of this complex consists of a single oxygen bridge to the Si_{T1} site one hydroxyl group and two OH_2 molecules. The OH group and the water molecules forms hydrogen bonds with the surface oxygen sites and support the surface configuration.



Last reaction step is again mediated by a nucleophilic attack of water molecule on the mono-dentate surface complex (Fig. 3.19). A water molecule enters the hydration shell of the complex and causes elongation of $Al-O_b$ bonds in the four-fold coordinated the activated complex. Simultaneously, two water molecules in the coordination shell dissociate and donate protons to the nearby under-coordinated surface oxygen sites. Neo-formed tetrahedrally coordinated aluminiumhydroxide complex $Al(OH)_3OH_2$ is adsorbed at the fluid-surface interface by hydrogen bonds to the surface oxygen sites. Eventually, the $Al(OH)_3OH_2$ complex desorbs from the interface and moves away from the surface.

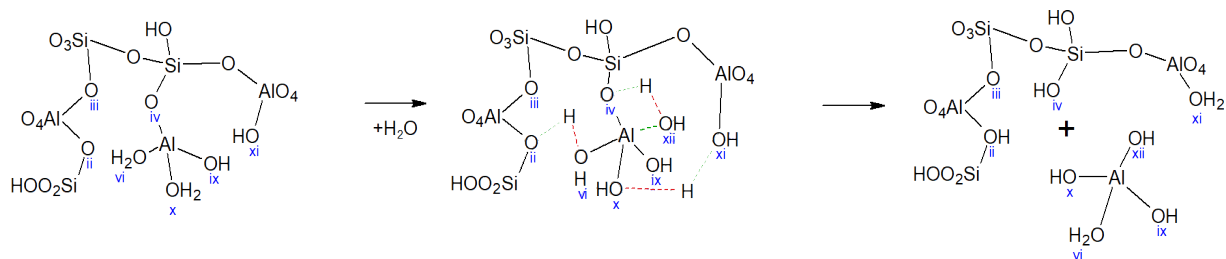
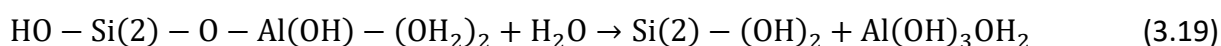


Figure 3.19: Nucleophilic attack of a H_2O on a four-fold coordinated mono-dentate complex surface complex attached to the tetrahedral sheet ($\text{Si}_{\text{T}1}$) via $\text{O}(\text{iv})$ (see Eq. 3.19). Result of the reaction is a four-fold coordinated oxyion $\text{Al}(\text{OH})_3\text{OH}_2$ adsorbed at the mineral water interface via hydrogen bonds.



3.3.2 Activation energies

The free energy data obtained by MetaD simulations are expressed as scalar field in the space of the collective variables (Fig. 3.S1-3.S4 in the Supporting Information). The numerous (local) minima in the free energy surface correspond to initial, final and intermediate states of the multistep dissolution process (e.g. the intermediate reactants and the products). These local minima are connected by a number of saddle points. The saddle points corresponding to the minimum energy path between local minima provide an estimate of the activation energies for the elementary reaction steps. Correspondence between the local energy minima on the FES and actual molecular configurations of the molecular trajectories is obtained based on the analysis of the reaction coordinates. The quantitative analysis of the activation energies for the free energy path between local minima has been conducted using isodensity surface as function of CVs using the visualisation software VisIt (Childs et al., 2012). Estimated activation energies for elementary reaction steps are summarized in Table 3.2. Because of the FES complexity, the full convergence of the FES with respect to the barrier re-crossing cannot be guaranteed within the limited simulation time. Consequently, the energy barrier for the backward reaction cannot be accurately estimated. Therefore, table 3.2 reports values of the forward activation barrier only. In this representation, the relative energy of reactants for each intermediate state are set to $0 \text{ kJ} \cdot \text{mol}^{-1}$.

As discussed in the method section the free energy estimates in MetaD simulations may contain significant bias depending on the choice of collective variables and the system simulation setup.

Table 3.2: Estimated activation energy for elementary reaction steps of Al, and Si dissolution the (110) edge surface of pyrophyllite. The activation energy values are given in $\text{kJ} \cdot \text{mol}^{-1}$.

$\text{Si}_{\text{T}1}$	Equations	3.2 & 3.3	3.4 & 3.5	3.6	
	E_{A}	65.1	112.8	254.0	
$\text{Si}_{\text{T}2}$	Equations	3.7	3.9 & 3.10	3.11	3.12
	E_{A}	204.7	195.3	278.1	8.5
Al	Equations	3.14	3.15 & 3.16	3.17 & 3.18	3.19
	E_{A}	90.4	26.1	69.9	28.5

The Aluminium-octahedra dissolution (see Table 3.2) show four barriers on the FES, which translates into five minima. The silica-tetrahedra detachment takes place via smaller number of reaction steps, typically only three to four barriers. For the Aluminium octahedra

detachment, the activation barriers for each single detachment step does not exceed $100 \text{ kJ} \cdot \text{mol}^{-1}$. The activation barriers for silica detachment are, on average, higher by factor of 2 or even more (see especially $\text{Si}_{\text{T}2}$ in Table 3.2). The highest activation barrier corresponds to the hydrolysis of the last $\text{Si-O}_b\text{-Si}$ bond of a mono-dentate complex (Eq. 3.6 for $\text{Si}_{\text{T}1}$) or one of the $\text{Al-O}_b\text{-Si}$ bonds of a bidentate complex (Eq. 3.11 for $\text{Si}_{\text{T}2}$), respectively.

3.4 Discussion

Investigations of molecular scale dissolution of silicate and alumino-silicate minerals goes back to the pioneering work of (Lasaga and Gibbs, 1990) applying ab initio simulations to small scale cluster models. This modelling and the experimental observations suggest that water should play a key role in the hydrolysis of Si-O-Si and Al-O-Si bonds. Further applications of ab initio modelling have been extended towards the use of more accurate quantum mechanical methods and larger systems to allow a more realistic description of the hydration shell and, where possible, to account for long range solvent effects (Pelmenschikov et al., 2000, 2001; Criscenti et al., 2006; Nangia et al., 2007; Nangia and Garrison, 2008, 2009b, a, 2010a, b; Morrow et al., 2009; Kurganskaya and Lutttge, 2013; Zapol et al., 2013). In general, the recent simulations confirm the original findings that the dissolution of the Si-O-Si and Al-O-Si bonds must proceed via step-by-step hydrolysis of individual bonds assisted by proton transfer reactions from more acidic to more basic oxygen sites. The major limitation of the cluster approach is related to the use of a simplified representation of the surface structure, which may not correctly account for the steric effects at the fluid-surface interface. Furthermore, the geometry optimization approach does not consider the dynamic aspects of the mineral fluid interaction at finite temperature.

The simulations performed in this work include the realistic description of edge surface geometry and takes into account dynamics of the mineral fluid interface. The explicit treatment of the solvent in the system allows for realistic modelling of complex solvent dynamics in the first and the second hydration shell of the reactive surface complexes. To the best of our knowledge, such full-scale ab initio simulations of surface dissolution of phyllosilicate minerals are reported for the first time. A good proxy for the comparison of our results could be the ab initio simulations of crystalline and amorphous silica and aluminosilicate dissolution performed using molecular clusters. Some structural fragments of framework silicates and silica glasses resemble those of pyrophyllite and phyllosilicates in general. (Pelmenschikov et al., 2000, 2001) and (Nangia and Garrison, 2008, 2009a, b) investigated stepwise dissolution of quartz. The dissolution can be represented with a stepwise hydrolysis of bridging oxygen sites from $\text{Si}(\text{O}_b)_4$ to $\text{Si}(\text{OH})_4$. In the bulk structure, Si ions are coordinated by four O_b . Cluster simulations suggest (Pelmenschikov et al., 2000) that for each consequent hydrolysis step the activation energy increases. In the pyrophyllite (110) surface the outmost Si tetrahedra have only two bridging oxygen sites O_b to surface Si and one to surface Al. Thus, the dissolution can be compared with the last two steps of the quartz surface dissolution.

On first glance the reaction pathway obtained in our MetaD simulations seems to be much more complex compared to the one obtained in the static geometry optimizations (Xiao and Lasaga, 1994, 1996; Pelmenchikov et al., 2000, 2001; Criscenti et al., 2006; Nangia and Garrison, 2008, 2009a, b). Part of the apparent complexity is attributed to the more realistic representation of the pyrophyllite edge topography and the explicit consideration of interface molecules applied in this work. A closer look to the MetaD simulation results allows a generalized treatment of the reaction mechanism and a comparison to the static simulations.

The MetaD simulations suggest three most fundamental elementary reaction events leading to the dissolution of silanol and aluminol groups. These elementary reaction steps are the nucleophilic attack of H₂O molecules or OH_x groups on reactive sites, the change of the surface conformation by ligand exchange and the collective hydrogen transfer event from acidic to basic oxygen sites.

At close to neutral pH conditions, as in the current simulation setup, the nucleophilic agents are either water molecules at the interface or, in case of a sterically hindered access for the solvent molecules, the OH/OH₂ groups donated by nearby surface sites (compare Eqs. 3.7, 3.10 and 3.17). It can be further speculated that at higher pH, at which the concentration of OH⁻ in the interface region becomes significant, aqueous OH ion could be a more efficient agent than H₂O. This would be consistent with the known linear increase of the silicate dissolution rate at high pH (Köhler et al., 2003; Kuwahara, 2006b).

The nucleophilic attack and the consequent relaxation of the activated complexes result in significant fluctuation of the coordination shell of the reacting sites. The observed coordination of Si site by oxygen atoms represented by O_b, OH and OH₂ groups was found to vary between 3 and 5. Increase of the coordination number from four to five-fold in the beginning of the nucleophilic attack causes the elongation of Si-O bond and weakening of the interaction to the specific sites. These fluctuations in the first hydration shell allow Si to exchange the bridging oxygen sites O_b with OH groups and eventually leave the surface. Some transition state Si complexes have 3-fold coordination (see Figs. 3.6 b and 3.11 b). This occurs because of the pulling effect applied by the attacking nucleophilic agent (H₂O) that increases the distances between the bridging oxygen connected to the surface. The broken bonds are stabilized by formation of a hydrogen bond to the dangling bridging oxygen site, which typically stay associated with the silica tetrahedra left on the surface.

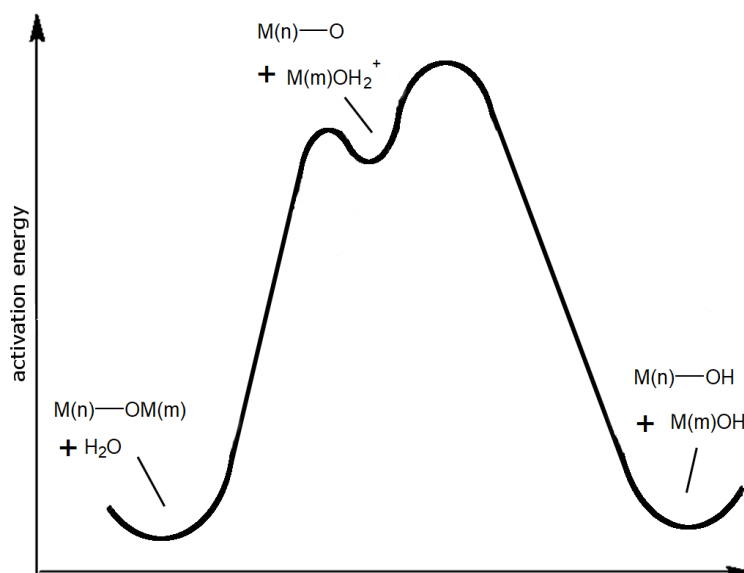
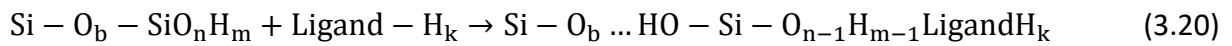


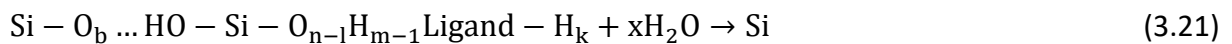
Figure 3.20: Generalized and simplified model for the activation energy profile for a stepwise reduction of the surface site density observed by MetaD simulation. The minimum on the left represents the initial state of the detaching species (M(m)) surrounded by the slit pore water molecules. Overcoming the first barrier leads to one dangling oxygen previously bonded to the surface. The second barrier corresponds to the proton transfer through a chain of HBs, which leads to the minimum on the right. That minimum corresponds to the final state of the detachment mechanism, where the dangling surface oxygen is protonated.

A remarkable difference to the reaction mechanism observed in our simulation and the conceptualizations devised from earlier cluster-based ab initio studies (Xiao and Lasaga, 1994, 1996) is the notice that the nucleophilic agent does not necessarily has steric access to the breaking Si-O bonds at the surface. Such a reaction can be best described as a sort of ligand exchange process, where the increase of the coordination number promotes elongation of the cation-ligand bond distances followed by displacement of the cation towards the nucleophilic agent and the exchange of one surface ligand (see Fig. 3.28). As a result of such ligand exchange the surface is left with one or more highly reactive nucleophilic oxygen sites. Further stabilization of the reaction intermediate takes place by formation of hydrogen bonds towards the nucleophilic oxygen sites, eventually followed by a proton transfer reaction. It is important to note that the OH group donating the hydrogen bond to the dangling $>S-O_b$ site is not the one initiating the nucleophilic attack on the reacting site, but most likely another, nearby, H_2O molecule or possibly an OH_x group present in the coordination shell already before the reaction event. Thus, the coordination shell of the reacting site undergoes complex conformational changes enabling the formation of hydrogen bonds.



The intermediate complex formed in such a reaction event can easily undergo reverse reaction, similar to the self-healing process described by (Pelmenchikov et al., 2001) on the silica surface. For the dissolution process to proceed, the intermediate complex is further stabilized by protonation of the dangling $> Si - O_b$ bond. In the simulations conducted in this work, e.g. at close to neutral pH, the proton is donated by one of the OH_2 groups in the coordination shell of the reacting site. The simulations show that the proton donor site may be spatially separated from the proton acceptor site. Contrary to the reaction mechanism typically modelled in cluster ab initio simulations, the proton transfer between the donor and acceptor sites take place via an intermediate chain of hydrogen bounded molecules, enabling a collective exchange of protons within the chain of hydrogen bonds.

Such collective proton transfer reactions have even been observed in direct ab initio simulations of the pyrophyllite-water interface (Churakov, 2007). This process can be formalized as the consequent reaction:



The first reaction step in the sequence (Eq. 3.20) has the highest activation energy, in the order of $30-200 \text{ kJ} \cdot \text{mol}^{-1}$ and is rate limiting, whereas the second reaction (Eq. 3.21) corresponding to the proton transfer is nearly barrier free. It is important, to note however that the second reaction step is essential for the continuation of the reaction progress. The equilibrium in Eq. 3.20 is strongly shifted to the left and there are high chances for the reversible self-healing reaction unless the reaction 28 takes place. The activation energy for the proton transfer is of entropic nature and depends on the probability of a proper alignment of solvent molecules to enable collective proton transferee event. Under proper consideration of the quantum dynamics of proton the actual collective proton transfer along the chain of hydrogen bond could be nearly barrier free (Tuckerman et al., 1997).

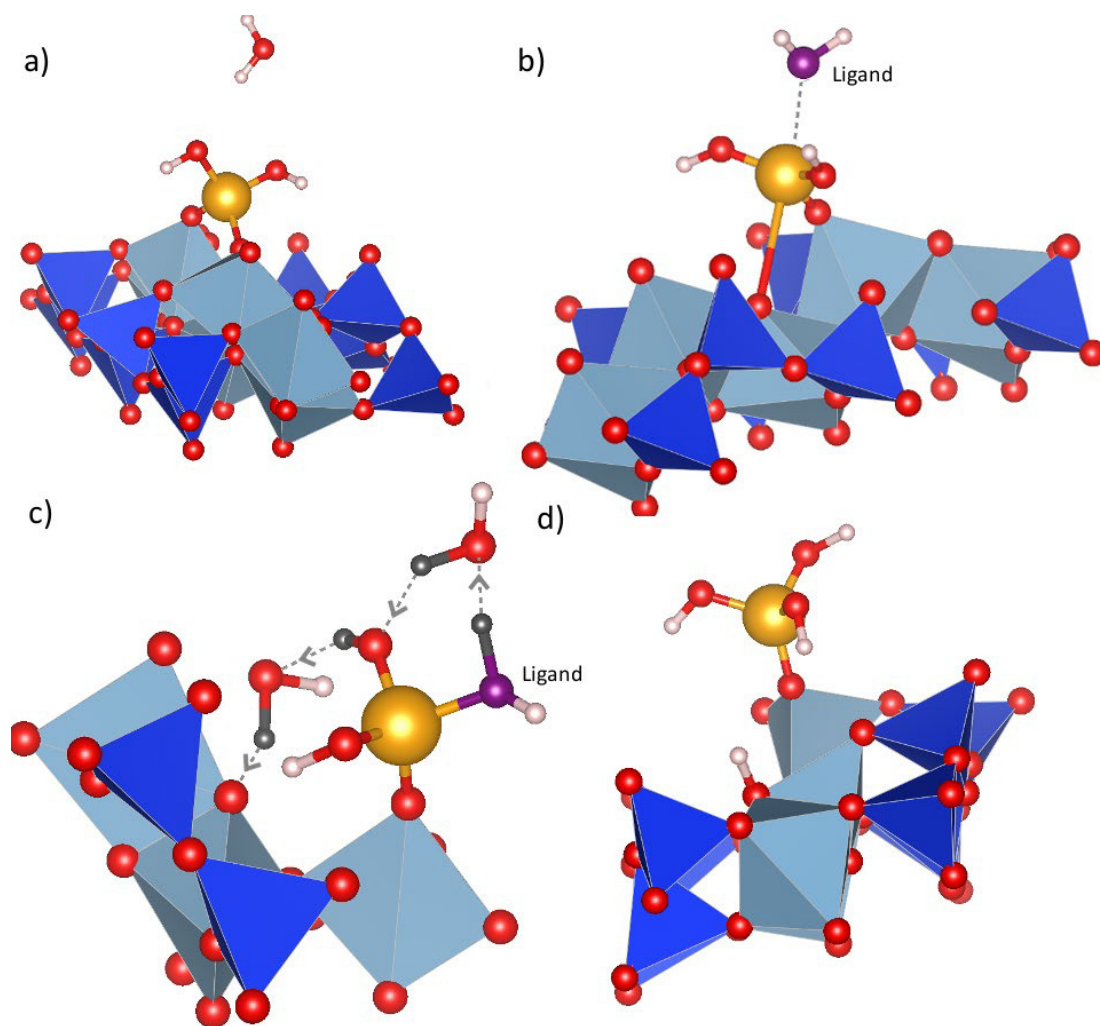


Figure 3.21: Schematic representation of a multistep hydrolysis of a Si-O bond on the edge surface of clay minerals in water. Part of the edge surface is shown using polyhedral representation. Surface Si tetrahedra and Al octahedra are shown as blue and cyan polyhedral respectively. Oxygen atoms are represented by small red spheres. Water molecules not involved in the reaction process are omitted for the sake of simplicity. The initial configuration of reacting Si-tetrahedra (golden sphere) in bidentate configuration is shown in part (a). The first reaction step is the nucleophilic attack of a water molecule (magenta) on a Si bidentate complex, which destabilises the tetrahedral configuration and increases coordination number of Si complex from four to five. Thereafter Si atom moves towards the ligand molecule and loses one Si-O bond to the surface (c). This process is best described as a ligand-exchange (see Eq. 3.20). Stabilisation of the neo-formed complex require protonation of dangling oxygen site on the surface and the rearrangement of OH/H₂O molecules in the Si-hydration shell. The proton donor (that is typically the ligand but could be any other acidic site on the clay mineral surface) donates a proton to the surface site via chain of hydrogen bonds in the first and second coordination shell of the Si complex. The hydrogen bonds are shown by grey dashed lines. The direction of proton transfer along HB is shown by arrows. The net proton transfer is a result of several protons (dark grey) moving simultaneously along the chain of HB. The reaction product is a monodentate surface complex (d, see Eq. 3.21).

In each reaction step associated with the hydrolysis of the bridging $>Si-O_b^{Surf}-(Al,Si)$ bond, the sequence of the reactive steps and the direction of the proton transfer reaction can be rationalized considering the acidity of water and adsorbed OH group on the surface of pyrophyllite. Ab initio studies of the intrinsic surface sites acidity from (Liu et al., 2014; Pfeiffer-Laplaud et al., 2016) suggest that

$$pK_{AlOH}(21.2) > pK_W(14) > pK_{SiOH}(6 \dots 9) > pK_{AlOH_2}(3 - 7) > pK_{SiOH_2}(-5) . \quad (3.22)$$

Thus, the net proton donor of the proton transfer reaction to the dangling $>Si - O_b$ bond at the surface is the $-OH_2$ site participating in the nucleophilic attack to the dissolving site or, with a lower probability, $>Al-OH_2$ sites.

3.4.1 Activation energies

The activation energies for Si dissolution obtained in our study are well comparable with the ones reported before (Pelmenchikov et al., 2000; Criscenti et al., 2005, 2006) for different silicates ($71-167 \text{ kJ} \cdot \text{mol}^{-1}$) and aluminosilicates (Morrow et al., 2009). The calculations in this work predict slightly higher activation energies ($65-280 \text{ kJ/mol}$), which may depend on the specific structural position of the surface groups. Our data also confirm the increase in the activation energies of subsequent reaction steps correlated with the decreasing denticity of the silica species attached to the TOT edge via bridging $-Si-O_b-Si-$ oxygen site (see Table 3.2 for both Si_{T1} and Si_{T2}). The reaction-limiting step for the Si dissolution is thus the hydrolysis of the last mono-dentate bond for both Si_{T1} and Si_{T2} sites (Eqs. 6 and 11, respectively).

Our study suggests that for an ideal (110) surface of pyrophyllite with zero surface charge, the activation energies for the detachment of Al is lower than that of Si. The highest barrier for the detachment of the Al(o) group from the (110) edge surface is lower on average by 20 to $150 \text{ kJ} \cdot \text{mol}^{-1}$ compared to that of the Si(t) group. This means that the octahedral sheet, starting from the Al site with the smallest connectivity to the surface, has a higher possibility of dissolving than either tetrahedral sheets forming the TOT layer of clay minerals. After initial preferential leaching of the octahedral sheet, the outermost Al sites in the octahedral sheet will become sterically inaccessible to water molecules. The initial fast non-stoichiometric leaching of the octahedral sheet will slow down. The dissolution of the phyllosilicate is expected to become congruent and will be controlled by the slower dissolution of the tetrahedral sheets.

Initial fast incongruent dissolution of octahedral cations (e.g. Al) followed by a slow congruent reaction regime has been observed in numerous experimental studies of illite, muscovite and other clay minerals and thus fully consistent with the estimated activation energies and the reaction mechanism obtained in this study (Xiao and Lasaga, 1994; Nagy, 1995; Bauer and Berger, 1998; Köhler et al., 2003; Oelkers et al., 2008; Marty et al., 2011a).

In summary, we would like to emphasize, that the complexity of the FES allows several concurrent dissolution pathways contributing to the overall apparent dissolution reaction kinetics. The details of the reaction mechanism will depend on initial conditions, the surface structure, speciation and the fluid composition. The detachment mechanism of Si_{T1} site (see Figs. 3.2-3.6) is substantially different to the detachment mechanism of Si_{T2} site (Figs. 3.7-3.12). The asymmetry of the (110) surface causes this difference, due to the atoms and bond structure surrounding both sites (see Fig. 3.1). The highest, e.g. rate-limiting activation barriers are comparable for the Si_{T1} and Si_{T2} sites.

3.5 Conclusion

In this study, the *ab initio* MetaD simulations were applied to elucidate the molecular mechanism of pyrophyllite dissolution at the (110) edge surface in pure water at neutral pH under far from equilibrium conditions. Unlike earlier studies, the simulation setup used in this work allows realistic representation of the clay mineral surface and explicit consideration of solvent dynamics at finite temperature. The simulation provides molecular scale reaction mechanism and free energies associated with the individual reaction steps. The simulation reveals that dissolution of a single tetrahedron or octahedron from the clay mineral edge is a complex multistep process with several reaction intermediates. Typically, each reaction step reduces denticity of the reacting site in a step-by-step and eventually lead to release of aqueous aluminol and silanol ions from the surface to the solution. The solvent rearrangement and the proton transfer reactions play a critical role in the stabilization of reaction intermediates and the net progress of the dissolution reactions.

Despite the complexity, a detailed reaction mechanism can be rationalized as a sequence of elementary reaction events, which are:

- 1) the nucleophilic attack of water or OH groups on the dissolving surface site
- 2) ligand exchange reactions in the first coordination shell of the reacting sites leading to its conformational changes and denticity at the mineral surface
- 3) collective proton transfer reaction between the acidic and basic oxygen sites mediated by a chain of the hydrogen bonded molecules in the first and second coordination shell of the reacting site.

Analysis of the activation barriers suggests that dissolution of a pristine surface start with preferential leaching of cations in the octahedral sheet. As the leaching proceeds the access of water to the octahedral sheet cations is sterically hindered and the further dissolution process becomes limited by the dissolution of the tetrahedral sheet and eventually led to an overall congruent dissolution regime.

Although the simulations were conducted at the neutral pH conditions, the mechanism and the factors controlling the dissolution rate at high and low pH conditions can be devised. One of the major reaction-controlling steps observed in the simulation is the nucleophilic attack of a water molecule to the reacting site. Aqueous OH-ion is a stronger nucleophilic agent. Accordingly, the increasing dissolution rate of the phyllosilicate minerals at basic pH can be attributed to the higher concentration of OH, which is a stronger nucleophilic agent. Proton transfer reaction from an acidic to a more basic surface site plays a critical role in the stabilization of the reaction intermediates. The successful proton transfer reactions reduce the probability of the reversible intermediate reactions. The proton transfer reactions are essentially barrier free. The probability of the proton exchange is determined by relative acidity of the donor and acceptor (Liu et al., 2013, 2015b). The activation energy for this reaction step depends on the probability of the specific hydrogen bond arrangement of water molecules enabling the proton transfer reaction. The acidic pH condition increases availability of protons for the saturation of under-coordinated oxygen sites and thus stimulate net dissolution process by reducing the probability of reverse precipitation reactions.

Finally, the experimental studies on mineral dissolution kinetics reveal very similar pH dependence of dissolution rate for various 2:1 and 1:1 phyllosilicates and suggest common reaction control mechanisms for these minerals. Based on these data we argue that the details of the dissolution mechanism obtained on this study for the pyrophyllite should be well applicable to a wide range 2:1 phyllosilicates.

3.6 Supporting Information

System pre-equilibration using classical FF

The equilibration of the system is essential for obtaining accurate structural and thermodynamic data. The ab initio simulations are very expensive. It is therefore important to have good initial guess of atomic coordinates in order to obtain equilibration of the system and to focus on the production ab initio trajectory. For the pre-equilibration of the system, we used classical NVT simulations (constant Volume, Temperature and Number of particles) at 300K for 5 ns using the CLAYFF force field (Cygan et al., 2004b). In these classical MD simulations, the atomic positions of the clay particle were kept frozen according to the results of ab initio structural optimisation. These classical pre-equilibration runs were also used to adjust the box size in b(y)-direction while adjusting the number of water molecules in the system until water-like density in the middle of the water layer was obtained. The density profiles for oxygen atoms in the middle of the water layer was analysed. The obtained molecular configuration was used as initial conditions for actual equilibration of the system by the ab initio simulations.

Collective variables for MetaDynamics simulations

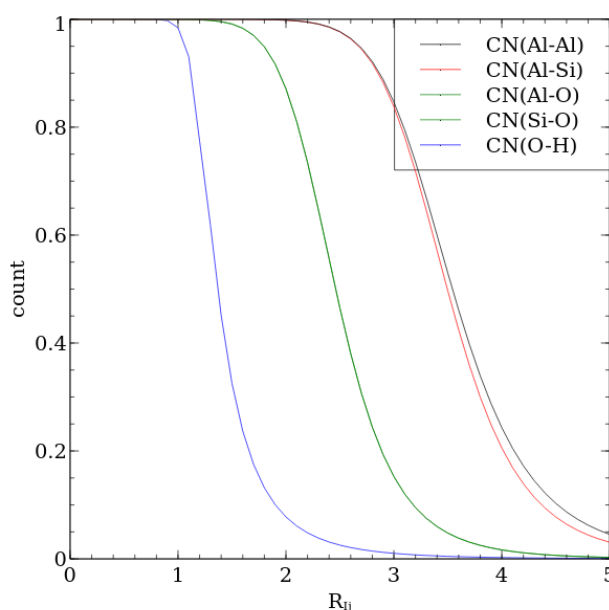


Fig. 3.S1: Graphical representation of the CN functions for all used atom combinations ij . The free energy of the system is described as function of several, system specific reaction coordinates, or more generally speaking the collective variables. One of the main requirements for the collective variable used for the identification of reaction mechanisms is the ability to quantitatively discriminate between the reaction products, reactants, and the reaction intermediates. The collective variable is thus a numerical indicator discriminating the actual state of the system. The nature of the method is such that only those states of the system, which are discriminated by the collective variables, can be sampled. Therefore, the collective variable should be as general as possible and introduce the least possible bias to the system description. Various choices of collective variables (reaction coordinates) are feasible. In this work, we are using coordination numbers of Si and Al atoms with OH and other Al and Si atoms. Si or Al in the solution will be surrounded with OH and H_2O groups whereas at the surface they will be also coordinated by other Si and Al atoms. The mathematical representation of the coordination number is implemented with a smooth step like function

of the interatomic distance, which is close to one when two atoms are coordinating each other and asymptotically go to zero when atoms are apart beyond the coordination distance.

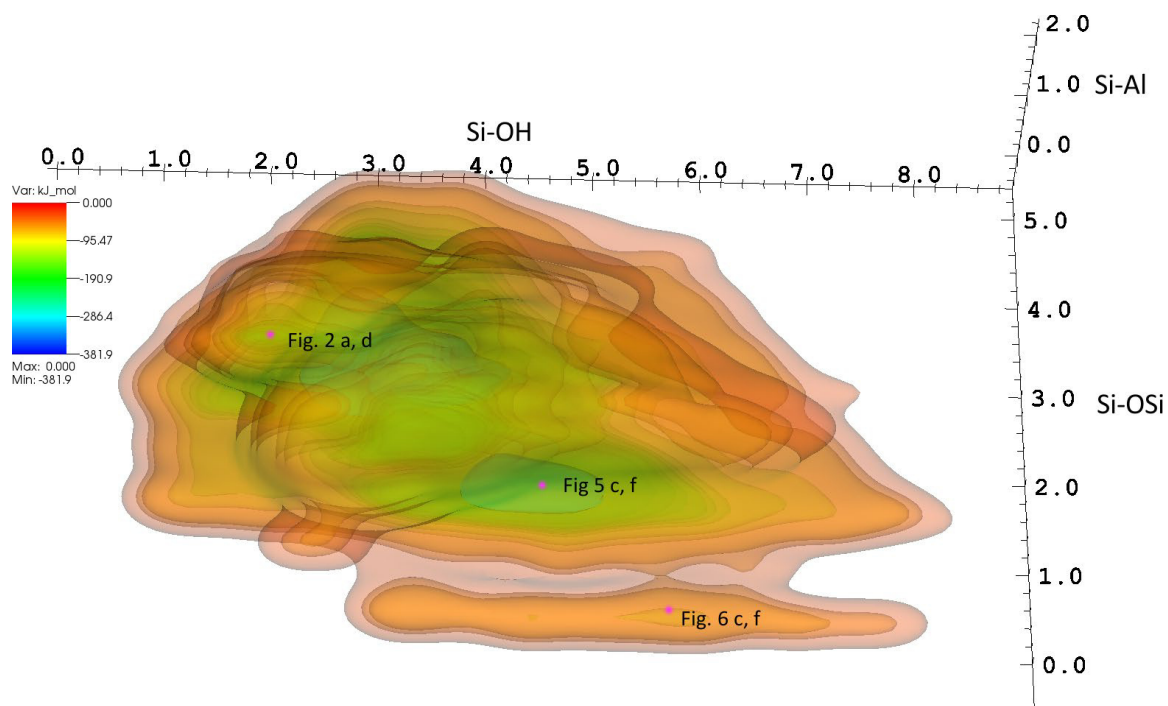


Figure 3.S2: FES of the $\text{Si}_{\text{T}1}$ detachment as obtained by MetaD simulation with a hill size of $7.8 \text{ kJ} \cdot \text{mol}^{-1}$. Three CNs – Si-OH, Si-OSi, Si-Al - (as defined by Eq. 3.1 with the parameters in table 3.1 from the main article) were defined as reaction coordinates. The states that can be clearly distinguished are highlighted with a pink dot and the reference to the corresponding Fig in the main article. The color scale shows the free energy of the shown iso-surfaces in $\text{kJ} \cdot \text{mol}^{-1}$.

Several mathematical representations of the coordination number functions are possible. We are relying on the one used in our previous work (*Churakov et al., 2004*).

The functions used in this study are shown in Fig 3.S9. and Eq. 3.1 in the main paper. The functional parameters R_0 , i and k controls the steepness and the position of the gradual transition between the coordinated (short distance, value close to 1) and uncoordinated (long distance and 0 count). Such distance indicator functions are summed up for all atom of a specific type in the system to give an integral coordination number indicator function. These collective variables are the variables describing the FES in Figs. 3.S2 to 3.S4.

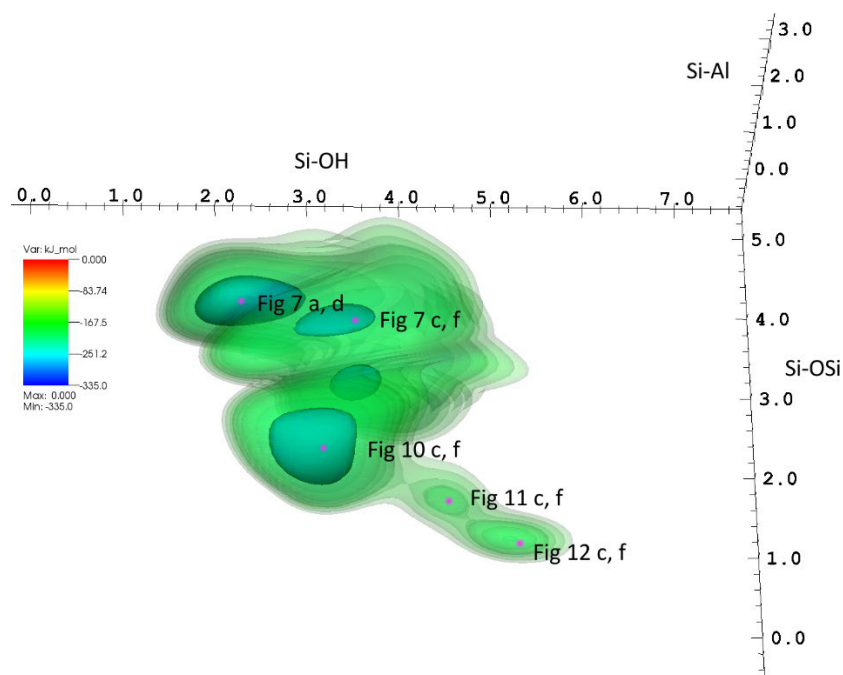


Figure 3.S3: FES of the Si_{T2} detachment as obtained by MetaD simulation. The same three CNs and hill size as in Fig. 3.S2 were used as reaction coordinates. The states that can be clearly distinguished are highlighted with a pink dot and the reference to the corresponding Fig in the main article. The color scale on the right show the free energy of the displayed isosurfaces in $\text{kJ} \cdot \text{mol}^{-1}$.

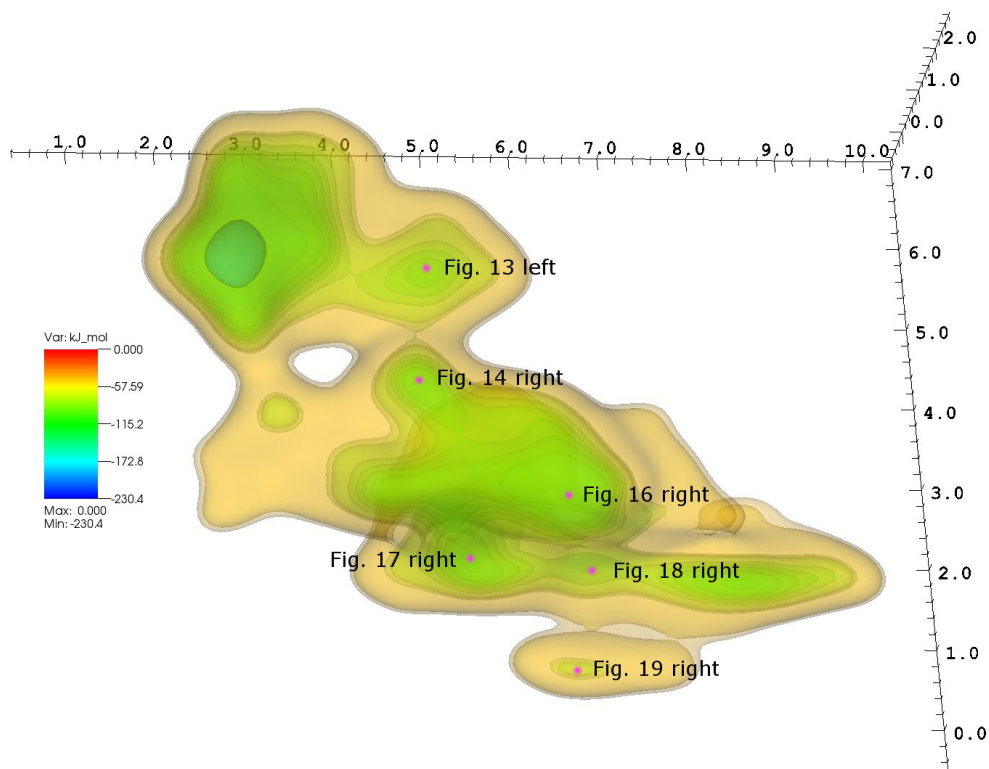


Figure 3.S4: FES of the Al detachment as obtained by MetaD simulation. Three CNs were used to define the reaction coordinates: Al-OH, Al-Al, Al-Si. The states that can be clearly distinguished are highlighted with a pink dot and the reference to the corresponding Fig in the main article. The color scale in the right gives the free energy of the different isosurfaces in $\text{kJ} \cdot \text{mol}^{-1}$.

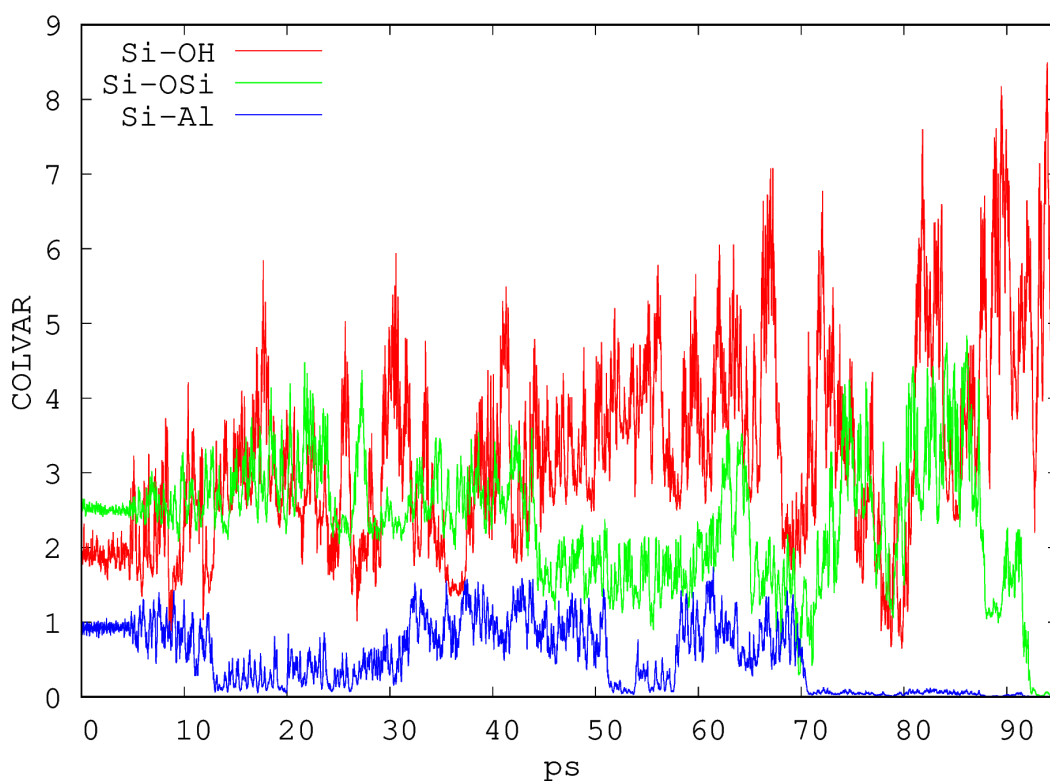


Figure 3.S5: Development of the CNs (or collective variables = COLVAR as defined by Eq. 3.1 in the main article) with time during the $\text{Si}_{\text{T}1}$ detachment as obtained by MetaD simulation.

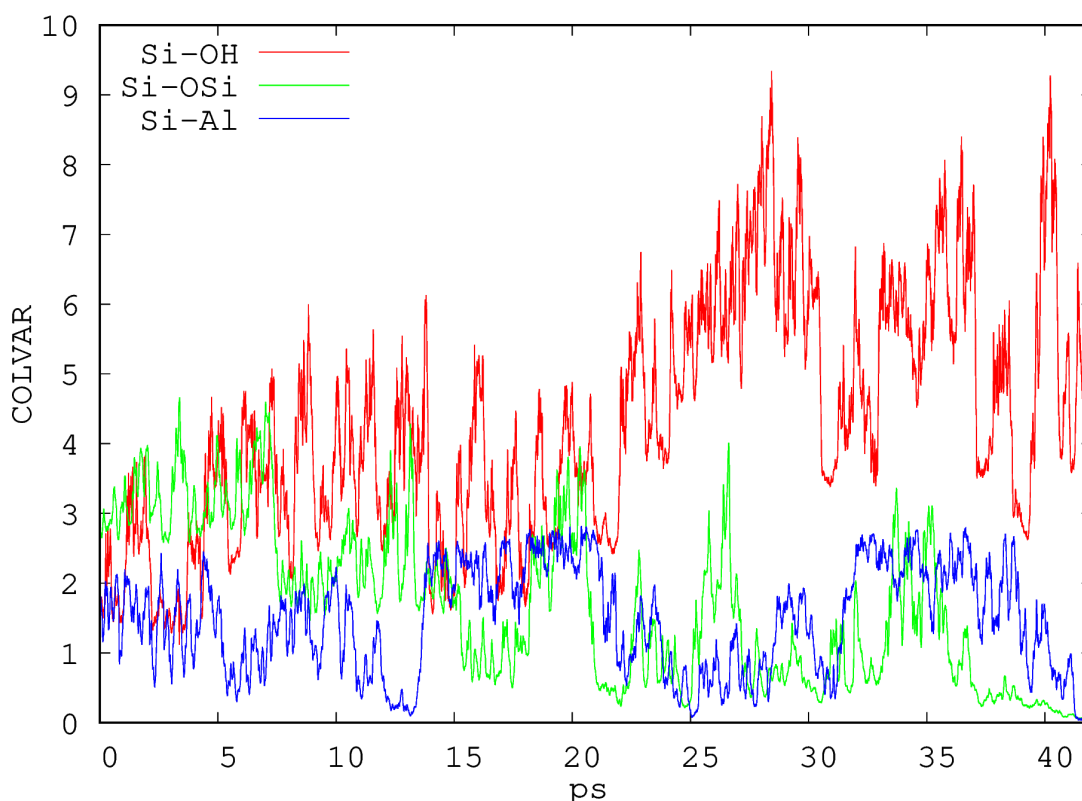


Figure 3.S6: Development of the CNs (or collective variables = COLVAR as defined by Eq. 3.1 in the main article) with time during the $\text{Si}_{\text{T}2}$ detachment as obtained by MetaD simulation.

The time evolution of the CVs is shown in Figs 3.S5 to 3.S7. Since the coordination number defined like this is an integral quantity the individual atoms are indistinguishable, and the system is not biased through the interaction of particular atoms in the system. It is also

important to realise that the exact value of such a collective coordination number is not necessarily corresponding to an integer valued structural definition of coordination.

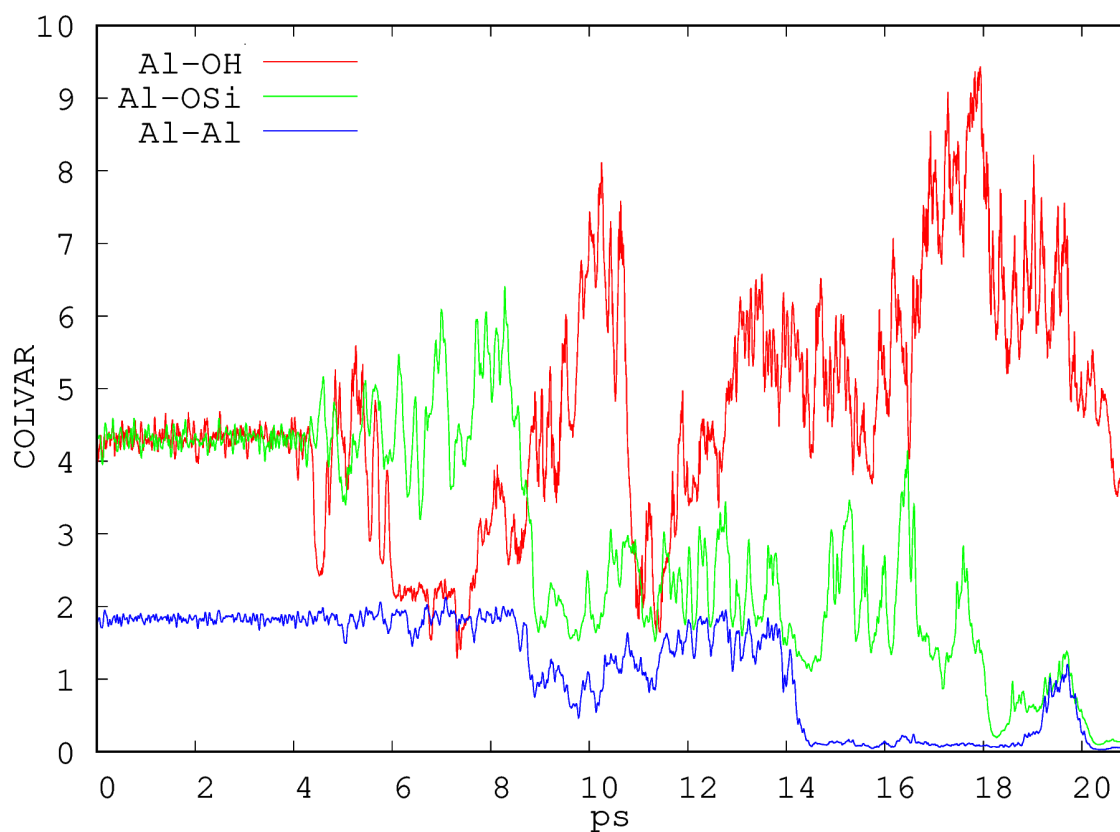


Figure 3.S7: Development of the CNs (or collective variables = COLVAR as defined by Eq. 3.1 in the main article) with time during the Al detachment as obtained by MetaD simulation.

Table 3.S1: Average bond distances (in stable states from the trajectories discussed in the main text. Å) of the

M=	Si ¹						Si ²						Al							
	Fig. reaction step	Fig. 3.2	Fig. 3.2	Fig. 3.3	Fig. 3.4	Fig. 3.5	Fig. 3.6	Fig. 3.7	Fig. 3.7	Fig. 3.9	Fig. 3.10	Fig. 3.11	Fig. 3.12	Fig. 3.13	Fig. 3.13	Fig. 3.14	Fig. 3.15	Fig. 3.16	Fig. 3.17	Fig. 3.18
M-O(i)	3.2	3.2	3.3	3.4	3.5	3.6	3.7	3.7	3.9	3.10	3.11	3.12	3.13	3.13	3.14	3.15	3.16	3.17	3.18	
M-O(ii)	-	1.64	1.66	1.67	1.74	-	-	-	-	-	-	-	1.97	-	-	-	-	-	-	-
M-O(iii)	1.62	-	-	-	-	-	1.65	1.7	1.69	1.65	1.67	-	1.93	-	-	-	-	-	-	-
M-O(iv)	1.66	1.68	1.65	1.6	1.64	1.62	-	1.63	1.63	1.61	1.65	1.69	1.86	1.74	1.83	-	1.81	1.76	-	-
M-O(v)	-	-	-	-	-	-	1.64	-	-	-	-	-	1.9	1.83	1.89	1.89	1.87	-	-	-
M-O(vi)	-	-	-	-	1.66	1.66	1.66	1.64	1.66	-	-	-	1.88	1.77	1.8	1.80	1.88	1.78	1.84	-
M-O(vii)	-	-	-	-	-	1.67	-	-	-	-	1.64	1.68	-	-	1.87	1.99	-	-	-	-
M-O(viii)	-	-	-	-	-	-	-	-	1.64	1.67	-	-	-	-	-	-	-	1.79	1.76	1.82
M-O(ix)	-	-	-	-	-	-	-	-	-	-	-	-	-	-	-	-	-	1.76	1.76	1.82
M-O(x)	-	-	-	-	-	-	-	-	-	-	-	1.69	-	-	-	-	-	-	1.82	1.78
M-O(xii)	1.65	1.59	1.62	1.66	1.65	1.68	-	-	-	-	-	-	-	-	-	-	-	-	-	1.81

3.7 References

- Aldushin K., Jordan G. and Schmahl W. W. (2006) Basal plane reactivity of phyllosilicates studied in situ by hydrothermal atomic force microscopy (HAFM). *Geochimica et Cosmochimica Acta* 70, 4380–4391.
- Altmann S. (2008) `Geo'chemical research: A key building block for nuclear waste disposal safety cases. *Journal of Contaminant Hydrology* 102, 174–179.
- Amram K. and Ganor J. (2005) The combined effect of pH and temperature on smectite dissolution rate under acidic conditions. *Geochim Cosmochim Acta* 69, 2535–2546.
- Baeyens B and Bradbury M. (1997) A mechanistic description of Ni and Zn sorption on Na-montmorillonite .1. Titration and sorption measurements. *Journal of Contaminant Hydrology* 27, 199–222.
- Baeyens Bart and Bradbury M. H. (1997) A mechanistic description of Ni and Zn sorption on Na-montmorillonite Part I: Titration and sorption measurements. *J Contam Hydrol* 27, 199–222.
- Bauer A. and Berger G. (1998) Kaolinite and smectite dissolution rate in high molar KOH solutions at 35° and 80°C. *Appl Geochem* 13, 905–916.
- Bickmore B. R., Bosbach D., Hochella M. F., Charlet L. and Rufe E. (2001) In situ atomic force microscopy study of hectorite and nontronite dissolution: Implications for phyllosilicate edge surface structures and dissolution mechanisms. *Am Mineral* 86, 411–423.
- Bickmore B. R., Rosso K. M., Nagy K. L., Cygan R. T. and Tadanier C. J. (2003) Ab Initio Determination of Edge Surface Structures for Dioctahedral 2:1 Phyllosilicates: Implications for Acid-Base Reactivity. *Clay Clay Miner* 51, 359–371.
- Bosbach D., Charlet L., Bickmore B. and Hochella M. F. (2000) The dissolution of hectorite: In-situ, real-time observations using atomic force microscopy. *Am Mineral* 85, 1209–1216.
- Botan A., Rotenberg B., Marry V., Turq P. and Noetinger B. (2011) Hydrodynamics in Clay Nanopores. *Journal of Physical Chemistry C* 115, 16109–16115.
- Bradbury M. H. and Baeyens B. (2005) Modelling the sorption of Mn(II), Co(II), Ni(II), Zn(II), Cd(II), Eu(III), Am(III), Sn(IV), Th(IV), Np(V) and U(VI) on montmorillonite: Linear free energy relationships and estimates of surface binding constants for some selected heavy metals and actinides. *Geochim Cosmochim Acta* 69, 875–892.
- Bradbury M. H. and Baeyens B. (2011) Predictive sorption modelling of Ni(II), Co(II), Eu(III), Th(IV) and U(VI) on MX-80 bentonite and Opalinus Clay: A ``bottom-up'' approach. *Applied Clay Science* 52, 27–33.
- Bradbury M. H. and Baeyens B. (2009) Sorption modelling on illite Part I: Titration measurements and the sorption of Ni, Co, Eu and Sn. *Geochimica et Cosmochimica Acta* 73, 990–1003.
- Brandt F., Bosbach D., Krawczyk-Bärsch E., Arnold T. and Bernhard G. (2003) Chlorite dissolution in the acid pH-range: a combined microscopic and macroscopic approach. *Geochim Cosmochim Acta* 67, 1451–1461.
- Brantley S. L., White A. F. and Kubicki J. D. (2008) *Kinetics of water-rock interaction.*, Springer New York, United States.

- Brigatti M. F., Galan E. and Theng B. K. G. (2006) Chapter 2 Structures and Mineralogy of Clay Minerals eds. ["Faiza Bergaya and Benny K.G. Theng and Gerhard Lagaly"]. 1, 19–86.
- Bussi G., Donadio D. and Parrinello M. (2007) Canonical sampling through velocity rescaling. *J Chem Phys* 126, 014101.
- Cama J., Ganor J., Ayora C. and Lasaga C. A. (2000) Smectite dissolution kinetics at 80°C and pH 8.8. *Geochim Cosmochim Acta* 64, 2701–2717.
- Childs H., Brugger E., Whitlock B., Meredith J., Ahern S., Pugmire D., Biagas K., Miller M., Harrison C., Weber G. H., Krishnan H., Fogal T., Sanderson A., Garth C., Bethel E. W., Camp D., Rübél O., Durant M., Favre J. M. and Navrátil P. (2012) VisIt: An End-User Tool For Visualizing and Analyzing Very Large Data. , 357–372.
- Churakov S. V. (2006) Ab Initio Study of Sorption on Pyrophyllite: Structure and Acidity of the Edge Sites. *J Phys Chem B* 110, 4135–4146.
- Churakov S. V. (2013) Mobility of Na and Cs on Montmorillonite Surface under Partially Saturated Conditions. *Environmental Science & Technology* 47, 9816–9823.
- Churakov S. V. (2007) Structure and dynamics of the water films confined between edges of pyrophyllite: A first principle study. *Geochimica et Cosmochimica Acta* 71, 1130–1144.
- Churakov S. V. and Dähn R. (2012) Zinc Adsorption on Clays Inferred from Atomistic Simulations and EXAFS Spectroscopy. *Environ Sci Technol* 46, 5713–5719.
- Churakov S. V., Iannuzzi M. and Parrinello M. (2004) Ab Initio Study of Dehydroxylation–Carbonation Reaction on Brucite Surface. *The Journal of Physical Chemistry B* 108, 11567–11574.
- Churakov S. V. and Kosakowski G. (2010) An ab initio molecular dynamics study of hydronium complexation in Na-montmorillonite. *Philosophical Magazine* 90, 2459–2474.
- Churakov S. V. and Liu X. (2018) Quantum-chemical modelling of clay mineral surfaces and clay mineral–surface–adsorbate interactions. *Developments in Clay Science*, 49–87.
- Criscenti L. J., Brantley S. L., Mueller K. T., Tsomaia N. and Kubicki J. D. (2005) Theoretical and ²⁷Al CPMAS NMR investigation of aluminum coordination changes during aluminosilicate dissolution. *Geochimica et Cosmochimica Acta* 69, 2205–2220.
- Criscenti L. J., Kubicki J. D. and Brantley S. L. (2006) Silicate Glass and Mineral Dissolution: Calculated Reaction Paths and Activation Energies for Hydrolysis of a Q3 Si by H₃O⁺ Using Ab Initio Methods. *J Phys Chem* 110, 198–206.
- Cygan R. T., Liang J.-J. and Kalinichev A. G. (2004) Molecular Models of Hydroxide, Oxyhydroxide, and Clay Phases and the Development of a General Force Field. *The Journal of Physical Chemistry B* 108, 1255–1266.
- Dähn R., Scheidegger A., Manceau A., Schlegel M., Baeyens B., Bradbury M. and Chateigner D. (2003) Structural evidence for the sorption of Ni(II) atoms on the edges of montmorillonite clay minerals: A polarized X-ray absorption fine structure study. *Geochimica et Cosmochimica Acta* 67, 1–15.
- Dähn R., Scheidegger A., Manceau A., Schlegel M., Baeyens B., Bradbury M. and Morales M. (2002) Neoformation of Ni phyllosilicate upon Ni uptake on montmorillonite: A kinetics study by powder and polarized extended X-ray absorption fine structure spectroscopy. *Geochimica et Cosmochimica Acta* 66, 2335–2347.

- Delhorme M., Labbez C., Caillet C. and Thomas F. (2010) Acid–Base Properties of 2:1 Clays. I. Modeling the Role of Electrostatics. *Langmuir* 26, 9240–9249.
- Dong H., Kostka J. and Kim J. (2003) Microscopic evidence for microbial dissolution of smectite. *Clays and Clay Minerals* 51, 502–512.
- Duc M., Thomas F. and Gaboriaud F. (2006) Coupled chemical processes at clay/electrolyte interface: A batch titration study of Na-montmorillonites. *Journal of Colloid and Interface Science* 300, 616–625.
- Eypert-Blaison C., Michot L., Humbert B., Pelletier M., Villieras F. and Caillerie J. de la (2002) Hydration water and swelling behavior of magadiite. The H⁺, Na⁺, K⁺, Mg²⁺, and Ca²⁺ exchanged forms. *Journal of Physical Chemistry B* 106, 730–742.
- Fernandes M. M., Vér N. and Baeyens B. (2015) Predicting the uptake of Cs, Co, Ni, Eu, Th and U on argillaceous rocks using sorption models for illite. *Appl Geochem* 59, 189–199.
- Goedecker S., Teter M. and Hutter J. (1996) Separable dual-space Gaussian pseudopotentials. *Physical Review B* 54, 1703–1710.
- Golubev S. V., Bauer A. and Pokrovsky O. S. (2006) Effect of pH and organic ligands on the kinetics of smectite dissolution at 25°C. *Geochim Cosmochim Acta* 70, 4436–4451.
- Grimme S. (2004) Accurate description of van der Waals complexes by density functional theory including empirical corrections. *J Comput Chem* 25, 1463–1473.
- Grimme S., Hansen A., Brandenburg J. G. and Bannwarth C. (2016) Dispersion-Corrected Mean-Field Electronic Structure Methods. *Chemical Reviews* 116, 5105–5154.
- Hartman P. and Perdok W. G. (1955) On the Relations between Structure and Morphology of Crystals .2. *Acta Crystallographica* 8, 521–524.
- Iannuzzi M., Laio A. and Parrinello M. (2003) Efficient Exploration of Reactive Potential Energy Surfaces Using Car-Parrinello Molecular Dynamics. *Phys Rev Lett* 90, 238302.
- Kamp P. C. van de (2008) Smectite-illite-muscovite transformations, quartz dissolution, and silica release in shales. *Clays and Clay Minerals* 56, 66–81.
- Keri A., Dahn R., Krack M. and Churakov S. V. (2019) Characterization of Structural Iron in Smectites - An Ab Initio Based X-ray Absorption Spectroscopy Study. *Environmental Science & Technology* 53, 6877–6886.
- Keri A., Dahn R., Krack M. and Churakov S. V. (2017) Combined XAFS Spectroscopy and Ab Initio Study on the Characterization of Iron Incorporation by Montmorillonite. *Environmental Science & Technology* 51, 10585–10594.
- Köhler S. J., Bosbach D. and Oelkers E. H. (2005) Do clay mineral dissolution rates reach steady state? *Geochim Cosmochim Acta* 69, 1997–2006.
- Köhler S. J., Dufaud F. and Oelkers E. H. (2003) An experimental study of illite dissolution kinetics as a function of pH from 1.4 to 12.4 and temperature from 5 to 50°C. *Geochim Cosmochim Acta* 67, 3583–3594.
- Kremleva A., Martorell B., Krüger S. and Rösch N. (2012) Uranyl adsorption on solvated edge surfaces of pyrophyllite: a DFT model study. *Phys Chem Chem Phys* 14, 5815–5823.
- Kubicki J. D., Sofo J. O., Skelton A. A. and Bandura A. V. (2012) A New Hypothesis for the Dissolution Mechanism of Silicates. *Journal of physical Chemistry C* 116, 17479–17491.

- Kurganskaya I., Arvidson R. S., Fischer C. and Luttge A. (2012) Does the stepwave model predict mica dissolution kinetics? *Geochimica et Cosmochimica Acta* 97, 120–130.
- Kurganskaya I. and Luttge A. (2013) A comprehensive stochastic model of phyllosilicate dissolution: Structure and kinematics of etch pits formed on muscovite basal face. *Geochimica et Cosmochimica Acta* 120, 545–560.
- Kuwahara Y. (2008) In situ observations of muscovite dissolution under alkaline conditions at 25–50 °C by AFM with an air/fluid heater system. *Am Mineral* 93, 1028–1033.
- Kuwahara Y. (2006a) In-situ AFM study of smectite dissolution under alkaline conditions at room temperature. *American Mineralogist* 91, 1142–1149.
- Kuwahara Y. (2006b) In-situ AFM study of smectite dissolution under alkaline conditions at room temperature. *Am Mineral* 91, 1142–1149.
- Kuwahara Y., Uehara S. and Aoki Y. (2001) Atomic Force Microscopy Study of Hydrothermal Illite in Izumiyama Pottery Stone from Arita, Saga Prefecture, Japan. *Clay Clay Miner* 49, 300–309.
- Kuwahara Y., Uehara S. and Aoki Y. (1998) Surface Microtopography of Lath-Shaped Hydrothermal Illite by Tapping-ModeTM and Contact-Mode AFM. *Clay Clay Miner* 46, 574–582.
- Laio A. and Gervasio F. L. (2008) Metadynamics: a method to simulate rare events and reconstruct the free energy in biophysics, chemistry and material science. *Rep Prog Phys* 71, 126601.
- Laio A. and Parrinello M. (2002) Escaping free-energy minima. *Proc National Acad Sci* 99, 12562–12566.
- Laio A., Rodriguez-Fortea A., Gervasio F. L., Ceccarelli M. and Parrinello M. (2005) Assessing the Accuracy of Metadynamics †. *J Phys Chem B* 109, 6714–6721.
- Lasaga A. and Gibbs G. (1990) Ab initio quantum-mechanical calculations of water-rock interactions - Adsorption and hydrolysis reactions. *American Journal of Science* 290, 263–295.
- Liu X., Cheng J., Sprik M., Lu X. and Wang R. (2014) Surface acidity of 2:1-type dioctahedral clay minerals from first principles molecular dynamics simulations. *Geochimica et Cosmochimica Acta* 140, 410–417.
- Liu X., Lu X., Cheng J., Sprik M. and Wang R. (2015a) Temperature dependence of interfacial structures and acidity of clay edge surfaces. *Geochim Cosmochim Ac* 160, 91–99.
- Liu X., Lu X., Cheng J., Sprik M. and Wang R. (2015b) Temperature dependence of interfacial structures and acidity of clay edge surfaces. *Geochimica et Cosmochimica Acta* 160, 91–99.
- Liu X., Lu X., Sprik M., Cheng J., Meijer E. J. and Wang R. (2013) Acidity of edge surface sites of montmorillonite and kaolinite. *Geochimica et Cosmochimica Acta* 117, 180–190.
- Liu X., Lu X., Wang R., Zhou H. and Xu S. (2008) Surface complexes of acetate on edge surfaces of 2:1 type phyllosilicate: Insights from density functional theory calculation. *Geochim Cosmochim Ac* 72, 5896–5907.
- Marty N. C. M., Cama J., Sato T., Chino D., Villieras F., Razafitianamaharavo A., Brendle J., Giffaut E., Soler J. M., Gaucher E. C. and Tournassat C. (2011a) Dissolution kinetics of synthetic Na-smectite. An integrated experimental approach. *Geochimica et Cosmochimica Acta* 75, 5849–5864.

Marty N. C. M., Cama J., Sato T., Chino D., Villieras F., Razafitianamaharavo A., Brendle J., Giffaut E., Soler J. M., Gaucher E. C. and Tournassat C. (2011b) Dissolution kinetics of synthetic Na-smectite. An integrated experimental approach. *Geochimica et Cosmochimica Acta* 75, 5849–5864.

Metz V., Amram K. and Ganor J. (2005a) Stoichiometry of smectite dissolution reaction. *Geochim Cosmochim Acta* 69, 1755–1772.

Metz V., Raanan H., Pieper H., Bosbach D. and Ganor J. (2005b) Towards the establishment of a reliable proxy for the reactive surface area of smectite. *Geochim Cosmochim Acta* 69, 2581–2591.

Molina-Montes E., Donadio D., Hernández-Laguna A., Parrinello M. and Sainz-Díaz C. I. (2013) Water Release from Pyrophyllite during the Dehydroxylation Process Explored by Quantum Mechanical Simulations. *J Phys Chem C* 117, 7526–7532.

Molina-Montes E., Donadio D., Hernández-Laguna A. and Sainz-Díaz C. I. (2010) Exploring the Rehydroxylation Reaction of Pyrophyllite by Ab Initio Molecular Dynamics. *J Phys Chem B* 114, 7593–7601.

Mooney R. W., Keenan A. G. and Wood L. A. (1952) Adsorption of Water Vapor by Montmorillonite. 2. Effect of exchangeable Ions and Lattice Swelling as measured by X-Ray Diffraction. *Journal of the American Chemical Society* 74, 1371–1374.

Morrow C. P., Nangia S. and Garrison B. J. (2009) Ab Initio Investigation of Dissolution Mechanisms in Aluminosilicate Minerals. *J Phys Chem* 113, 1343–1352.

Nagy K. (1995) Dissolution and precipitation kinetics of sheet silicates eds. ["White, AF and Brantley, and SL"]. 31, 173–233.

Nangia S. and Garrison B. J. (2009a) Ab initio study of dissolution and precipitation reactions from the edge, kink, and terrace sites of quartz as a function of pH. *Mol Phys* 107, 831–843.

Nangia S. and Garrison B. J. (2009b) Advanced Monte Carlo Approach To Study Evolution of Quartz Surface during the Dissolution Process. *Journal of the American Chemical Society* 131, 9538–9546.

Nangia S. and Garrison B. J. (2008) Reaction Rates and Dissolution Mechanisms of Quartz as a Function of pH †. *J Phys Chem* 112, 2027–2033.

Nangia S. and Garrison B. J. (2010a) Role of Intrasurface Hydrogen Bonding on Silica Dissolution. *J Phys Chem C* 114, 2267–2272.

Nangia S. and Garrison B. J. (2010b) Theoretical advances in the dissolution studies of mineral–water interfaces. *Theor Chem Acc* 127, 271–284.

Nangia S., Washton N. M., Mueller K. T., Kubicki J. D. and Garrison B. J. (2007) Study of a Family of 40 Hydroxylated β -Cristobalite Surfaces Using Empirical Potential Energy Functions. *J Phys Chem C* 111, 5169–5177.

Oelkers E. H., Schott J., Gauthier J.-M. and Herrero-Roncal T. (2008) An experimental study of the dissolution mechanism and rates of muscovite. *Geochimica et Cosmochimica Acta* 72, 4948–4961.

Paineau E., Bihannic I., Baravian C., Philippe A.-M., Davidson P., Levitz P., Funari S. S., Rochas C. and Michot L. J. (2011a) Aqueous Suspensions of Natural Swelling Clay Minerals. 1. Structure and Electrostatic Interactions. *Langmuir* 27, 5562–5573.

- Paineau E., Michot L. J., Bihannic I. and Baravian C. (2011b) Aqueous Suspensions of Natural Swelling Clay Minerals. 2. Rheological Characterization. *Langmuir* 27, 7806–7819.
- Pelmenschikov A., Leszczynski J. and Pettersson L. G. M. (2001) Mechanism of Dissolution of Neutral Silica Surfaces: Including Effect of Self-Healing. *J Phys Chem* 105, 9528–9532.
- Pelmenschikov A., Strandh H., Pettersson L. G. M. and Leszczynski J. (2000) Lattice Resistance to Hydrolysis of Si–O–Si Bonds of Silicate Minerals: Ab Initio Calculations of a Single Water Attack onto the (001) and (111) β -Cristobalite Surfaces. *J Phys Chem B* 104, 5779–5783.
- Perdew J. P., Burke K. and Ernzerhof M. (1996) Generalized Gradient Approximation Made Simple. *Phys Rev Lett* 77, 3865–3868.
- Pfeiffer-Laplaud M., Gageot M.-P. and Sulpizi M. (2016) pK(a) at Quartz/Electrolyte Interfaces. *Journal of Physical Chemistry Letters* 7, 3229–3234.
- Ponnamperuma C., Shimoyama A. and Friebele E. (1982) Clay and the Origin of Life. *Origins of Life and Evolution of the Biosphere* 12, 9–40.
- Robin V., Tertre E., Regnault O. and Descostes M. (2016) Dissolution of beidellite in acidic solutions: Ion exchange reactions and effect of crystal chemistry on smectite reactivity. *Geochim Cosmochim Acta* 180, 97–108.
- Rotenberg B., Morel J.-P., Marry V., Turq P. and Morel-Desrosiers N. (2009) On the driving force of cation exchange in clays: Insights from combined microcalorimetry experiments and molecular simulation. *Geochimica et Cosmochimica Acta* 73, 4034–4044.
- Salles F., Douillard J.-M., Denoyel R., Bildstein O., Jullien M., Beurroies I. and Damme H. V. (2009) Hydration sequence of swelling clays: Evolutions of specific surface area and hydration energy. *J Colloid Interf Sci* 333, 510–522.
- Schlegel M. L. and Manceau A. (2006) Evidence for the nucleation and epitaxial growth of Zn phyllosilicate on montmorillonite. *Geochim Cosmochim Acta* 70, 901–917.
- Smith D. E., Wang Y., Chaturvedi A. and Whitley H. D. (2006) Molecular simulations of the pressure, temperature, and chemical potential dependencies of clay swelling. *Journal of Physical Chemistry B* 110, 20046–20054.
- Snowdeniff D., Price P. B., Nagahara L. A. and Fujishima A. (1993) Atomic-Force-Microscopic observations of dissolution of mica at sites penetrated by keV/nucleon ions. *Physical Review Letters* 70, 2348–2351.
- Soltermann D., Baeyens B., Bradbury M. H. and Fernandes M. M. (2014a) Fe(II) Uptake on Natural Montmorillonites. II. Surface Complexation Modeling. *Environmental Science & Technology* 48, 8698–8705.
- Soltermann D., Fernandes M. M., Baeyens B., Daehn R., Joshi P. A., Scheinost A. C. and Gorski C. A. (2014b) Fe(II) Uptake on Natural Montmorillonites. I. Macroscopic and Spectroscopic Characterization. *Environmental Science & Technology* 48, 8688–8697.
- Szczerba M., Kalinichev A. G. and Kowalik M. (2020) Intrinsic hydrophobicity of smectite basal surfaces quantitatively probed by molecular dynamics simulations. *Applied Clay Science* 188.
- Tournassat C., Grangeon S., Leroy P. and Giffaut E. (2013) Modeling specific pH dependent sorption of divalent metals on montmorillonite surfaces. A review of pitfalls, recent achievements and current challenges. *American Journal of Science* 313, 395–451.

- Tournassat C., Neaman A., Villiéras F., Bosbach D. and Charlet L. (2003) Nanomorphology of montmorillonite particles: Estimation of the clay edge sorption site density by low-pressure gas adsorption and AFM observations. *Am Mineral* 88, 1989–1995.
- Tuckerman M. E., Marx D., Klein M. L. and Parrinello M. (1997) On the Quantum Nature of the Shared Proton in Hydrogen Bonds. *Science* 275, 817–820.
- Tunega D., Bučko T. and Zaoui A. (2012) Assessment of ten DFT methods in predicting structures of sheet silicates: Importance of dispersion corrections. *J Chem Phys* 137, 114105.
- Turpault M. P. and Trotignon L. (1994) The dissolution of biotite single-crystals in dilute HNO₃ at 24-degrees-C - Evidence of an anisotropic corrosion process of micas in acidic solutions. *Geochimica et Cosmochimica Acta* 58, 2761–2775.
- VandeVondele J. and Hutter J. (2007) Gaussian basis sets for accurate calculations on molecular systems in gas and condensed phases. *J Chem Phys* 127, 114105.
- VandeVondele J., Krack M., Mohamed F., Parrinello M., Chassaing T. and Hutter J. (2005) Quickstep: Fast and accurate density functional calculations using a mixed Gaussian and plane waves approach. *Comput Phys Commun* 167, 103–128.
- Voinot A., Lemarchand D., Collignon C., Granet M., Chabaux F. and Turpault M.-P. (2013a) Experimental dissolution vs. transformation of micas under acidic soil conditions: Clues from boron isotopes. *Geochim Cosmochim Acta* 117, 144–160.
- Voinot A., Lemarchand D., Collignon C., Granet M., Chabaux F. and Turpault M.-P. (2013b) Experimental dissolution vs. transformation of micas under acidic soil conditions: Clues from boron isotopes. *Geochimica et Cosmochimica Acta* 117, 144–160.
- Walther J. (1996) Relation between rates of aluminosilicate mineral dissolution, pH, temperature, and surface charge. *American Journal of Science* 296, 693–728.
- Wang J., Kalinichev A. G., Kirkpatrick R. J. and Cygan R. T. (2005) Structure, Energetics, and Dynamics of Water Adsorbed on the Muscovite (001) Surface: A Molecular Dynamics Simulation. *J Phys Chem B* 109, 15893–15905.
- White G. N. and Zelazny L. W. (1988) Analysis and Implications of the Edge Structure of Dioctahedral Phyllosilicates. *Clay Clay Miner* 36, 141–146.
- Whitley H. and Smith D. (2004) Free energy, energy, and entropy of swelling in Cs-, Na-, and Sr-montmorillonite clays. *Journal of Chemical Physics* 120, 5387–5395.
- Wick S., Baeyens B., Fernandes M. M. and Voegelin A. (2018) Thallium Adsorption onto Illite. *Environmental Science & Technology* 52, 571–580.
- Xiao Y. and Lasaga A. (1996) Ab initio quantum mechanical studies of the kinetics and mechanisms of quartz dissolution: OH⁻ catalysis. *Geochimica et Cosmochimica Acta* 60, 2283–2295.
- Xiao Y. and Lasaga A. C. (1994) Ab initio quantum mechanical studies of the kinetics and mechanisms of silicate dissolution: H⁺(H₃O⁺) catalysis. *Geochim Cosmochim Acta* 58, 5379–5400.
- Zapol P., He H., Kwon K. D. and Criscenti L. J. (2013) First-Principles Study of Hydrolysis Reaction Barriers in a Sodium Borosilicate Glass. *Int J Appl Glass Sci* 4, 395–407.

Zhang C., Liu X., Lu X. and He M. (2018) Complexation of heavy metal cations on clay edges at elevated temperatures. *Chem Geol* 479, 36–46.

Zhang C., Liu X., Lu X., He M., Meijer E. J. and Wang R. (2017) Surface complexation of heavy metal cations on clay edges: insights from first principles molecular dynamics simulation of Ni(II). *Geochimica et Cosmochimica Acta* 203, 54–68.

4. Dissolution mechanism of Pyrophyllite under metamorphic pressure conditions

The text of this chapter is published as René Schliemann & Sergey V. Churakov “Pyrophyllite dissolution at elevated pressure conditions: An ab initio study” *Geochimica et Cosmochimica Acta* 307, 42–55.

Abstract

The atomistic mechanism of dissolution reactions at mineral fluid interface is essential for understanding the reaction kinetics and the adsorption and thermodynamic equilibria at mineral surfaces. In this study we investigate the initial state of the dissolution process on (010) surface of pyrophyllite by applying large-scale ab initio Meta-Dynamics simulations. The system setup provides a realistic representation of the clay mineral edge surface structure and takes into account explicit dynamics of solvent molecules. The model parameters follow the procedure recently tested for the simulation of the (110) pyrophyllite edge. The simulation reveals that dissolution of a single tetrahedral or an octahedral unit from the clay mineral edge is a complex multi-step process with several reaction intermediates. Typically, each reaction step changes the denticity of the reacting site in a step-by-step manner and leads, eventually, to the leaching of the ions forming the octahedral and tetrahedral sheets of the phyllosilicate. The solvent rearrangement and the proton transfer reactions in the first and second coordination shell of the dissolving unit play a critical role in the stabilization of reaction intermediates and the net progress of the dissolution reactions. The simulation reveals new insight into the coordination environment of the dissolving complexes at the mineral fluid interface.

4.1 Introduction

Clay minerals, phyllosilicates, are one of the main components of soils and sedimentary rocks formed by the processes of chemical weathering (Grim and Company, 1968). In natural environment, the clayish sediments and soil often act as a hydraulic barrier with low hydraulic conductivity (Pusch, 2006). One of the remarkable properties of clay minerals is their exceptionally high cation exchange capacity (Slabaugh, 1954; Kahr and Madsen, 1995; Bergaya and Vayer, 1997; Meier and Kahr, 1999; Dohrmann et al., 2012a, b) and the minute size of crystallites. Their high specific surface (Tournassat et al., 2003; Metz et al., 2005; Czurda, 2006; Macht et al., 2011) and sorption selectivity towards transition metals explain their use as effective adsorbent of hazardous metals. At large scale clayish materials are applied as natural and engineered low permeability barrier to confine pollutant transport in natural environment (Czurda, 2006; Dohrmann et al., 2013; Kaufhold et al., 2013).

The crystal structure of 2:1 phyllosilicates can be described as a sheet of octahedrally (O) coordinated cations sandwiched between two sheets of silica tetrahedra (T), forming a TOT layer. Isomorphic substitutions of lattice cations by cations of a lower valence in the T and O sheets, result in permanent negative structural charge in the TOT layer (Meunier, 2005). This charge is compensated by positively charged cationic species located in between the TOT platelets (interlayer cations) or forming a diffuse double layer normal to the tetrahedral sheet

(basal plane). The electrostatically bound cations, which constitute the electrical double layer, can undergo stoichiometric exchange with the cations in solution. Most of the clay sorption capacity is related to the cation exchange processes at the basal plane. The cation exchange process is chemically unspecific and essentially controlled by the magnitude of the cation charge and the effective ionic size (Bourg et al., 2003; Bourg et al., 2007; Tournassat et al., 2013). Compared to the basal plane, the edges of the clay particles are highly reactive. The surface speciation of edge faces of a clay particle depends on pH and the ionic strength of the solution (Churakov and Liu, 2018; Delhorme et al., 2010). The thermochemistry and the protonation mechanism of the edge has been intensively investigated by *ab initio* simulations (Liu et al., 2014a; Liu et al., 2015; Liu et al., 2013; Liu et al., 2014b). It has been also shown that the (110) and (010) are two of the most stable edge surfaces of 2:1 phyllosilicate particles (Churakov, 2006, 2007; Keri et al., 2020; Kraevsky et al., 2020).

The edges of clay minerals are known to have a high selectivity with respect to transition metals, lanthanides and actinides (Baeyens and Fernandes, 2018). The specific adsorption mechanism of cations on edges of phyllosilicates has been studied with wet chemical experiments, spectroscopic investigation and atomistic modelling (Dähn et al., 2011; Dähn et al., 2002; Dähn et al., 2003; Dähn et al., 2002a; Manceau et al., 2004; Marques Fernandes et al., 2012; Schlegel and Manceau, 2006; Soltermann et al., 2013; Soltermann et al., 2014; Tournassat et al., 2016; Tournassat et al., 2018). One of the most successful thermodynamic sorption models for the uptake of cations on edge sites, 2SPSC/CE (Baeyens and Bradbury, 1997; Bradbury and Baeyens, 2005; Bradbury and Baeyens, 2011; Marques Fernandes et al., 2015; Wick et al., 2018), assumes existence of high and low affinity sites with lower and higher site density (~ 40 and $\sim 2 \text{ mmol kg}^{-1}$), respectively. The nature of these sorption sites has been recently revealed by combining XAS studies and molecular simulations (Churakov and Dähn, 2012; Dähn et al., 2003; Keri et al., 2020). It could be shown that for divalent and trivalent transition metals, the low affinity sites correspond to inner-sphere surface complexes. The high affinity surface sites can be viewed as ions incorporation into structural defects corresponding to the single atom etch pits in the octahedral layer of clay minerals. The uptake of cations on the strong sites has been shown to be often irreversible. The release and uptake of the metal cations on the strong sorption sites is related to the dissolution-precipitation process (Dähn et al., 2003; Schlegel and Manceau, 2006; Schlegel et al., 2001). Recently, molecular scale mechanism of the edge surface reactivity has been successfully incorporated into thermodynamic sorption model (Zhang et al., 2018).

The kinetic based description of the 2:1 phyllosilicate dissolution is essential for reactive transport simulations of the chemical weathering and low temperature diagenic process or geochemical interaction geotechnical barriers (Marty, 2009; Gaucher, 2006). The dissolution rate and the solubility of clay minerals is strongly controlled by pH. The solubility and the dissolution rates have V-shape dependence on pH with a minimum close to neutral conditions (Amram and Ganor, 2005; Bickmore et al., 2001; Marty et al., 2011; Metz et al., 2005; Oelkers et al., 2008; Robin et al., 2016). Such behavior is typical for a variety of aluminium silicates (Brantley et al., 2007; Walther, 1996) and could be explained by the critical role of OH^- and H_3O^+ for the hydrolysis of Si-O and O-Me bonds respectively. First insight into the molecular mechanism of the dissolution process of silicates was obtained through *ab initio* studies of small molecular clusters (Criscenti et al., 2006; Criscenti et al., 2005; Nangia and Garrison, 2009; Pelmenschikov et al., 2001; Pelmenschikov et al., 2000; Xiao and Lasaga, 1994; Xiao and Lasaga, 1996). These studies investigated activation barriers for hydrolysis of single bonds on silica surfaces with different connectivity (for example, disiloxane in Xiao and Lasaga, 1994,

1996 versus Q2 and Q3 silica in Pelmenschikov, 2000) and environment (one water molecule versus four in Criscenti et al., 2006), size of the Si clusters and constrained (Pelmenschikov et al., 2000) or unconstrained terminal atoms (Criscenti et al., 2006). Nangia and Garrison (2009) showed that, on the one hand, the difference of the activation barrier for the hydrolysis of the Si-O_b is small ($\Delta E \leq 9 \text{ kJ} \cdot \text{mol}^{-1}$), when considering different topologies like edge, kink or terrace sites. On the other hand, the pH conditions and thus the dominant protonation state of O_b on the surface have a major impact on the activation barrier. All of these findings above can be transferred to clay minerals to some extent, at least to the silicate sheets.

Recently, large-scale ab initio molecular dynamics simulations have been applied to simulate the mechanism of (110) surface of pyrophyllite at neutral pH (Schliemann and Churakov, 2020). The simulations revealed that the dissolution is a complex multistep process, which can be rationalized as a sequence of concurrent and reversible elementary reaction events, leading to a step-by-step decrease of the surface site density and eventual release of the silanol and aluminol complexes into solution. The essential reaction rate controlling events are the nucleophilic attack of H₂O molecules or OH groups on the metal – oxygen bonds, ligand (OH⁻, H₂O) exchange reactions in the first coordination shell of the reacting sites, and the collective proton transfer reactions between the acidic and basic oxygen sites on the edge surface. In this work we apply large scale meta-dynamic simulations (Laio and Parrinello, 2002) to further investigate the mechanism of silanol and aluminol leaching on (010) edge surface of pyrophyllite under elevated pressure conditions. The result of the modelling is compared with our recent study of the dissolution mechanism on the (110) edge of 2:1 phyllosilicate. The simulations provide insight into the mechanism of etch pit formation of the edges of phyllosilicate, which is essential for understanding the surface complexation mechanism of ions on the edges and the initial stage of clay mineral dissolution. The particular strength of the selected approach is the consideration of explicit solvent, which allows taking into account the realistic solvent surface interaction. The system setup corresponds to leaching at neutral pH in deionized water at far from equilibrium conditions with density (i.e. pore water pressure) that corresponds to a clay mineral with water content below 0.1 g g_{clay}⁻¹ (Bahramian et al., 2017).

4.2 Methods

The simulations setup and methodology follow a similar approach previously used in our study of pyrophyllite dissolution mechanism on the (110) edge (Schliemann and Churakov, 2020).

4.2.1 System setup

The simulated system was represented by one TOT-layer with (010) edge surfaces built on the basis of an ideal pyrophyllite structure (Fig. 4.1). The supercell dimensions of the explicitly modelled (010) edge surface spans three crystallographic lattice units of pyrophyllite in [100] direction and 1 lattice unit in [001] direction. The surface reconstruction and the surface speciation of the (010) edge is similar to the one previously investigated in Churakov (2007). The simulations were performed applying periodic boundary conditions. The initial dimensions of the simulated supercell were 40.0 Å x 15.7 Å x 10.0 Å. The pore space between (010) edge surfaces related by periodic boundary conditions was filled with H₂O molecules representing the bulk density of water in the middle of the pore for a lowly hydrated clay mineral. The composition of the simulated system was 12 x [Al₂Si₄O₁₀(OH)₃(OH₂)_{0.5} x 12H₂O].

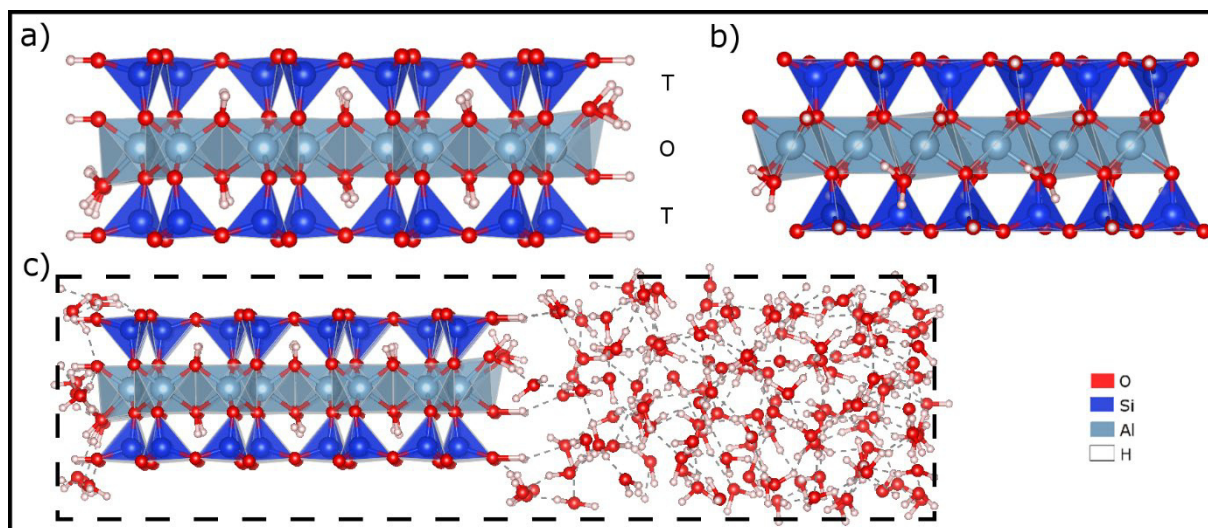


Figure 4.1: A snapshot from MD simulations showing the structure of (010) edge surface of pyrophyllite a) side view and b) front view of clay platelet without water for the sake of clarity, c) Side view of supercell showing the slit pore filled with water and the bounding box of the super cell.

Prior to the ab initio molecular dynamics simulations (AIMD), the distribution of water molecules in the slit pore was pre-equilibrated with classical MD simulations in NVT ensemble (constant Number of particles, Volume and Temperature) at 300 K for at least 1.0 ns using the CLAYFF force field (Cygan et al., 2004) and keeping the atomic positions of the clay particle frozen at their equilibrium position obtained by ab initio geometry optimization. This classical pre-equilibration runs were also used to pre-adjust the box size in b(y)-direction and the number of molecules in the system to ensure the increased water density in the middle of the pore space. Details of the pre-equilibration can be found in our previous study (Schliemann and Churakov, 2020).

4.2.2 Ab initio MD

The density functional theory (DFT) calculations were applied based on the PBE-D3 exchange correlation functional (Perdew et al., 1996) augmented with dispersion correction developed by Grimme (2004). Norm-conserving dual-space Goedecker-Teter-Hutter pseudopotentials were used to describe the core electrons (Goedecker et al., 1996). The valence electron wave-functions were built with DZVP Gaussian basis set. For the auxiliary electron density, we used plane wave basis sets with an energy cut-off of 400 Ry. The simulations were performed in the Born-Oppenheimer approximation. The AIMD simulations were conducted at 300 K in the NPT ensemble with the Canonical Sampling Velocity Rescaling (CSV) thermostat (Bussi et al., 2007). The equations of motion were integrated with 0.5 fs time step. At each MD step the wave functions were converged better than 3×10^{-7} Ha. This setup has been proven to reproduce structural data of 2:1 phyllosilicates in our previous simulations (Kéri et al., 2017; Kéri et al., 2019).

4.2.2.1 MetaDynamic simulations

The dissolution of ions from mineral surface is a rare event with a high activation energy barrier. The MetaDynamics (MetaD) method (Laio and Parrinello, 2002; Iannuzzi et al., 2003) was used to sample the free energy surfaces (FES) for the detachment of tetrahedral and octahedral sites. The reaction progress was monitored by a set of collective variables (CV),

describing the change in the coordination environment, i.e. change of the coordination number (CN) of the reacting site given by the following equation:

$$CN_I = \sum_{j=1}^{N_j} \frac{1 - \left(\frac{R_{Ij}}{R_{0Ij}}\right)^i}{1 - \left(\frac{R_{Ij}}{R_{0Ij}}\right)^k}, \quad (4.1)$$

where, j is the index of the species coordinating the atom of interest, i and k are exponents, R_{0Ij} , are the characteristic bond length parameters depending on the atom types involved and R_{Ij} is the actual bond distance between atoms I and j . The parameters and detailed description of uncertainties associated with the choice of simulations setup and the modelling parameters are provided in the Supplementary Information (Table 4.S1). This set of collective variables was found to provide a distinctive description of reactants and products emerging in the course of the dissolution process as well as the geometry of the transition state activated complexes (Schliemann and Churakov, 2020).

Depending on the simulation parameter and the type of reaction, the detachment of a silanol or aluminol group could be observed within 50-200 ps long MetaD trajectory. The evolution of the collective variables and representation of FES surface is provided in the Supporting Information (Figs. 4.S3 and 4.S4). The results presented in this study emerge from several ab initio MetaD trajectories with total length of nearly 250 ps.

Detailed analyses of uncertainties in MetaD simulations of phyllosilicate dissolution was provided in our previous work, based on the analysis of several independent simulations with different initial conditions. For the given parameters of the simulations the best estimate of the uncertainty on the free energy could be derived as two times the height of the Gaussian hills used for the FES sampling. The hill size used in the simulations was $7.88 \text{ kJ} \cdot \text{mol}^{-1}$. Accordingly, the uncertainty in the sampled FES is estimated as $\pm 15.0 \text{ kJ} \cdot \text{mol}^{-1}$ (Schliemann and Churakov, 2020)

4.3 Results

The results reported are obtained by the direct analysis of collective variables and atomic configurations from the ab initio MetaD trajectory. The free energy surface controlling the reaction mechanism is the function of reaction coordinates. In the MetaD approach, the free energy of the system is projected to the reduced space spanned by the collective variables (reaction coordinates). In complex systems like the one considered in this work the same reaction can occur via several concurrent mechanisms. The reactants and reaction products can be connected via several reaction pathways with distinct reaction intermediates, which are separated by multiple activation barriers. Given the simulation uncertainties, the evolution of the atomic configuration in a MetaD trajectory is expected to follow the lowest energy path between reactants and products. These are the configurations reported in the following section. Alternative reaction pathways, eventually with the slightly higher activation barriers are not represented by the molecular trajectory. Further indirect information about alternative reaction pathways can, however, be devised from the analysis of the full FES in the space of reaction coordinates. In general, the obtained FES can be used for the coarse grain simulations of the reaction kinetics. The dissolution mechanism typically involves several molecules and functional groups which are difficult to visualize in a simple 2D projection. Therefore, the reaction steps are illustrated by schematic diagrams and, if appropriate,

accompanied with the snapshot of the simulation. The oxygen sites involved in the reaction steps are designated with roman numbers (i, ii, ...). The same notation is used for the equations and the description in the text. To indicate the structural environment of the reacting surface sites, the coordination with respect to the bridging oxygen sites is provided in parentheses in the equations, when necessary. For example, the structural formula $\text{Al}(4)(\text{OH})$ indicates that Al is coordinated by four bridging oxygen sites and one OH group, whereas $\text{Si}(3) - \text{O} - \text{Si}(2) - \text{OH}$ describes two Si tetrahedra sharing a bridging oxygen site. The Si site on the left side of the formula is coordinated by four bridging oxygens, whereas the Si site on the right side is coordinated by three bridging oxygens and one OH group. In order to distinguish the dissolving reactive site from the environment in the schematic figures, the detaching complex is subscripted with a d, i.e. Al_d and Si_d .

4.3.1 The mechanism of Al edge surface leaching from the octahedral sheet

The outermost Al site on the (010) edge of pyrophyllite is six – fold coordinated. Its first coordination shell includes one hydroxyl group, one OH_2 molecule and four bridging oxygen atoms, which are shared with neighbouring silicon tetrahedra and aluminium octahedra (Fig. 4.2).

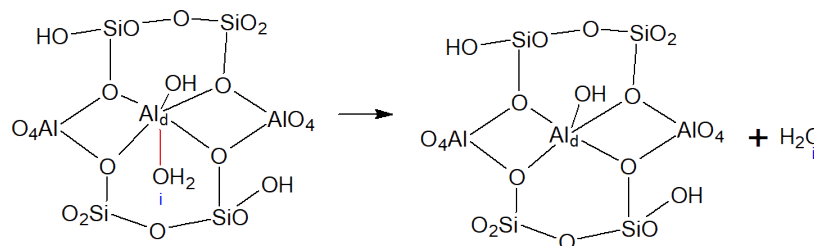
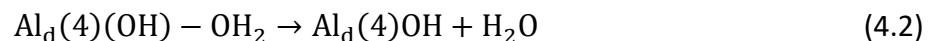


Figure 4.2: Reversible H_2O de-resorption reaction step of the Al detachment (see Eq. 4.2). The OH_2 group in the coordination shell of the detaching species stretches the bond to the surface and migrates into the pore water. This reaction step is reversible, meaning that several repeating adsorption and de-sorption of H_2O onto Al site has been observed in the simulations prior to the complete detachment of the surface group.

The adsorption free energy of the OH_2 group on the (010) edge is estimated to be about $21 \text{ kJ} \cdot \text{mol}^{-1}$ (Liu, 2012). The first reaction step observed on the (010) is the reversible de-sorption of the H_2O molecule from Al site. A similar behaviour was also observed in the simulations of the leaching on (110) edge surface (see (Schliemann and Churakov, 2020)). Spontaneous desorption of water on pyrophyllite and montmorillonite were reported in previous *ab initio* simulations.



The de- and resorption of water molecules destabilize the coordination polyhedron of the surface aluminium site. Several cycles of the H_2O de- and resorption events cause elongation of interatomic distances within the first coordination shell of the surface Al and distort the coordination polyhedron. The reaction proceeds with the nucleophilic attack of a water molecule at the interface on the six-fold coordinated Al site. Two out of four bridging oxygen sites (O(iv) and O(v)) leave the coordination shell of the leaching Al site. The Al ion forms a bidentate complex coordinated by two water molecule and an OH group. Shortly after the change of denticity, the O(ii)H group in the coordination shell of the Al site accepts a second proton and becomes doubly protonated. The final configuration of the reaction product in this

step is represented by a five-fold bidentate complex linked to the edge surface via two bridging oxygen sites and coordinated by three H₂O molecules (see Fig. 4.3 and Eq. 4.3).



The next reaction step observed in the trajectory represents a change of the Al conformation from the bidentate to a monodentate state. The reaction takes place without direct invol-

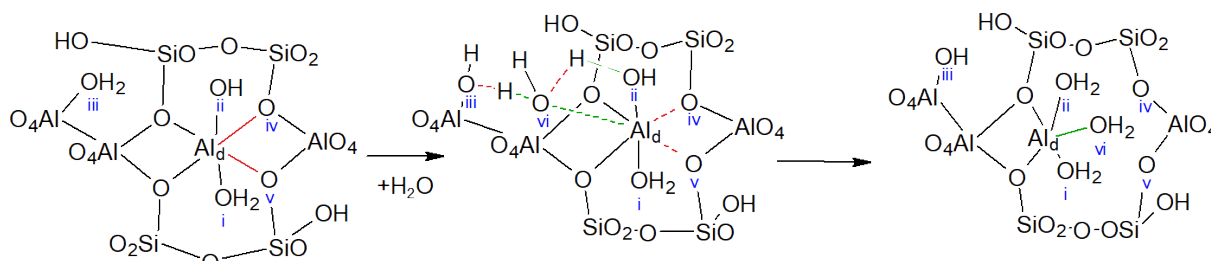


Figure 4.3: First Al-O bond hydrolysis step of the Al detachment (Eq. 4.3). In this step a water molecule approaches the six-fold coordinated Al surface site and the CN of this site temporary increases to seven. Consequently, the bonds to the two bridging oxygens (O(iv) and O(v)) elongate and eventually break, resulting in a bidentate configuration of the Al_{det}. Red solid lines indicate the hydrolysing ion-covalent bonds in the products. The same bonds are shown by red dashed lines in the intermediate activated complex and green dashed lines indicate forming bonds.

vement of surrounding molecules or functional groups. The reaction step results in the changes of Al coordination from five- to four-fold. The neo-formed mono-dentate complex is attached to bridging oxygen(viii) and coordinated by three water molecules (see Eq. 4.4 and Fig. 4.4).

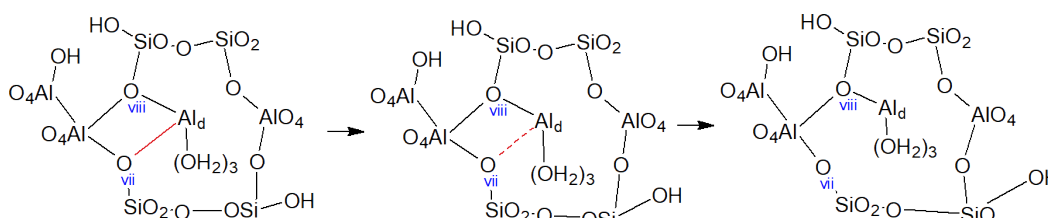
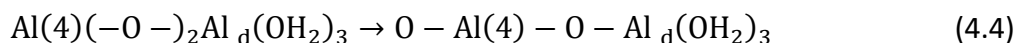


Figure 4.4: In this intermediate reaction step (see Eq. 4.4) the Al-O(viii) bond is breaking and the bidentate surface complex transforms into a mono-dentate one. Unlike the other reaction steps, the conformational change is not triggered by a nucleophilic attack.

The last reaction step leading to the full solvation of Al ion and formation of an outer-sphere complex at the interface is triggered by the nucleophilic attack of a water molecule on the four-fold coordinated mono-dentate Al complex. While the water molecule from the interfacial solution enters the Al coordination shell, Al_d moves away from the surface towards the water molecule (see Fig. 4.5, Eq. 4.5). The activated complex has five-fold coordination. The elongated O(viii)-Al bond breaks and the neo-formed tetrahedrally coordinated Al complex detach from the surface. Simultaneously, two out of four OH₂ groups in the tetrahedral coordination shell of the detaching Al site donate one proton each to the O(iv) and O(iii) surface sites coordinating Si tetrahedron and Al octahedron, respectively. At the end of

this reaction step the solvated aqueous complex is coordinated by two OH groups and two OH₂ molecules.

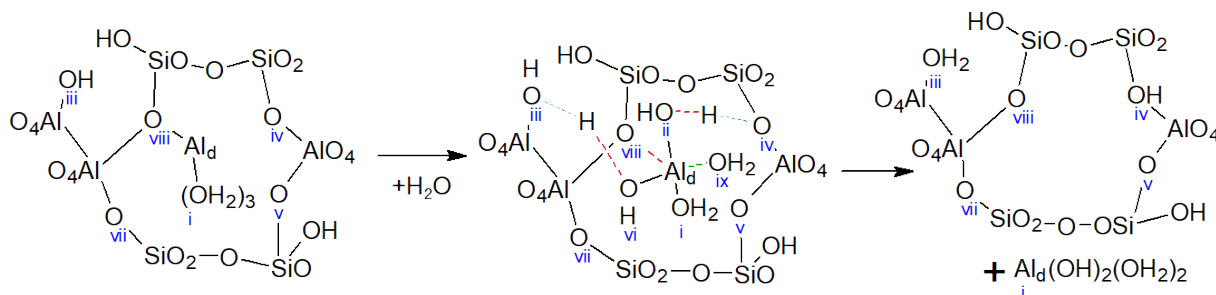
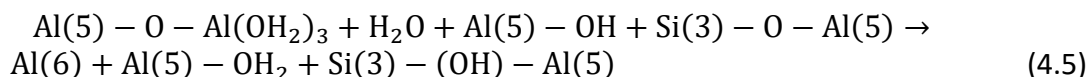
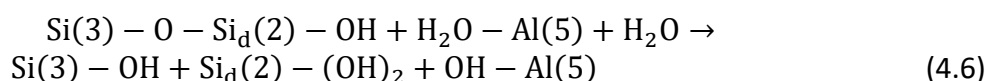


Figure 4.5: The last reaction step leading to the release of Al into solution is initiated by a nucleophilic attack of water molecule to a mono-dentate Al complex attached to the O(viii) site (see Eq. 4.5). A water molecule enters the coordination shell of the four-fold coordinated surface complex and contribute to formation of a five-fold coordinated activated complex. This transient is temporary stabilised by a complex network of HBs. That HB- network further controls rearrangement of the geometry as well as the directional proton transfer mechanism taking place in the course of the reaction step. Either of two water molecules in the coordination shell of the five-fold activated complex donate a proton to -O(iii)H and the bridging oxygen -O(iv) surface site at the edge surface. Eventually, Al moves away from the -O(viii) surface site and the neo-formed tetrahedral coordinated complex Al(OH)₂(OH)₂ leaves the surface and forms an outer sphere complex at the interface.

4.3.2 The mechanism of Si edge surface leaching from the tetrahedral sheet

The detachment of a single silicon atom from the (010) edge surface of pyrophyllite is a complex multistep reaction with several reaction intermediates that differ only slightly in their bond topology. These intermediate structures are encountered several times in the course of MetaD trajectory as it can be seen through the frequent fluctuations in the COLVARs with time (see S3 in Supporting Information).

The leaching of Si at the (010) edge surface starts with a nucleophilic attack of a water molecule on the four-fold coordinated tridentate Si species. The water molecule enters the coordination tetrahedron of the surface Si site and triggers the formation of a five-fold coordinated activated complex with elongated Si-O bonds. The structure intermediate with the water oxygen O(ii)H₂ entering the Si coordination shell and the HBs topology responsible for the proton transfer reactions in the course of the surface conformation is shown in Fig. 4.6 (b and e). The resulting bidentate reaction product is shown in Fig. 4.6 (c and f). The conformation of the bidentate complex is stabilised by the proton transfer reaction to the dangling oxygen sites formed as result of the hydrolysis of the Si-O-Si bond. The Si-O(i) site on the surface accepts a proton transferred from the OH₂ group coordinating the neighbouring Al surface site. In the course of the simulation a proton was observed to exchange repeatedly between O(ii) and O(vi) oxygen sites in the octahedral and tetrahedral sheet, respectively:



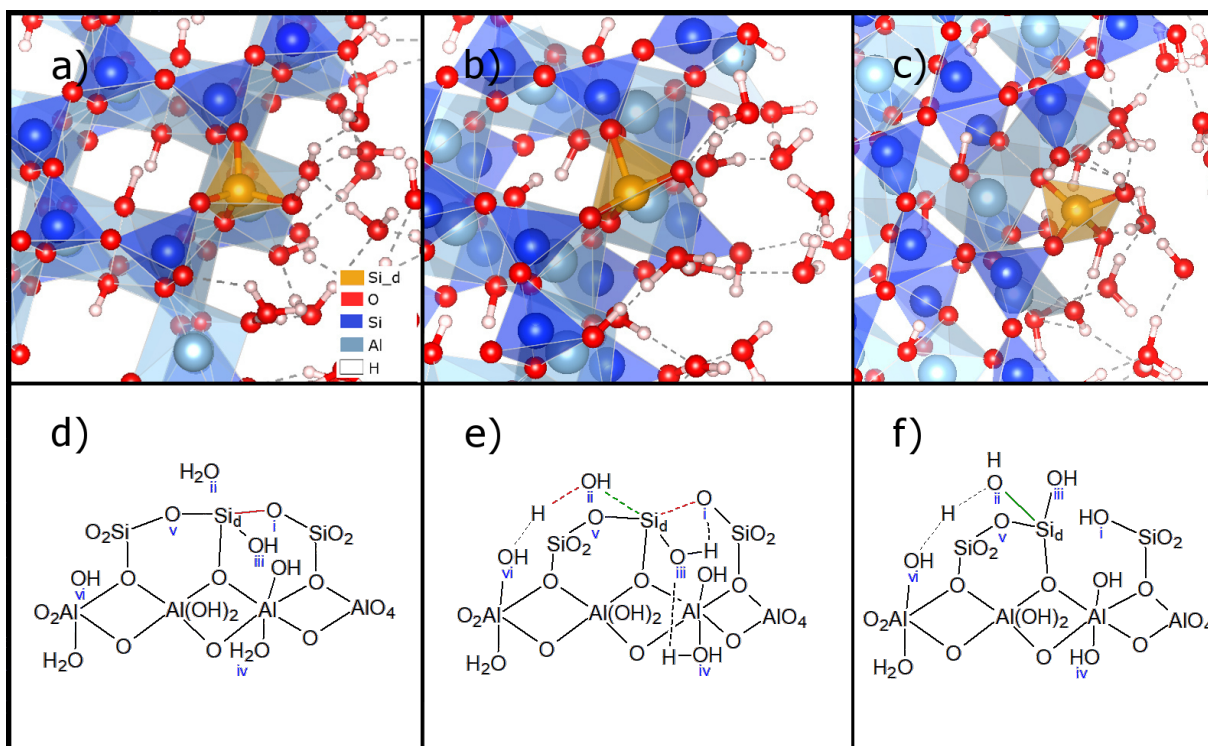
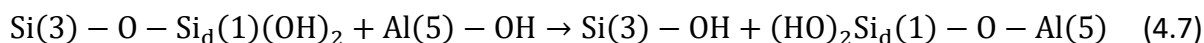
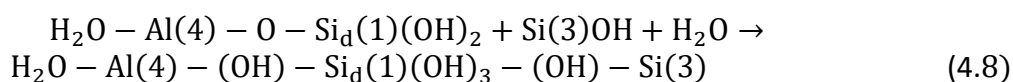


Figure 4.6: The edge surface Si leaching is initiated with a nucleophilic attack of a water molecule (b and e). The activated complex of Si is five-fold coordinated and has elongated Si-O distances. As result of the reaction the Si_{det}-O(i) bond breaks and a bidentate complex is formed in which the Si-tetrahedron keeps one bond to the tetrahedral layer and one bond to the octahedral layer (c and f). The dangling oxygen O(i) is protonated through collective hydrogen transfer event along a chain of hydrogen bonds in which the O(iv)H₂ group act as a net proton donor (Eq. 4.6).

In the course of the leaching process, the bidentate complex shared between the tetrahedral and octahedral sheet is transformed into another bidentate complex shared between two neighbouring Al sites in the octahedral sheet of the pyrophyllite particle (Fig. 4.7, eq. 4.7). The activation complex formed in this reaction has an octahedral coordination. The intermediate reaction products are stabilised by the proton transfer from the OH group coordinating Al octahedra to a dangling Si-O bond formed after change of the surface complex conformation. This net proton transfer reaction is a result of collective proton transfer event taking along a chain of hydrogen bonds formed by several H₂O and OH groups.



The detachment of Si from (010) edge of pyrophyllite continues by the nucleophilic attack on the bidentate-dentate Si-complex (Fig. 4.8, Eq. 4.8). In this reaction step, an H₂O molecule in the second coordination shell enters the coordination of tetrahedral Si complex. The activated complex is represented by a trigonal bi-pyramide comparable to the intermediate in the previous step (Fig. 4.7 b). The leaching Si atom approaches another oxygen site on the edge surface and adopts an octahedral coordination. One proton from the O(viii) site is transferred to the O(vi) site through a HB chain including surrounding H₂O molecules.



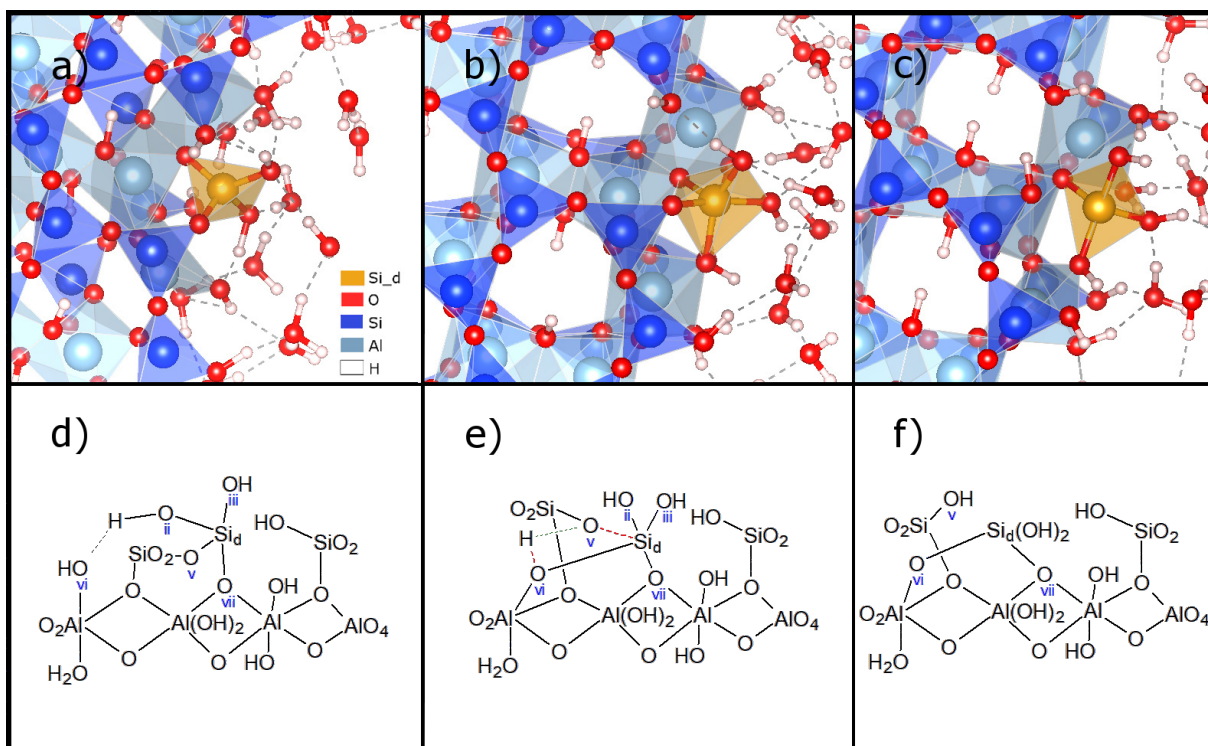
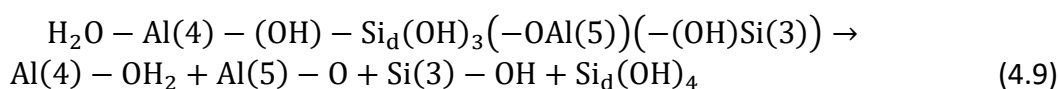


Figure 4.7.: The Illustration to reaction in Eq. 4.7, showing the transformation of a bidentate complex with one bond to the tetrahedral sheet (O(v)) and one bond with the octahedral sheet (O(vii)) into another bidentate complex with two bonds to the octahedral sheet (O(vi) and O(vii)). The hydroxy group (O(vi)H) of an adjacent Al site makes a nucleophilic attack and temporarily changes the CN of the detaching Si to 5 (b and e). After the rupture of the Si-O(v) bond, the neoformed bidentate complex is shared by two neighbouring Al octahedra via O(vi) and O(vii) (c and f). The reaction products are stabilized by the proton transfer reaction from O(vi)H to the dangling Si-O(v) site.

The last step of the Si leaching process was found to be the desorption of the tridentate inner sphere $\text{Si}(\text{OH})_4$ complex connected to the octahedral Al sheet via Al-(OH)-Si, Al-O-Si and Si-O-Si bond breakage and formation of the outer-sphere complex stabilised by hydrogen bonds close to the edge surface (Fig 4.9. Eq. 4.9). Eventually this complex leaves the surface and forms a solvated $\text{Si}(\text{OH})_4$ molecule in the interstitial solution.



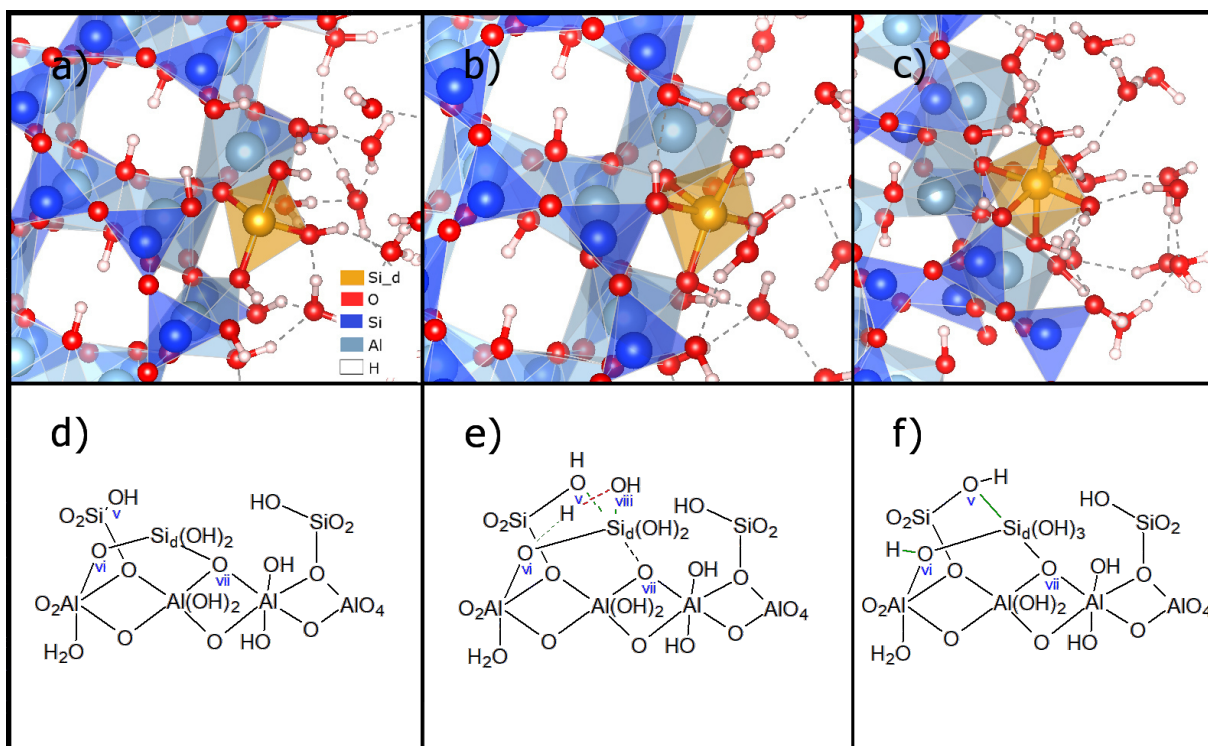


Figure 4.8: The illustration to the reaction in Eq. 4.8, showing the conformational changes of the bidentate surface complex (c and f). The reaction starts with a nucleophilic attack of a water molecule on the Si_d (b and e), which simultaneously forms a bond to the tetrahedral sheet. The bond formation with the attacking water leads to the elongation of the Si-O-Si and the other Si-O bonds. Together with the other five coordinating oxygens an octahedral structure of the leaching Si site forms. The octahedral complex is stabilised by a proton transfer from the O(viii)H_2 water molecule to the bridging oxygen site (O(vi)).

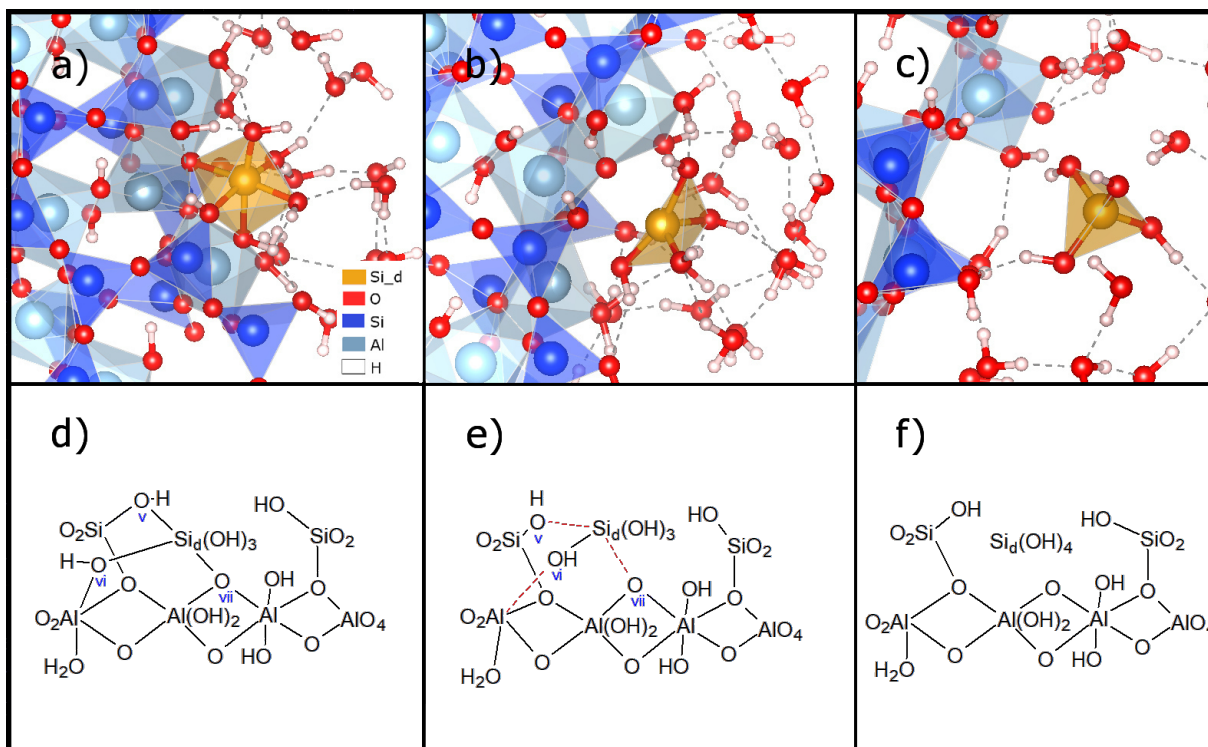


Figure 4.9: The last step of the detachment mechanism is the completion of the single tetrahedra dissolution from the (010) edge surface. The Si-O(vii), Al-O(vi) and Si-O(v) bonds

elongate (b and e) before they rupture and a free silicic acid ($\text{Si}(\text{OH})_4$) molecule emerges (c and f).

4.3.3 Activation energies

The activation barriers were obtained analysing the free energy surface (FES) collected at the end of the MetaD simulations following the same procedure used in our previous work (Schliemann and Churakov, 2020). Several local minima in the FES correspond to initial, intermediate and final reaction products e.g. an etch pit on the (010)-edge surface and a solvated Al or Si ion. The minimum energy pathway and the values of the activation barriers can be derived from the saddle points connecting these states. Accurate and complete sampling of FES require, in general a multiple re-crossing of the barriers separating reaction products and intermediate states. Due to the uncertainties associated with completeness of the free energy sampling, the activation energies for the reverse reactions are not reliable. Therefore, the activation energies are provided for the forward reactions only (Table 4.1). Detailed analysis of uncertainties related to a potentially incomplete FES is provided in Schliemann and Churakov (2020).

Analysis of activation energy barriers associated with the step-by-step leaching of the Al ion from the (010) edge surface with high-pressurized pore water, indicate that the largest activation barrier corresponds to the reaction expressed in Eq. 4.4. In this step, the Al ion leaves the structural position corresponding to the octahedra in the bulk structure and forms a bidentate complex attached to the edge surface. Considering the fact that the activation for this reaction step is substantially higher than the activation energy for the other intermediates, this reaction step can be viewed as a rate limiting one. With the exception of the reaction step described by Eq. 4.3, the activation barriers for the intermediate reaction steps predicted for the Al leaching are lower compared to the ones reported for the Si leaching. The same trend was also observed for the dissolution of (110) edge surface (Schliemann and Churakov, 2020).

Table 4.1: Estimated forward activation energies for each elementary reaction step of Al and Si leaching from the ideal (010) edge surface of pyrophyllite under elevated pressure conditions.

Al	Equations	2	3	4	5
	E_A [kJ · mol ⁻¹]	8.7	172.3	15.3	52
Si	Equations	6	7	8	9
	E_A [kJ · mol ⁻¹]	146.9	10.9	154.9	157.9

The leaching mechanism of the Si observed in the simulated trajectory also comprises 4-intermediate reaction steps (Eq. 4.6-4.9). The activation energies of the first three reaction steps (Eq. 4.6, 4.8 and 4.9, respectively) are nearly the same within the uncertainty of the simulations. The same order of magnitude for the activation energies were reported in the study of Si dissolution at the (110) surface (Schliemann and Churakov, 2020). On the contrary, the activation energy for the Eq. 4.7 is an order of magnitude lower. The reaction step represents the ligands exchange in the coordination shell of the tetrahedral Si surface complex, which do not change the net density of the complex, but the identity of the surface complexation sites.

4.4 Discussion

The observed dissolution mechanisms of Si and Al on (010) is consistent with the one documented in our study of the pyrophyllite dissolution on the (110) edge surface. In general, the overall reaction process can be described as a sequence of reversible step-by-step elementary reaction events which change the denticity of the surface group or a surface ligand exchange. These structural changes result in the weaker bonding of the leaching complex and eventual release of the Al/Si oxygens from the surface into solution. For the vast majority of the observed elementary reaction steps, the change in the denticity of the detaching surface complexes was triggered by the interaction with a nucleophilic oxygen agent, such as a nearby OH group or water molecule. Typically, a nucleophilic agent enters the first coordination shell of the surface complex, contributes to the temporary increase of the coordination number and causes elongation of the existing bonds to the surface sites. Formation of the activated complex with an increased coordination number and the elongated metal-oxygen bonds in the first coordination shell leads to the destabilisation of the surface complex and creates the necessary preconditions for the change of the surface complex denticity or ligand exchange (see Fig. 4.2-4.6). For the non-symmetric Si-O-Al bond chain, it is the Al-O bond, which has the lower bond energy. Consequently, the Al-O bond is expected to have lower activation energy and to hydrolyse more readily. For the symmetric Si-O-Si or Al-O-Al bond chains the reaction steps are determined by the local coordination of molecules at the interface. In either chemical environment, the dangling oxygen sites emerging after the hydrolysis events are strong proton hydrogen bond acceptors. The further stabilisation of surface complexes with the lower denticity is accomplished by the protonation of dangling oxygen sites with high proton affinity (see Figs. 4.3, 4.6 (e, f) and 4.7 (e, f)). The proton donors in these proton transfer reactions are the more acidic groups on the surface, which are either the H₂O molecules initiating the nucleophilic attack (see Figs. 4.5, 4.6 (O(ii)) and 4.8) or the OH_x-group of an aluminol site (see O(ii) and O(vi) in Fig. 4.3 and O(iv) in Fig. 4.6).

The elementary reaction steps can be revealed and back-traced by analysing the evolution of the instantaneous values of CV along the MetaD-trajectory (see Figs. 4.S3 and 4.S4). At ambient conditions, the most stable coordination of Si with oxygen is the tetrahedral one. The analysis of the trajectory shows that the local minima on the FES, correspond to different conformations of Si tetrahedra on the edge surface. In the course of such elementary reaction events, the CN of Si with respect to ligands (OH, O_b or OH₂) was found to vary from three to five and even become six-fold for a short simulation interval. A five-fold coordination is typically observed when a nucleophilic agent approaches the tetrahedral reacting site. The short lived three-fold coordination is observed during the ligand exchange event, which leads to the decrease of the surface complex denticity. The CN of the Al site was found to change between 4 and 6 during the reaction. Interestingly, the tetrahedral coordination was very common for the reaction intermediates corresponding to the local energy minima in the FES.

It is interesting to compare the leaching mechanism of the (010) and (110) edge surfaces of pyrophyllite. The major differences are in the sequence and eventually in the number of the elementary reaction steps. Especially for the octahedral Al site, these reaction steps are characterised by distinct activation barriers. These differences in the reaction mechanism can be related to the distinct coordination of the surface sites on the (010) and the (110) edge. While the bond topology of the silicon species on the pristine (010) surface is almost the same as on the (110) surface (i.e. two O_b connecting to the tetrahedral sheet, one to the octahedral sheet and a hydroxyl group), the Al sites have substantially different coordination.

The major, eventually rate limiting reaction events for the leaching of Al, are related to the hydrolysis of the M-O_b-M bonds on the pristine surface. The coordination shell of the Al site on the (010) surface has fewer O_b ligands than the corresponding Al site on the (110) surface and thus the leaching process could, potentially, be accomplished in a fewer number of steps. Indeed, the detachment of Al encounters three major activation barriers in contrast to four or six on the (110) edge surface.

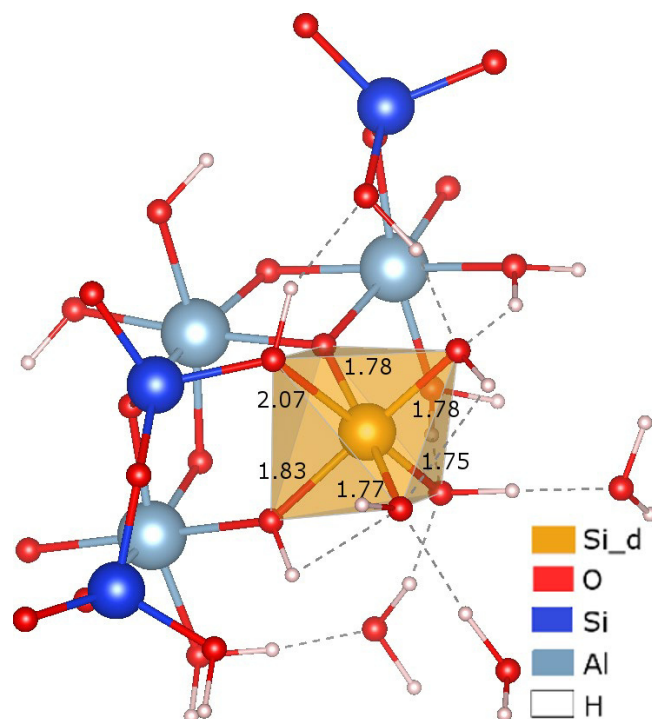


Figure 4.10: Snapshot of the optimized geometry of the intermediate octahedral configuration (orange polyhedron) in Fig. 4.9 a and d. The bond length of all six Si-O bonds is indicated next to them. Only the most relevant atoms in the first and the second coordination shell are shown.

The planar pseudo orthorhombic symmetry of the (010) edge differs from the oblique, grafted (110) edge. This difference in structural environment explains the higher barrier for the initial step of Al leaching on the (010) compared to the (110) edge. The reversible dehydration of the aluminol site has a low activation barrier, which means the bonds to the bridging oxygen sites at the edge surface need to be stronger to charge balance (screen) the Al site. Furthermore, the two protonated oxygen sites on the initial Al configuration (see Fig. 4.1 a) make it sterically more difficult for water or OH groups to initiate the nucleophilic attack on the Al site on (010) edge compared to the respective site on the (110) edge coordinated with just one OH₂ group.

The Si site at the (010) edge on the other hand must overcome four energy barriers (see Table 4.1), which is the same as for the Si_{T2} dissolution on the (110) edge. Not only the number of intermediate reaction steps was found to be the same, but also the initial sequence of reaction steps is very alike. The Si_{T2} detachment includes an intermediate state in which it has two bridging oxygen connected solely to the octahedral sheet is exactly the same as can be observed in Fig. 4.8 a) and d).

Some very peculiar surface complex geometries are observed in the last two steps of Si leaching from (010) edge prior to the formation the aqueous silicic acid. The Si site was found to adopt an unusual six-fold octahedral coordination (see Fig. 4.10). The geometry of the octahedral surface complex and time evolution of the interatomic distances and bond angles

is reported in the Supplementary Figs. 4.S5 and 4.S6. Additionally, we provide the analysis of the wannier centers of the molecule orbitals in the supplementary as well (Fig. 4.S7). The analysis of bond angles clearly demonstrates the octahedral geometry is maintained over a period of 20 ps. Five out of six Si-O bond distances have an average value of 1.75-1.85 Å. One distance is substantially longer (2.5 Å) and shows larger fluctuation during the simulation trajectory. A more detailed analysis shows a repetitive exchange of the ligand-Si distance between the short-range interaction at ~ 2.0 Å and longer Si O distance larger than 2.5 Å. It is important to emphasise that the octahedral geometry of the coordination shell, as defined by the bond angles is retained during this exchange. A simultaneous cell and geometry optimisation, starting from an arbitrary MD snapshot, was performed to check that the octahedral configuration does represent a local energy minimum. The optimised geometry is shown in Fig. 4.10.

The octahedral configuration for Si is very uncommon and is expected to be stable at ultrahigh pressure condition like in mineral stishovite forming above ~ 10 GPa pressure (Lyon et al., 1962; Ono et al., 2017). It is therefore essential to ensure that the observed results are not a modelling artefact. The simulations are performed in the NPT ensemble with the target temperature of 300 K and the global pressure of the barostat is maintained at 1 bar. Therefore, the system should be able to accommodate the supercell dimension to account to the changes in the specific molar volume of the surface complex in different conformations. This aspect could be relevant for the comparatively small system size used in ab initio simulations for the obvious reasons of the computational effort. The simulation cell used in these simulations is however significantly larger than in typical ab initio simulation. In the same time, it should be realised that the observed configuration is not an energetically favourable reaction product but a reaction intermediate, which has by its nature higher energy compared to the reactants and reaction products. Despite the fact that tetrahedral coordination of Si is expected to be thermodynamically more stable compared to the octahedral one at ambient condition, several factors can be responsible for the stabilisation of the observed 6-fold complex. The octahedral geometry of the complex was maintained in the system over the period of 20 ps of MetaD trajectory. This is a sufficiently long simulation period to argue that the configuration does reflect a conformation with a local energy minimum. We also performed geometry and cell optimisation starting from one of the MD snapshots to test whether molecular configuration is maintained. The optimised geometry retains the octahedral configuration with the five short bonds (1.75 to 1.83 Å) and one elongated bond at 2.07 Å. The structure was used to evaluate the maximally localised electronic orbitals, the Wannier centers. The results are compared with the similar calculations of the reaction intermediates. The simulation results show which electrons are localised closer to the oxygen sites in the Si-O bond in the 6-fold configuration compared to the Si in tetrahedral coordination confirming higher ionicity of Si-O bond in the octahedral geometry (Alvarez and Rez, 1998)

It is also clear that the octahedral configuration can only be stabilised by the confinement formed by the molecules in the second coordination shell of the octahedral silica complex. It to be expect that this confinement pressure should be comparable with the stability field of the six-fold coordinated silica. The question is whether and to which extent the liquid solid interface can sustain such local stresses. Recent simulations of the nano cavitation collapse at the water-silica interface reveal possibility of the shock waves emerging in the system due to the collapse of nano-cavitation at the interface and generating local pressures in the range of 10-18 GPa (Nomura et al., 2012; Shekhar et al., 2013). These local pressures persist in the system on the timescale of several tens of picosecond before the relaxation take place.

Actually, the simulation of Shekhar et al., 2013 also report formation of six-fold coordinated silica at the pitting region of silica-water interface. We speculate, therefore that strong confinement forces together with the increased water density could be sufficient to stabilise short lived octahedral geometry of Si at the interface. The forces can be sustained over a period of few tens of picoseconds and stabilise the typical high-pressure octahedral configuration of Si at the interface.

In the study performed for the (110) edge surface, the activation barriers of the leaching reactions at the octahedral sheet were significantly lower than that for the tetrahedral sheet. Contrary, the height of activation barrier for the rate limiting step of both the Si and Al dissolution on the (010) is roughly the same. This would suggest a congruent dissolution of the (010) edge, in contrast to (110) edge for which an incongruent initial dissolution scenario can be anticipated. Clay platelets are composed of (010) and (110) facets. The contribution of each edge surface type to the dissolution process will depend on the abundance of the crystallographic faces, which in turn depend on the surface energy controlled by the specific chemical environment including the pH condition and ionic strength of the solution. The ab initio simulations (Bickmore et al., 2003) and AFM observations (Kraevsky et al., 2020) suggest higher surface ratio (110) to (010) edges for most of the 2:1 phyllosilicates. The net macroscopic dissolution rate is still consistent with the experimental observations, which start with an incongruent dissolution preferential leaching of Al and later become limited by the rate of Si dissolution. Since pyrophyllite structure can be considered as a prototype to the wide range of phyllosilicates, the obtained result should be in general transferable for a broad range of phyllosilicate minerals at least qualitatively. Any isomorphous substitutions are expected to weaken bonds to the edge surface as their individual ion charges are lower than Al or Si, respectively. The co adsorption of ions is expected to have a significant influence on the strength of the surface bonds as well. Recent ab initio studies for example have revealed a significant effect of cation co-adsorption on the acidity of (OH) surface group on the silica surface (Pfeiffer-Laplaud et al., 2016).

4.5 Conclusion

Large scale quantum mechanical simulations of pyrophyllite dissolution at most important edge surfaces of pyrophyllite using enhanced sampling with MetaDynamics approach provide us with a unique insight into the molecular mechanism of the process for a large group of phyllosilicate minerals at far from equilibrium conditions. The results suggest that the overall reaction process can be described as the sequence of reversible step-by-step elementary reaction events, which change the denticity of the leaching surface group or is a surface ligand exchange leading to a different surface complexation mechanism on the surface. Independent of the edge surface type investigated the key molecular mechanism leading to the leaching of octahedral (Al) and tetrahedral (Si) sites is the nucleophilic attack of the OH and H₂O groups on the reaction surface site. In the course of the reaction, the nucleophilic agent enters the first coordination shell of the surface complex, temporary increases the coordination number and causes elongation of the existing bonds to the surface sites. Formation of the activated complex with an increased coordination number and the elongated metal-oxygen bonds in the first coordination shell leads to the destabilisation of the surface complex and creates necessary preconditions for the change of the surface complex denticity or a ligand exchange (see Fig. 4.2-4.6). Such an excited complex is more prone to the hydrolysis of the Al/Si – oxygen bonds responsible for inner-sphere complexation on the edge of the clay minerals. From this geometry of the activated complex it can either follow the reverse reaction or

forward reaction reducing the denticity and leading eventually to the detachment. The direction of the process depends on the additional stabilisation of the surface complex via the hydrogen bonding and the protonation of the dangling oxygen sites, which forms as the result of the bond hydrolysis.

The major difference is the mechanism of the Al dissolution, which includes one step less than on the (110) edge but includes a rate-limiting step with an activation barrier above $150 \text{ kJ} \cdot \text{mol}^{-1}$. This is almost twice as high as the rate limiting reaction step of the Al dissolution from the (110) edge. These differences appear to arise from the distinct topographies of both edge surfaces. That is true especially for the Al site, because the structural environment is clearly different, having one O_b exchanged by one OH group, when compared to its corresponding Al site on the (110) edge surface.

On the basis of obtained activation energies, the (010) edge is expected to follow a congruent dissolution pathway, whereas an incongruent preferential leaching of Al is anticipated for the (110) edge. The overall balance of Al and Si dissolution rate in a macroscopic system will depend on the relative abundance of (010) and (110) facets. The abundance of the different faces is likely to depend on the specific chemical environment of the system which influence the speciation and thus the relative stability of the surfaces.

4.6 Supporting Information

Table 4.S1: Parameters used for the CN in Eq. 4.1 of different neighboring elements during MetaD run (Taken from Schliemann and Churakov, 2021).

	Al-Al	Al-Si	Al-O	Si-O	O-H
R_0 [Å]	3.4	3.4	2.4	2.4	1.2
i	20	21	18	18	25
k	12	12	10	10	20

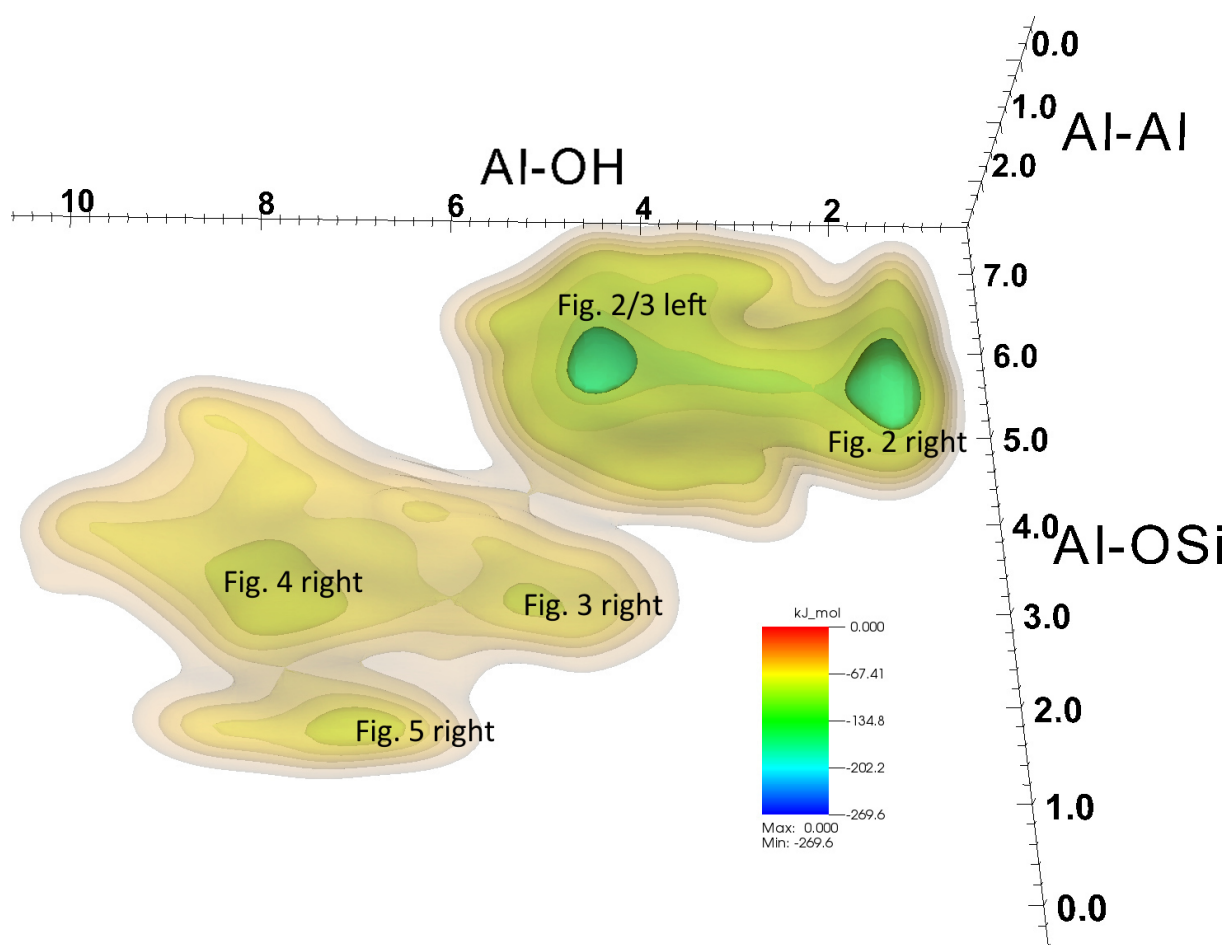


Figure 4.S1: FES for the Al detachment as obtained from the MetaD simulation with a hill size of $7.8 \text{ kJ} \cdot \text{mol}^{-1}$. The three CNs (used as coordinates in the graph) were defined according to Eq. 4.1 with the parameters from Table 4.S1. The clearly distinguishable states are labelled with their corresponding figure in the main article. The color scale shows the free energy of the displayed iso-surfaces in $\text{kJ} \cdot \text{mol}^{-1}$.

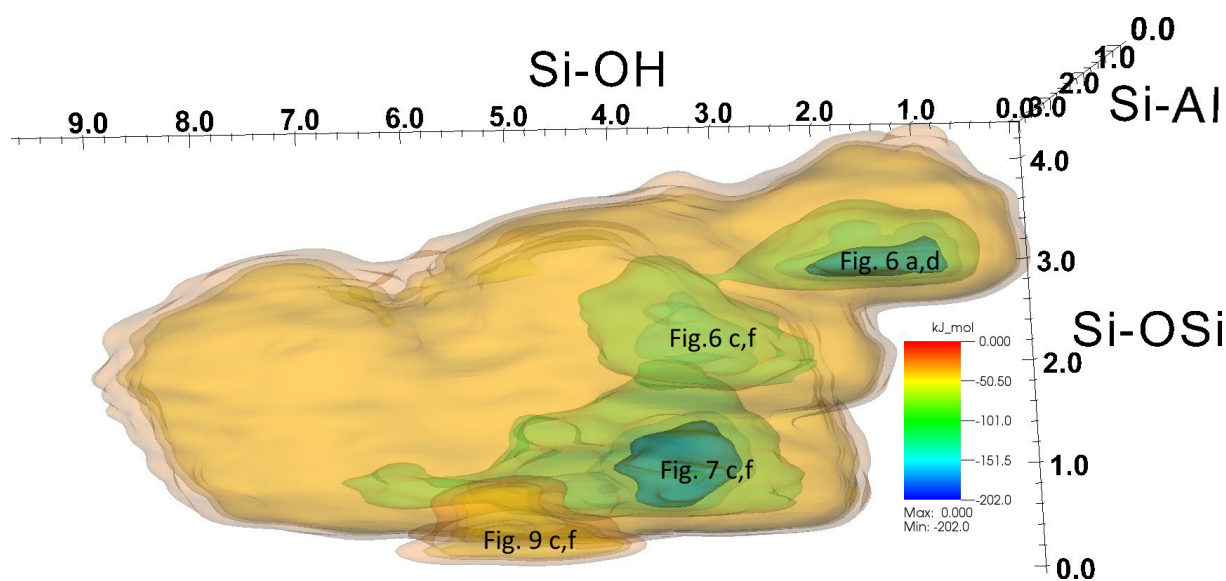


Figure 4.S2: FES for the Si detachment as obtained from the MetaD simulation with a hill size of $7.8 \text{ kJ} \cdot \text{mol}^{-1}$. The three CNs (used as coordinates in the graph) were defined according to Eq. 4.1 with the parameters from Table 4.S1. The clearly distinguishable states are labelled with their corresponding figure in the main article. The color scale shows the free energy of the displayed iso-surfaces in $\text{kJ} \cdot \text{mol}^{-1}$.

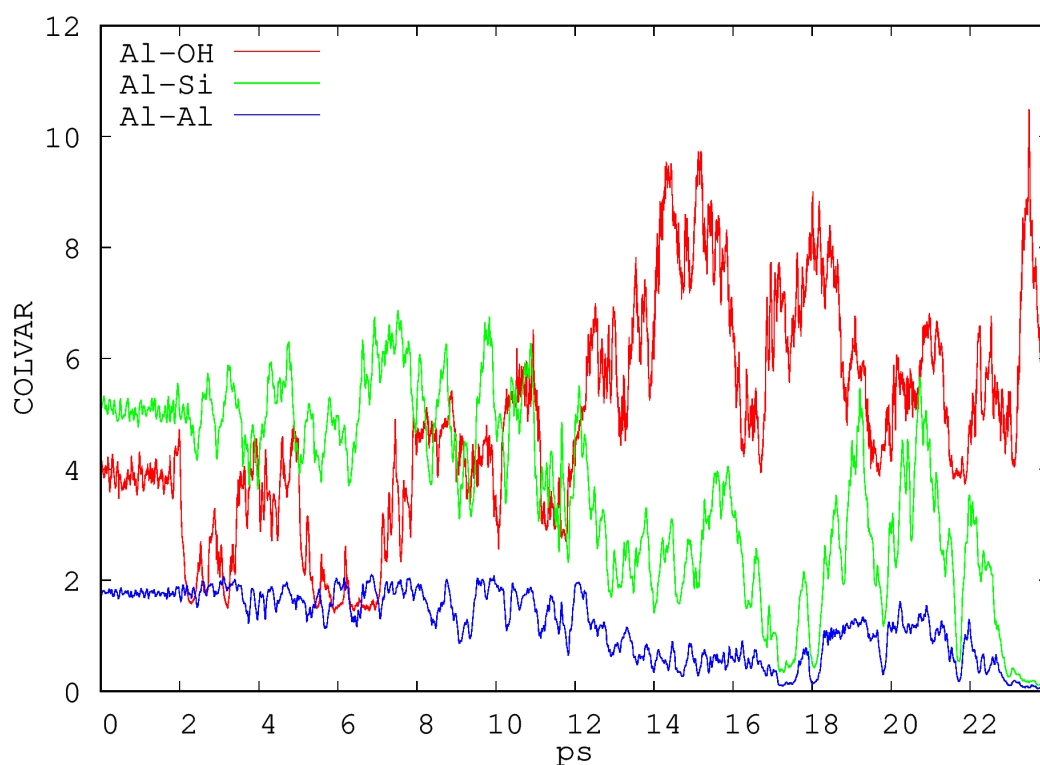


Figure 4.S3: The development of the collective variables for the Al detachment from the (010) surface with time as obtained by the MetaD simulations.

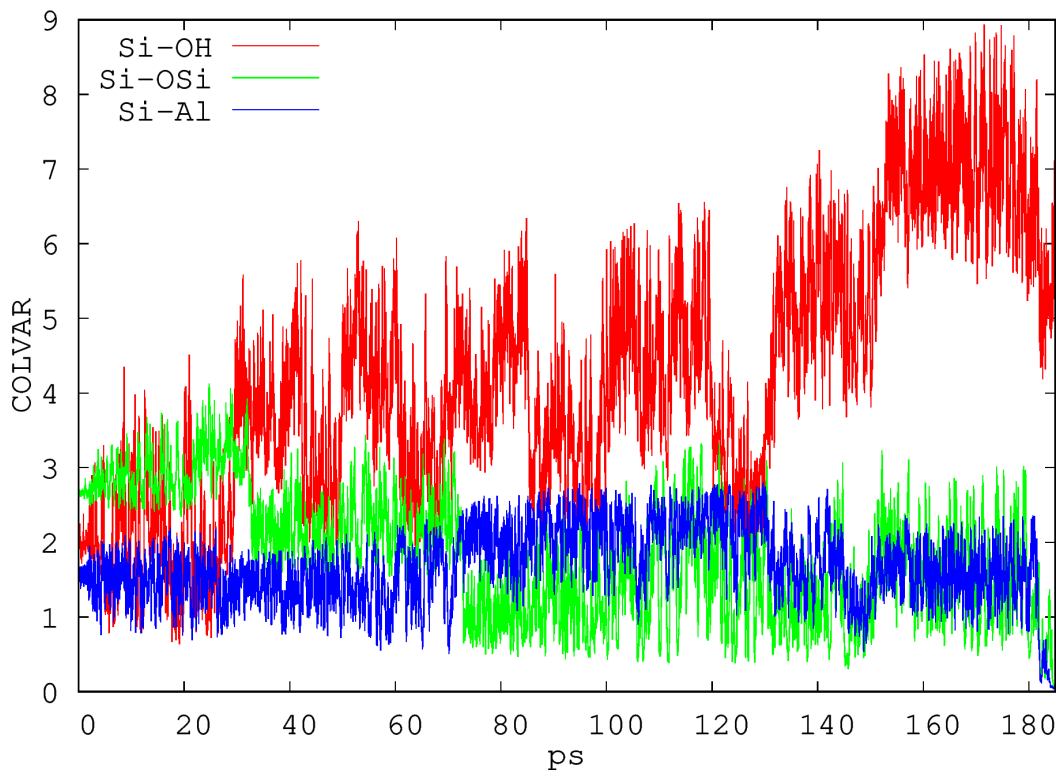


Fig. 4.S4: The development of the collective variables for the Si detachment from the (010) surface with time as obtained by the MetaD simulations.

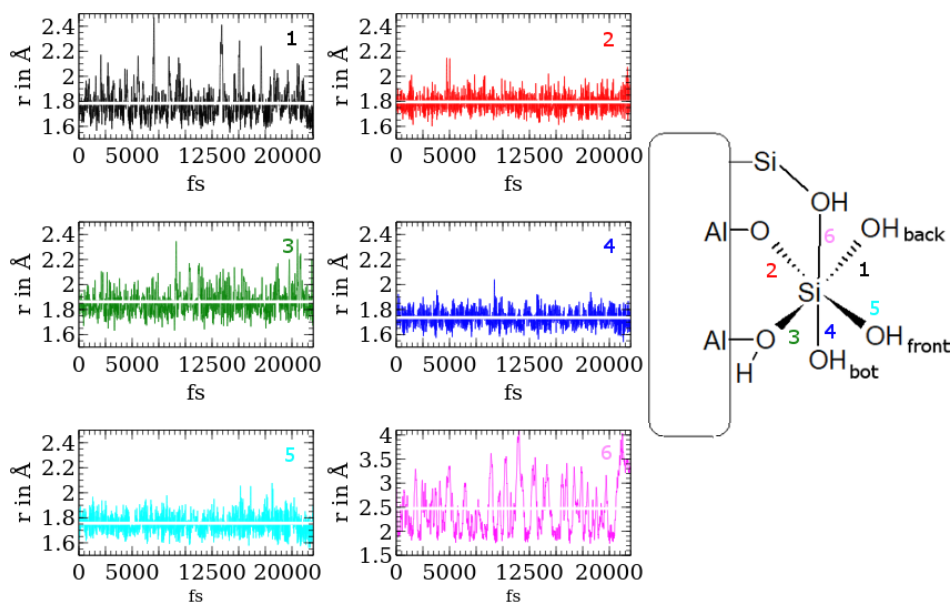


Fig 4.S5: Distances of the Si-O bonds for the octahedral Si from Eq. 4.8. In the right scheme all bonds are identified by the numbers linking them to the graphs.

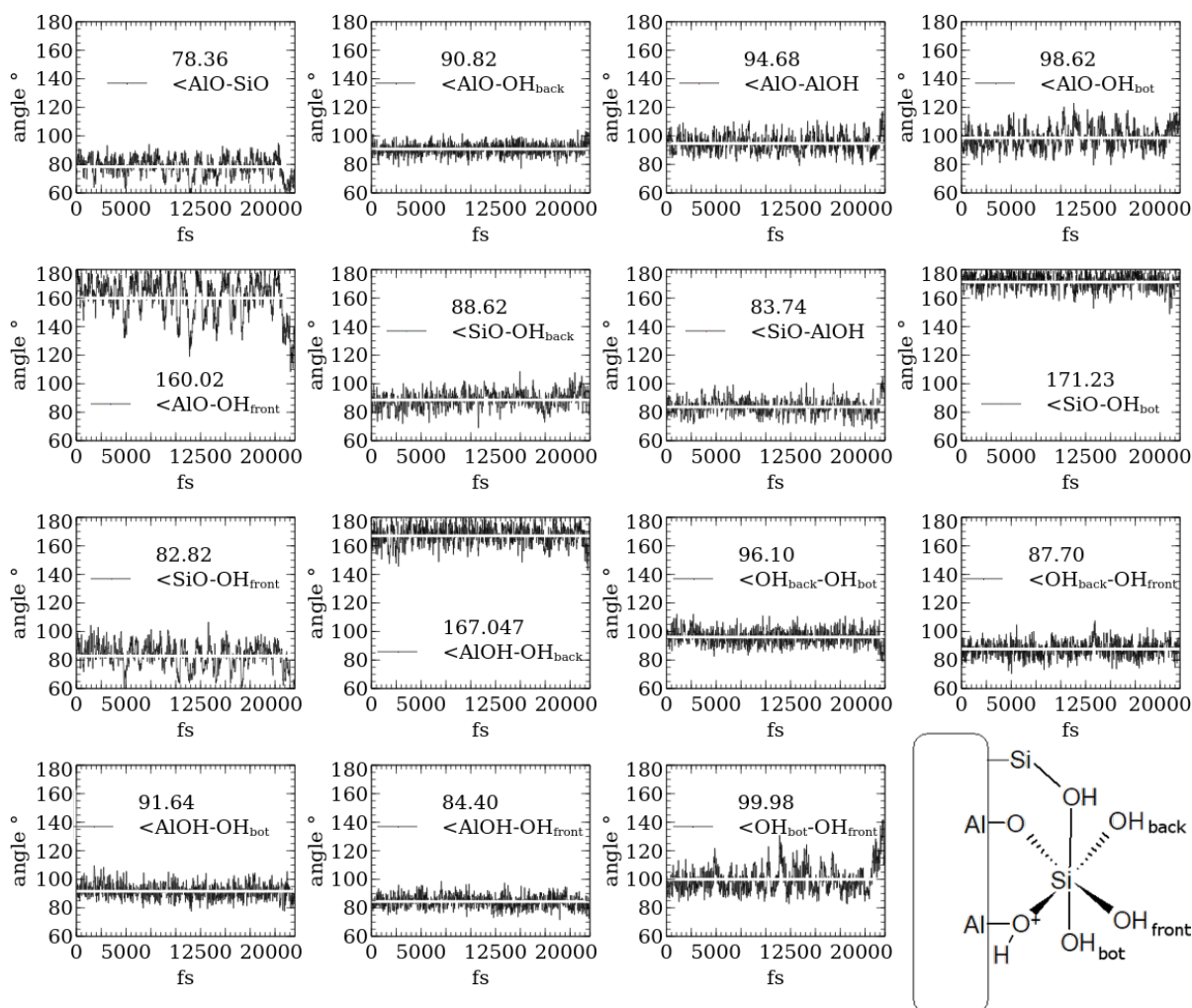


Fig. 4.S6: Angles between the Si-O bonds forming the octahedral configuration at the end of the third step of the Si dissolution (see Fig. 4.7 c and f). All angles are calculated for the whole duration the octahedral coordination is stable, which includes over 20 ps of simulation time. The white line indicates the bond distance average over the whole 20 ps.

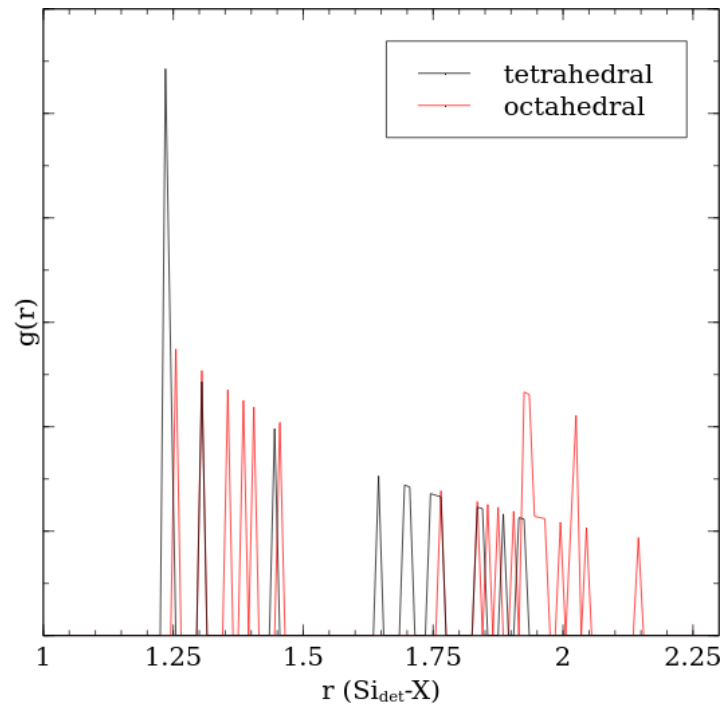


Fig. B7: Radial pair distribution of the detaching Si to the Wannier centers of the highest occupied molecule orbitals with coordinating oxygen. Comparison between the tetrahedral and octahedral coordinated Si.

4.7 References

- Alvarez J. and Rez P. (1998) Electronic structure of stishovite. *Solid State Communications* **108**, 37-42.
- Amram K. and Ganor J. (2005) The combined effect of pH and temperature on smectite dissolution rate under acidic conditions. *Geochimica et Cosmochimica Acta* **69**, 2535-2546.
- Baeyens B. and Bradbury M. (1997) A mechanistic description of Ni and Zn sorption on Na-montmorillonite .1. Titration and sorption measurements. *Journal of Contaminant Hydrology* **27**, 199-222.
- Baeyens B. and Marques Fernandes M. (2018) Adsorption of heavy metals including radionuclides. In *Developments in Clay Science* pp. 125-172.
- Bergaya F. and Vayer M. (1997) CEC of clays: Measurement by adsorption of a copper ethylenediamine complex. *Applied Clay Science* **12**, 275-280.
- Bickmore B., Bosbach D., Hochella M., Charlet L. and Rufe E. (2001) In situ atomic force microscopy study of hectorite and nontronite dissolution: Implications for phyllosilicate edge surface structures and dissolution mechanisms. *American Mineralogist* **86**, 411-423.
- Bickmore B., Rosso K., Nagy K., Cygan R. and Tadanier C. (2003) Ab initio determination of edge surface structures for dioctahedral 2 : 1 phyllosilicates: Implications for acid-base reactivity. *Clays and Clay Minerals* **51**, 359-371.
- Bourg I. C., Sposito G. and Bourg A. C. M. (2007) Modeling cation diffusion in compacted water-saturated sodium bentonite at low ionic strength. *Environmental Science & Technology* **41**, 8118-8122.
- Bourg I., Bourg A. and Sposito G. (2003) Modeling diffusion and adsorption in compacted bentonite: a critical review. *Journal of Contaminant Hydrology* **61**, 293-302.
- Bradbury M. and Baeyens B. (2005) Modelling the sorption of Mn(II), Co(II), Ni(II), Zn(II), Cd(II), Eu(III), Am(III), Sn(IV), Th(IV), Np(V) and U(VI) on montmorillonite: Linear free energy relationships and estimates of surface binding constants for some selected heavy metals and actinides (vol 69, pg 875, 2005). *Geochimica et Cosmochimica Acta* **69**, 5391-5392.
- Bradbury M. H. and Baeyens B. (2011) Predictive sorption modelling of Ni(II), Co(II), Eu(III), Th(IV) and U(VI) on MX-80 bentonite and Opalinus Clay: A “bottom-up” approach. *Applied Clay Science* **52**, 27-33.
- Bussi G., Donadio D. and Parrinello M. (2007) Canonical sampling through velocity rescaling. *Journal of chemical Physics* **126**.
- Churakov S. (2006) Ab initio study of sorption on pyrophyllite: Structure and acidity of the edge sites. *Journal of physical Chemistry B* **110**, 4135-4146.

Churakov S. V. (2007) Structure and dynamics of the water films confined between edges of pyrophyllite: A first principle study. *Geochimica et Cosmochimica Acta* **71**, 1130-1144.

Churakov S. V. and Daehn R. (2012) Zinc Adsorption on Clays Inferred from Atomistic Simulations and EXAFS Spectroscopy. *Environmental Science & Technology* **46**, 5713-5719.

Churakov S. V. and Liu X. (2018) Quantum-chemical modelling of clay mineral surfaces and clay mineral-surface-adsorbate interactions. In *Developments in Clay Science* Developments in Clay Science. pp. 49-87.

Criscenti L., Brantley S., Mueller K., Tsomaia N. and Kubicki J. (2005) Theoretical and Al-27 CPMAS NMR investigation of aluminum coordination changes during aluminosilicate dissolution. *Geochimica et Cosmochimica Acta* **69**, 2205-2220.

Criscenti L., Kubicki J. and Brantley S. (2006) Silicate glass and mineral dissolution: Calculated reaction paths and activation energies for hydrolysis of a Q(3) Si by H₃O⁺ using ab initio methods. *Journal of physical Chemistry A* **110**, 198-206.

Cygan R. T., Liang J.-J. and Kalinichev A. G. (2004) Molecular Models of Hydroxide, Oxyhydroxide, and Clay Phases and the Development of a General Force Field. *The Journal of Physical Chemistry B* **108**, 1255-1266.

Czurda K. (2006) Chapter 11.3 Clay Liners and Waste Disposal. In *Handbook of Clay Science* (ed. B. K. G. T. Faïza Bergaya and G. Lagaly). Handbook of Clay Science. Elsevier. pp. 693-701.

Dähn R., Baeyens B. and Bradbury M. H. (2011) Investigation of the different binding edge sites for Zn on montmorillonite using P-EXAFS - The strong/weak site concept in the 2SPNE SC/CE sorption model. *Geochimica et Cosmochimica Acta* **75**, 5154-5168.

Dähn R., Scheidegger A., Manceau A., Curti E., Baeyens B., Bradbury M. and Chateigner D. (2002) Th uptake on montmorillonite: A powder and polarized extended X-ray absorption fine structure (EXAFS) study. *Journal of Colloid and Interface Science* **249**, 8-21.

Dähn R., Scheidegger A., Manceau A., Schlegel M., Baeyens B., Bradbury M. and Chateigner D. (2003) Structural evidence for the sorption of Ni(II) atoms on the edges of montmorillonite clay minerals: A polarized X-ray absorption fine structure study. *Geochimica et Cosmochimica Acta* **67**, 1-15.

Dähn R., Scheidegger A., Manceau A., Schlegel M., Baeyens B., Bradbury M. and Morales M. (2002a) Neoformation of Ni phyllosilicate upon Ni uptake on montmorillonite: A kinetics study by powder and polarized extended X-ray absorption fine structure spectroscopy. *Geochimica et Cosmochimica Acta* **66**, 2335-2347.

Delhorme M., Labbez C., Caillet C. and Thomas F. (2010) Acid-Base Properties of 2:1 Clays. I. Modeling the Role of Electrostatics. *Langmuir* **26**, 9240-9249.

Dohrmann R., Genske D., Karnland O., Kaufhold S., Kiviranta L., Olsson S., Ploetze M., Sanden T., Sellin P., Svensson D. and Valter M. (2012) Interlaboratory CEC and exchangeable Cation

Study of Bentonite Buffer Materials: I. Cu(II)-Triethylenetetramine Method. *Clays and Clay Minerals* **60**, 162-175.

Dohrmann R., Genske D., Karnland O., Kaufhold S., Kiviranta L., Olsson S., Ploetze M., Sanden T., Sellin P., Svensson D. and Valter M. (2012a) Interlaboratory CEC and exchangeable Cation Study of Bentonite Buffer Materials: II. Alternative Methods. *Clays and Clay Minerals* **60**, 176-185.

Dohrmann R., Olsson S., Kaufhold S. and Sellin P. (2013) Mineralogical investigations of the first package of the alternative buffer material test - II. Exchangeable cation population rearrangement. *Clay Minerals* **48**, 215-233.

ed. Brantley S. L., Kubicki J. D. and White A. F. (2007) *Kinetics of Water-Rock Interaction.*, Springer New York

Gaucher E. C. and Blanc P. (2006) Cement/clay interactions - A review: Experiments, natural analogues, and modeling. *Waste Management* **26**, 776-788.

Goedecker S., Teter M. and Hutter J. (1996) Separable dual-space Gaussian pseudopotentials. *Physical Review B* **54**, 1703-1710.

Grim R. E. and Company M.-H. P. (1968) *Clay Mineralogy.*, McGraw-Hill.

Grimme S. (2004) Accurate description of van der Waals complexes by density functional theory including empirical corrections. *Journal of computational Chemistry* **25**, 1463-1473.

Iannuzzi M., Laio A. and Parrinello M. (2003) Efficient exploration of reactive potential energy surfaces using Car-Parrinello molecular dynamics. *Physical Review Letters* **90**.

Kahr G. and Madsen F. T. (1995) Determination of the cation exchange capacity and the surface area of bentonite, illite and kaolinite by methylene blue adsorption. *Applied Clay Science* **9**, 327-336.

Kahr G. and Madsen F. T. (1995) Determination of the cation exchange capacity and the surface area of bentonite, illite and kaolinite by methylene blue adsorption. *Applied Clay Science* **9**, 327-336.

Kaufhold S., Dohrmann R., Sanden T., Sellin P. and Svensson D. (2013) Mineralogical investigations of the first package of the alternative buffer material test - I. Alteration of bentonites. *Clay Minerals* **48**, 199-213.

Kéri A., Dahn R., Krack M. and Churakov S. V. (2017) Combined XAFS Spectroscopy and Ab Initio Study on the Characterization of Iron Incorporation by Montmorillonite. *Environmental Science & Technology* **51**, 10585-10594.

Kéri A., Dahn R., Krack M. and Churakov S. V. (2019) Characterization of Structural Iron in Smectites - An Ab Initio Based X-ray Absorption Spectroscopy Study. *Environmental Science & Technology* **53**, 6877-6886.

Kéri A., Dahn R., Marques Fernandes M., Scheinost A. C., Krack M. and Churakov S. V. (2020) Iron adsorption on clays inferred from atomistic simulations and XAS studies. *Environmental Science & Technology*

Kraevsky V S., Tournassat C., Vayer M., Warmont F., Grangeon S., Wakou B. F. N. and Kalinichev A. G. (2020) Identification of montmorillonite particle edge orientations by atomic-force microscopy. *Applied Clay Science* **186**.

Laio A. and Parrinello M. (2002) Escaping free-energy minima. *Proceedings of the national Academy of Sciences of the United States of America* **99**, 12562-12566.

Liu X., Cheng J., Sprik M., Lu X. and Wang R. (2014) Surface acidity of 2:1-type dioctahedral clay minerals from first principles molecular dynamics simulations. *Geochimica et Cosmochimica Acta* **140**, 410-417.

Liu X., Lu X., Cheng J., Sprik M. and Wang R. (2015) Temperature dependence of interfacial structures and acidity of clay edge surfaces. *Geochimica et Cosmochimica Acta* **160**, 91-99.

Liu X., Lu X., Meijer E. J., Wang R. and Zhou H. (2012) Atomic-scale structures of interfaces between phyllosilicate edges and water. *Geochimica et Cosmochimica Acta* **81**, 56-68.

Liu X., Lu X., Sprik M., Cheng J., Meijer E. J. and Wang R. (2013) Acidity of edge surface sites of montmorillonite and kaolinite. *Geochimica et Cosmochimica Acta* **117**, 180-190.

Lyon R. (1962) Infra-red Confirmation of 6-fold coordination of Silicon in Stishovite. *Nature* **196**.

Macht F., Eusterhues K., Pronk G. J. and Totsche K. U. (2011) Specific surface area of clay minerals: Comparison between atomic force microscopy measurements and bulk-gas (N₂) and -liquid (EGME) adsorption methods. *Applied Clay Science* **53**, 20-26.

Manceau A., Marcus M., Tamura N., Proux O., Geoffroy N. and Lanson B. (2004) Natural speciation of Zn at the micrometer scale in a clayey soil using X-ray fluorescence, absorption, and diffraction. *Geochimica et Cosmochimica Acta* **68**, 2467-2483.

Marques Fernandes M., Baeyens B., Daehn R., Scheinost A. C. and Bradbury M. H. (2012) U(VI) sorption on montmorillonite in the absence and presence of carbonate: A macroscopic and microscopic study. *Geochimica et Cosmochimica Acta* **93**, 262-277.

Marques Fernandes M., Ver N. and Baeyens B. (2015) Predicting the uptake of Cs, Co, Ni, Eu, Th and U on argillaceous rocks using sorption models for illite. *Applied Geochemistry* **59**, 189-199.

Marty N. C. M., Cama J., Sato T., Chino D., Villieras F., Razafitianamaharavo A., Brendle J., Giffaut E., Soler J. M., Gaucher E. C. and Tournassat C. (2011) Dissolution kinetics of synthetic Na-smectite. An integrated experimental approach. *Geochimica et Cosmochimica Acta* **75**, 5849-5864.

- Marty N. C. M., Tournassat C., Burnol A., Giffaut E. and Gaucher E. C. (2009) Influence of reaction kinetics and mesh refinement on the numerical modelling of concrete/clay interactions. *Journal of Hydrology* **364**, 58–72.
- Meier L. and Kahr G. (1999) Determination of the cation exchange capacity (CEC) of clay minerals using the complexes of copper(II) ion with triethylenetetramine and tetraethylenepentamine. *Clays and Clay Minerals* **47**, 386–388.
- Metz V., Amram K. and Ganor J. (2005) Stoichiometry of smectite dissolution reaction. *Geochimica et Cosmochimica Acta* **69**, 1755–1772.
- Meunier A. (2005) *Clays*. 1 ed., Springer-Verlag Berlin Heidelberg.
- Nomura K., Kalia R. K., Nakano A., Vashishta P. and van Duin A. C. T. (2012) Mechanochemistry of shock-induced nanobubble collapse near silica in water. *Applied Physics Letters* **101**.
- Oelkers E. H., Schott J., Gauthier J.-M. and Herrero-Roncal T. (2008) An experimental study of the dissolution mechanism and rates of muscovite. *Geochimica et Cosmochimica Acta* **72**, 4948–4961.
- Ono S., Kikegawa T., Higo Y. and Tange Y. (2017) Precise determination of the phase boundary between coesite and stishovite in SiO₂. *Physics of the Earth and planetary Interiors* **264**, 1–6.
- Pelmenschikov A., Leszczynski J. and Pettersson L. (2001) Mechanism of dissolution of neutral silica surfaces: Including effect of self-healing. *Journal of physical Chemistry A* **105**, 9528–9532.
- Pelmenschikov A., Strandh H., Pettersson L. and Leszczynski J. (2000) Lattice resistance to hydrolysis of Si-O-Si bonds of silicate minerals: Ab initio calculations of a single water attack onto the (001) and (111) beta-cristobalite surfaces. *Journal of Physical Chemistry B* **104**, 5779–5783.
- Perdew J., Burke K. and Ernzerhof M. (1996) Generalized gradient approximation made simple. *Physical Review Letters* **77**, 3865–3868.
- Pfeiffer-Laplaud M., Gaigeot M.-P. and Sulpizi M. (2016) pK(a) at Quartz/Electrolyte Interfaces. *Journal of Physical Chemistry Letters* **7**, 3229–3234.
- Pusch R. (2006) Chapter 6 Mechanical Properties of Clays and Clay Minerals. In *Handbook of Clay Science* (ed. B. K. G. T. Faïza Bergaya and G. Lagaly). Handbook of Clay Science. Elsevier. pp. 247–260.
- Robin V., Tertre E., Regnault O. and Descostes M. (2016) Dissolution of beidellite in acidic solutions: Ion exchange reactions and effect of crystal chemistry on smectite reactivity. *Geochimica et Cosmochimica Acta* **180**, 97–108.
- Schlegel M. and Manceau A. (2006) Evidence for the nucleation and epitaxial growth of Zn phyllosilicate on montmorillonite. *Geochimica et Cosmochimica Acta* **70**, 901–917.

Schlegel M., Manceau A., Charlet L., Chateigner D. and Hazemann J. (2001) Sorption of metal ions on clay minerals. III. Nucleation and epitaxial growth of Zn phyllosilicate on the edges of hectorite. *Geochimica et Cosmochimica Acta* **65**, 4155-4170.

Schliemann R. and Churakov V S. (2021) Atomic scale mechanism of clay minerals dissolution revealed by ab initio simulations. *Geochimica et Cosmochimica Acta* **293**, 438-460.

Shekhar A., Nomura K.-i., Kalia R. K., Nakano A. and Vashishta P. (2013) Nanobubble Collapse on a Silica Surface in Water: Billion-Atom Reactive Molecular Dynamics Simulations. *Physical Review Letters* **111**, 184503-1-184503-5.

Slabaugh W. (1954) Cation Exchange Properties of Bentonite. *Journal of physical Chemistry* **58**, 162-165.

Soltermann D., Marques Fernandes M., Baeyens B., Daehn R., Mieke-Brendle J., Wehrli B. and Bradbury M. H. (2013) Fe(II) Sorption on a Synthetic Montmorillonite. A Combined Macroscopic and Spectroscopic Study. *Environmental Science & Technology* **47**, 6978-6986.

Soltermann D., Marques Fernandes M., Baeyens B., Mieke-Brendle J. and Daehn R. (2014) Competitive Fe(II)-Zn(II) Uptake on a Synthetic Montmorillonite. *Environmental Science & Technology* **48**, 190-198.

Tournassat C., Davis J. A., Chiaberge C., Grangeon S. and Bourg I. C. (2016) Modeling the Acid-Base Properties of Montmorillonite Edge Surfaces. *Environmental Science & Technology* **50**, 13436-13445.

Tournassat C., Grangeon S., Leroy P. and Giffaut E. (2013) Modeling specific pH dependent sorption of divalent metals on montmorillonite surfaces. A review of pitfalls, recent achievements and current challenges. *American Journal of Science* **313**, 395-451.

Tournassat C., Neaman A., Villieras F., Bosbach D. and Charlet L. (2003) Nanomorphology of montmorillonite particles: Estimation of the clay edge sorption site density by low-pressure gas adsorption and AFM observations. *American Mineralogist* **88**, 1989-1995.

Tournassat C., Tinnacher R. M., Grangeon S. and Davis J. A. (2018) Modeling uranium(VI) adsorption onto montmorillonite under varying carbonate concentrations: A surface complexation model accounting for the spillover effect on surface potential. *Geochimica et Cosmochimica Acta* **220**, 291-308.

Walther J. (1996) Relation between rates of aluminosilicate mineral dissolution, pH, temperature, and surface charge. *American Journal of Science* **296**, 693-728.

Wick S., Baeyens B., Fernandes M. M. and Voegelin A. (2018) Thallium Adsorption onto Illite. *Environmental Science & Technology* **52**, 571-580.

Xiao Y. and Lasaga A. (1994) Ab-initio quantum-mechanical studies of the kinetics and mechanisms of silicate dissolution - H⁺(H₃O⁺) catalysis. *Geochimica et Cosmochimica Acta* **58**, 5379-5400.

Xiao Y. and Lasaga A. (1996) Ab initio quantum mechanical studies of the kinetics and mechanisms of quartz dissolution: OH- catalysis. *Geochimica et Cosmochimica Acta* **60**, 2283-2295.

Zhang C., Liu X., Lu X. and He M. (2018) Complexation of heavy metal cations on clay edges at elevated temperatures. *Chemical Geology* **479**, 36-46.

Zheng Y.-F. and Chen R.-X. (2017) Regional metamorphism at extreme conditions: Implications for orogeny at convergent plate margins. *Journal of Asian Earth Sciences* **145**, 46–73.

5. High pressure dissolution mechanism of Pyrophyllite from the (110) edge

Most of the text of this chapter is published as part of the book chapter:

“Churakov, S.; Schliemann, R.; (2021) Ab initio simulations of clay minerals reactivity and thermodynamics, in C.I. Sainz-Díaz (Editor). Computational Modelling in Clay Mineralogy, AIPEA Educational Series, Pub. No. 3, Chapter 6, Digilabs, Bari, Italy.”

5.1 Introduction

The dissolution mechanism of the (110) edge surface of pyrophyllite at ambient conditions was recently investigated by (Schliemann and Churakov 2021) using the MetaD simulation approach. The obtained MetaD simulation trajectories demonstrate that leaching of cations in tetrahedral and octahedral surface sites take place as a complex sequence of reaction events with several reaction intermediates. In general, each elementary reaction step modifies the surface-denticity of the reacting site, and eventually enables the leaching of octahedral or tetrahedral ions from the edge surface. The detailed analysis of the reaction mechanism reveals that the solvent rearrangement and the proton transfer reactions in the first and the second coordination shell of the dissolving unit play a critical role in the stabilization of reaction intermediates and the net progress of the dissolution reactions. Each intermediate reaction event is typically triggered by a nucleophilic attack of H₂O molecules or OH groups on the dissolving surface site followed by ligand exchange reactions in the first coordination shell of the reacting sites. These events change the conformation and denticity of reacting site at the mineral surface. The reaction products are further stabilised by collective proton transfer reactions between the acidic and basic oxygen sites mediated via a chain of the hydrogen bonded molecules in the first and the second coordination shell of the reacting site. Analysis of the activation barriers for different surface sites suggest that detachment of the terminal aluminol group in the octahedral sheet has significantly lower activation barriers than the corresponding barriers for the terminal silanol groups. This is consistent with the stronger energy of ion-covalent Si-O bond compared to the ionic Me-O interaction and further supported by experimental observation of the initial preferential leaching of the octahedral ions on the surface of phyllosilicate minerals.

Following the simulations of Pyrophyllite dissolution for (110) (Schliemann and Churakov 2021a) and (010) (Schliemann and Churakov 2021b) edge surfaces in our previous studies, this study was aimed to estimate simulation uncertainties related to the sampling of the potential energy surface. Specifically, the influence of initial system configuration on the dissolution mechanism was investigated. This complementary study also shows the effect of elevated water density on the dissolution mechanism of clay minerals.

5.2 System and simulation setup

The simulation system was represented by one TOT-layer of pyrophyllite with (110) edge surfaces built on the basis of an ideal structure. A slit pore between (110) edge surfaces was filled with water molecules to represent the interface with bulk water. 3D periodic boundary conditions were applied throughout the simulations. The initial system dimension between the TOT layers was set to 10 Å. The independent simulations were performed using supercells with two unit cells in [100] crystallographic direction of pyrophyllite corresponding to (10.4

Å). The size of the slit pore was adjusted to accommodate a necessary amount of water molecules (60 to 120 molecules) between the edge surfaces, so that the fluid in the center of the pore resembles bulk water properties. The scoping calculations and pre-equilibration of the system were performed with classical simulation as described in the next paragraph. The supercell dimension in direction normal to the interface was 39.3 Å to 42.1 Å, depending on the administered water density.

Prior to the ab initio equilibration and production MD runs, the distribution of water molecules in the slit pore was pre-equilibrated in NVT ensemble (constant Volume, Temperature and Number of particles) at 300K for at least 1 ns using the CLAYFF force field (Cygan et al., 2004) keeping the atomic positions of the clay particle frozen at their equilibrium position obtained by ab initio geometry optimization. This classical pre-equilibration runs were used to adjust the box size in b(y)-direction adjusting number of water molecules in the system until water-like density in the middle of the water layer was obtained. Further detail of the simulation setup is provided in the Supporting Information. The obtained molecular configuration was used as initial conditions for actual equilibration of the system by the ab initio simulations described in Chapter 2.

5.3 Results

The following section provides new insight into the mechanism of Al leaching from octahedral sheet of pyrophyllite at high pressure conditions corresponding to ~1.6 GPa. This system can be considered as limiting case for the reactivity of phyllosilicates (e.g. mica minerals) in high pressure metamorphic rocks of Alpine and Barrovian facies series (Zheng and Chen 2017). The MetaD simulations setup and reaction coordinates are used as described in (Schliemann and Churakov 2021), except for the high pressure conditions. The results described in detail in the following section show that also under high-pressure conditions, the main steps of the aluminol detachment mechanism are very similar to those controlling the dissolution under ambient conditions.

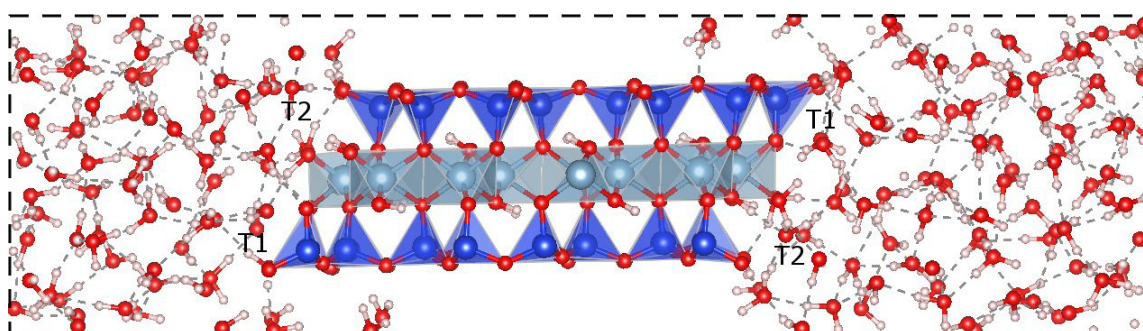
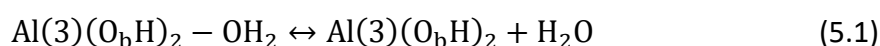


Figure 5.1: A snapshot of the simulation supercell shown in sideview. The two symmetrically inequivalent silanol groups are indicated with T1 and T2.

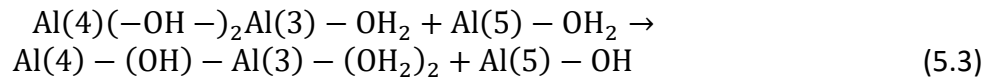
The first reaction step on the minimum energy pathway towards dissolution is the detachment of the O(i)H₂ group (see Fig. 5.2), leaving the initially octahedral coordinated Al surface site in five-fold coordination. This H₂O desorption/resorption is reversible and is encountered in the modelling trajectory for several times:



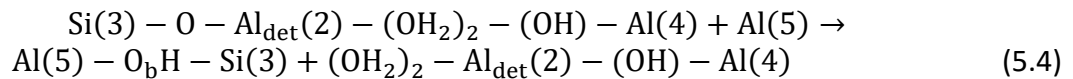
The repetitive desorption and resorption of H₂O leads to destabilization of the surface structure. Fig. 5.3 schematically shows the deformation of Al(o) coordination caused by the displacement of the Al(o) and the rupture of two Al – O_b bonds connecting neighbouring Al octahedral (see O(v) and O(vi) in Fig. 5.3). The Al(o) becomes coordinated with three O_b, that are bonded to one Al(o), the two Si(t) (Si_{T1} and Si_{T2}) and one OH₂-group:



Shortly after the reaction in Eq. 5.2, the OH₂(vii) group is donating a proton to the O_b(v) bridging site and the Al becomes coordinated by three O_b and two OH₂ groups (see Fig. 5.4, Eq. 28).



In the next series of steps water molecules at the interface repeatedly enter and leave the hydration shell of the Al site changing its coordination number of this site between four and five without a crossing a barrier on the minimum energy pathway to the aluminol detachment. These fluctuations in the coordination shell cause elongation of the Al–OH(ii) bond in the octahedral sheet.

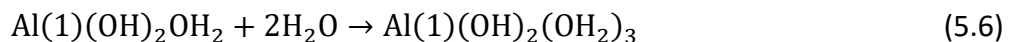


Eventually, the Al–OH bond breaks and the Al site moves away from the lower tetrahedral sheet (Si_{T2}) and forms a bond to a nearby H₂O molecule (Fig. 5.5). As the result, Al forms a bi-dentate complex simultaneously attached to the upper and to the lower tetrahedral sheet via bridging O_b-Si sites and hydrated by a water molecule and an OH group.

In the upcoming step the remaining Al – O_b bond to the octahedral sheet breaks, leading to a monodentate complex with tetrahedral Al coordination on the surface (Fig. 5.6). In the same time two protons from two different OH₂ groups dissociate into the slit pore. That can be written as follows:



In the follow-up reaction of the trajectory 2 more water molecules one by one enter the coordination shell of the detaching aluminol (see Fig. 5.7 and 5.8, respectively), leading to an octahedral coordinated monodentate complex. The reaction can be summarized as:



In the final reaction step of (Al–O_b)-Si bond elongates and initially six-fold mono-dentate complex detach from the Si–O_b site (Eq. 5.7, Fig. 5.9). During the transition, two H₂O molecules in the solvation shell of the complex deprotonate. One of them donate the proton to the dangling Si–O_b bond. Another proton is transferred to O(ii) site. The deprotonating H₂O molecule and the proton accepting surface site are spatially separated and do not have direct hydrogen bonded interaction. The net proton exchange between the proton donor and acceptor takes place via collective motion of protons along a chain of hydrogen bonds formed

by several water molecules at the interface. The neo-formed tetrahedral coordinated oxyion $\text{Al}(\text{OH})_4$ remains close to the interface forming hydrogen bonds to the surface oxygen sites. At the later stage, the $\text{Al}(\text{OH})_4$ desorbs from the surface and diffuse into the inter particle space.

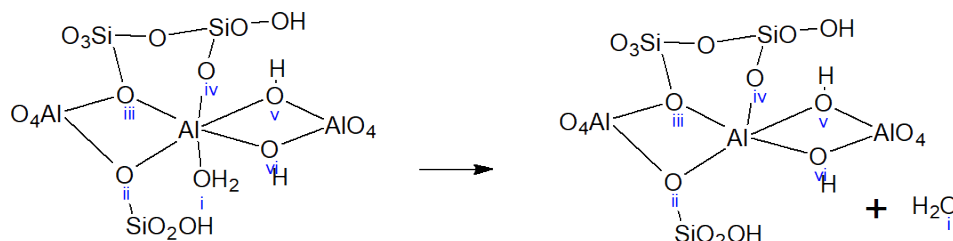
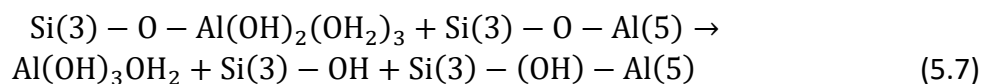


Figure 5.2. Reversible detachment of the OH_2 group from the octahedral Al species. This reaction step (Eq. 26) leads to dynamic destabilisation Al octahedra and precondition further reaction event.

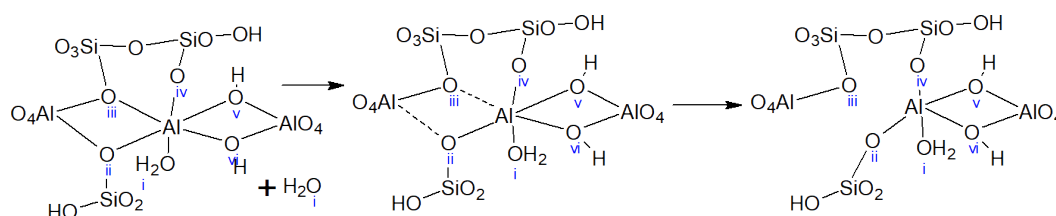


Figure 5.3. Schematic structural representation of reactant and product in Eq. 27. Two $\text{Al} - \text{O}_b$ bonds to trifold coordinated O_b break and the Al coordination collapses into fivefold coordination.

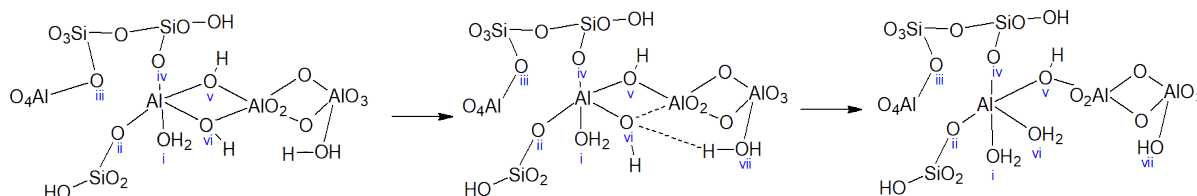


Figure 5.4. In this reaction step, the $\text{O}(\text{vii})\text{H}_2$ group of a nearby $\text{Al}(\text{O})$ donates one proton to the $\text{O}_b\text{H}(\text{vi})$ site, which then breaks its bond to the connected Al. The resulting complex has three oxygen bridges to the surface and two OH_2 (i and vi) groups (see Eq. 5.3).

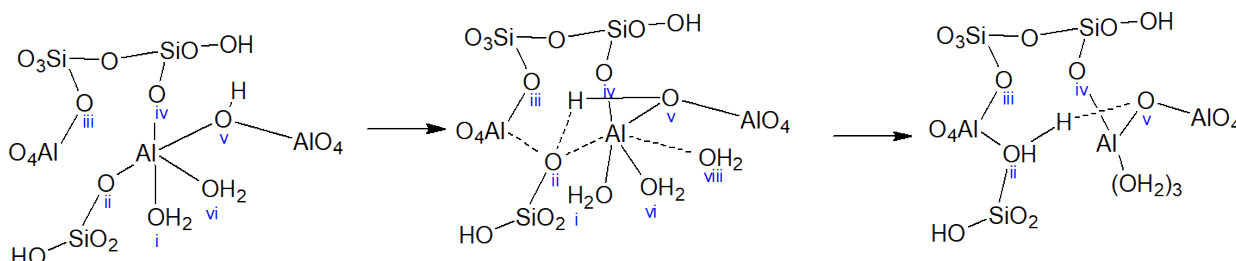


Figure 5.5. Nucleophilic attack of a water molecule result in the rupture of the $\text{Al}-\text{O}_b(\text{ii})$ bond and rebinds to the nearby $\text{Al}(\text{O})$ (see Eq. 29). The Al forms a bidentate complex attached to upper tetrahedral and the octahedral sheet.

The activation barriers obtained for the intermediate reaction steps are listed in Table 5.1. Although the sequence of reaction intermediates is not identical, the predicted activation energies are in the same range as the ones observed at ambient conditions (Schliemann and Churakov 2021). The activation barriers seem to be mainly dependent on the structural environment of the detaching species.

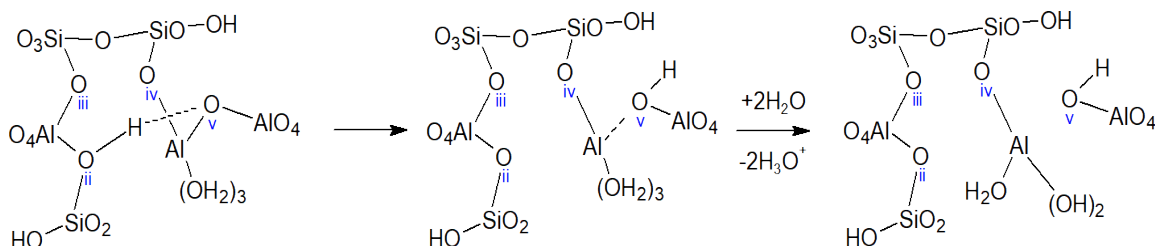


Figure 5.6. Water molecule enters the hydration shell of the Al and changes the CN from four to five (see Eq. 30). Simultaneously, Al_{det} changes its conformation on surface by swapping one of the bonds in the di-dentate complex from the oxygen in the tetrahedral to the octahedral sheet.

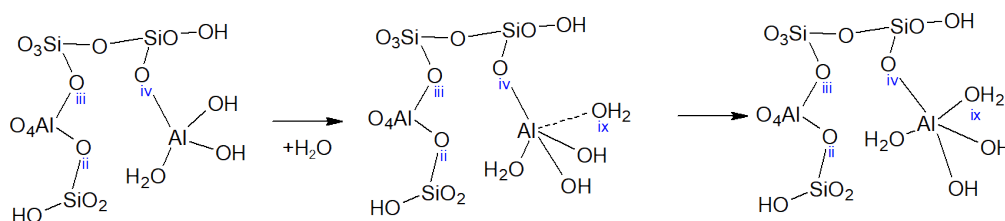


Figure 5.7: The $\text{H}_2\text{O}(\text{ix})$ water molecules enters coordination shell of detaching $\text{Al}(\text{o})$ and result in formation of fivefold coordinated mono-dentate complex.

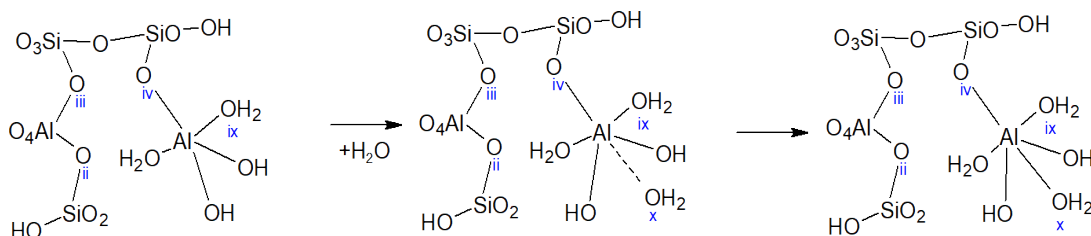


Figure 5.8: Another water molecule bonds to the monodentate Al species, completing the six-fold coordination. The reaction is comparable to the one shown in Fig. 16.

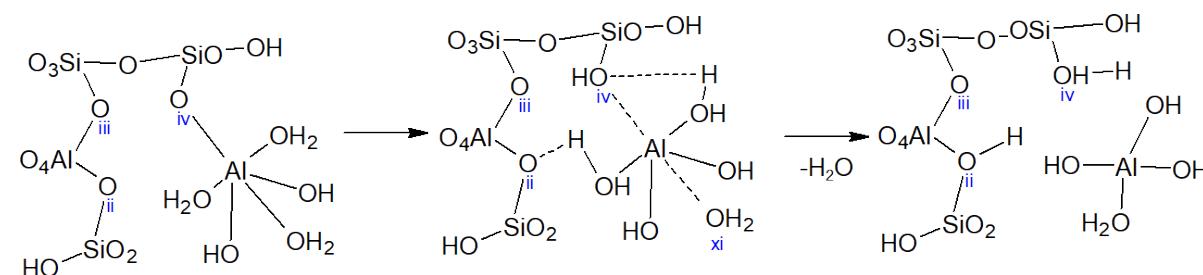


Figure 5.9: The final reaction step of leaching process, in which the Al-mono-dentate complex detach from the surface. In this step the protons in the coordination shell of the detaching Al site get rearranges in such a way, that one proton is accepted by the bridging oxygen O(iv) and another one by the nearby O(ii). The first leads to the completion of detachment from the surface and because of the dissociation of one $\text{O}(\text{xi})\text{H}_2$ group, the product is $\text{Al}(\text{OH})_4$ (compare Eq. 5.7).

Table 5.1: Estimated activation energies (kJ/mol) of the intermediate reaction steps of aluminol detachment from the (110) edge surface of pyrophyllite corresponding to equations 5.1-5.7.

Al _{MEP2}	Equations	5.1	5.2 & 5.3	5.4	5.5	5.6	5.7
	E _A	31.4	94.1	66.6	34.6	17.1	69.3

5.4 Conclusion

The simulations at elevated pressure presented in this chapter showed variability of the elementary reaction events already observed in our previous publications (Schliemann and Churakov 2021a, 2021b). The step-by-step mechanism of the pyrophyllite octahedral sheet dissolution was observed here as well. It starts with a nucleophilic agent attacking the detaching octahedral site, the ligand exchange progresses by proton transfer through a chain of water and hydroxy-groups and finally a bond break. This cycle repeats until all bonds to the surface are broken and the detaching aluminol group is solvated.

The activation barriers observed with the Metadynamics were very similar to the barriers observed at ambient conditions. However, the number of steps for the detachment of one Al site from the pyrophyllite is apparently higher with the initial system configuration in this study.

5.5 References

- Cygan R. T., Liang J.-J. and Kalinichev A. G. (2004) Molecular Models of Hydroxide, Oxyhydroxide, and Clay Phases and the Development of a General Force Field. *The Journal of Physical Chemistry B* **108**, 1255–1266.
- Schliemann R. and Churakov V S. (2021a) Atomic scale mechanism of clay minerals dissolution revealed by ab initio simulations. *Geochimica et Cosmochimica Acta* **293**, 438–460.
- Schliemann R. and Churakov V S. (2021b) Pyrophyllite dissolution at elevated pressure conditions: An ab initio study. *Geochimica et Cosmochimica Acta* **307**, 42–55.
- Zheng Y.-F. and Chen R.-X. (2017) Regional metamorphism at extreme conditions: Implications for orogeny at convergent plate margins. *Journal of Asian Earth Sciences* **145**, 46–73.

6. Conclusion and Outlook

The main scientific outcome of this thesis is the atomic scale mechanistic understanding of the dissolution processes at the edges of phyllosilicate minerals in aqueous solution. This includes detailed description of the elementary reaction steps and corresponding energies of activation barriers leading to the net leaching of aluminol and silanol species from the octahedral and tetrahedral sheets of pyrophyllite in water close to neutral pH. Considering structurally distinct edge surfaces, we could show that the fundamental elementary reaction steps controlling the overall detachment event of either species (Al(O) or Si(T)) are universal and generally applicable to different structural environments and geochemical conditions. On the other hand, the exact sequence of the elementary reaction steps is strongly dependent on the structural environment (density) and the speciation of the detaching site (chapters 3 to 5). The leaching of polydentate complexes can be considered as a sequence of reaction events leading to a step-by-step decrease of surface complex density (see Fig. 6.1). The general mechanism of each elementary reaction step can be described as follows: A nucleophilic agent, either a water molecule or a nearby OH_x group, enters the first coordination shell of the detaching species (Fig. 6.1a). This step is referred to as a nucleophilic attack which is a necessary precursor for the ligand exchange reaction. The ligand exchange reaction and the rupture of metal oxygen bonds initially coordinating the surface complex, result in the formation of highly dangling oxygen sites with unsaturated valences (Fig. 6.1c). These oxygen sites are prone to accept protons from more acidic functional groups. The proton donors can be neighbouring groups like >MOH_x (M= Si, Al) (like in Fig. 6.1c), but other more distant donors are possible. The observed size of the hydrogen bond chain included up to 7 molecules and/or terminal groups. In this case, the net proton transport from donor to acceptor is facilitated by collective motion of protons along a hydrogen bond chain consisting of H₂O and OH groups. This sequence (Fig. 6.1 a - d) is repeated until all oxygen bridges to the surface are broken and the species detaches with its hydration shell into the bulk water. The identified elementary reaction steps and overall reaction mechanism involving solvent exchange and proton transfer reaction are general and thus should be applicable to other clay minerals and even aluminosilicates with a similar bond structure. It can be argued that the variation in chemistry and accordingly the strength of the cation-oxygen bond should have an influence on the energy of the activation barrier but not the qualitative nature of the reaction mechanism.

As one of the first metadynamics studies on geochemical systems with a distinct consideration of water molecules it is therefore also a proof of concept for other mineral-water interface studies on reactions at the atomistic scale. It has been widely applied to smaller systems before, with system size restrictions mainly due to the limitations of computational resources. Nowadays with advances in numerical methods and highly parallelizable algorithms as well as the easy access to supercomputer facilities the calculation efforts for the investigation of bigger systems are feasible. In fact, another recent study used the same methodology and found very similar elementary reaction steps for tricalcium silicate dissolution (Li et.al, 2022), even though the collective variables used differ from this study. One of the main reasons for the need of the computational resources or the lack of accuracy in smaller systems is the equilibration of water, which requires a certain amount of water molecules to correctly represent its dynamics.

The differences in all three simulation setups in chapters 3 to 5 can be seen in the intermediate states that show distinct denticities (number of bonds to the edge surface) of the detaching species, depending on the accessibility for nucleophilic species to the site. For a detaching Si site an octahedral coordination is observed in the intermediate state of the detachment reaction. The Al site can undergo a tetrahedral coordination. The lifetime and concentration of these structural complexes is in the order of few picoseconds and thus cannot be detected by conventional spectroscopic methods. An explanation for the occurrence of the octahedral coordination of Si might be the highly ordered structure of the water molecules near the edge surface under the defined water pressure conditions in chapter 4.

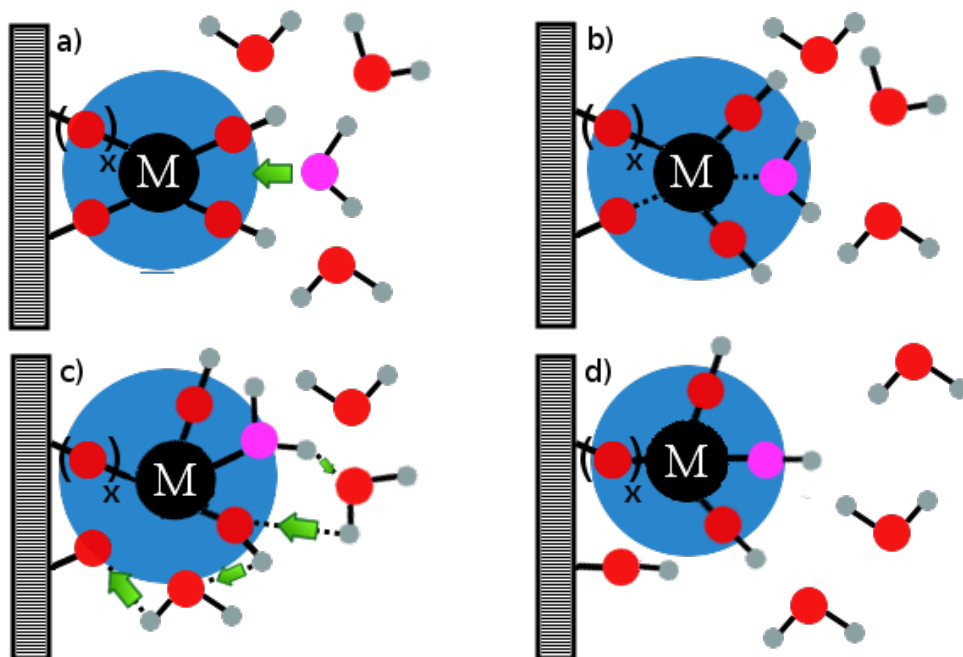


Fig. 6.1: Elementary reaction steps controlling the cation leaching from the clay mineral surface. a) nucleophilic attack of a water molecule on a surface site leading to local increase of coordination number b) breaking of a surface bond and subsequent solvent rearrangement c) ligand exchange with the proton transfer through a chain of water molecules in the first and second coordination shell shown with the green arrows and d) formation of surface complex (M) with reduced denticity. Repeating the steps a) to d) eventually leads to detachment of the species M and its release into solution. The red and purple spheres are oxygen atoms, the small grey spheres represent the hydrogen atoms and the blue circle marks the hydration shell of the metal ion.

The calculated activation barriers describe individual reaction steps in an idealised environment. The surface roughness and local structural heterogeneities would lead to co-existence of various mineral surface terminations and surface species. Thus, in natural environment, several concurrent reactions contribute to the overall reaction flux measured by macroscopic reactions. To link macroscopic reactive reaction rates with the theoretical predictions, the calculated activation barriers can be included in kinetic models in comparison to sorption, incorporation and mineral growth reactions. This way, the temporal evolution of clay minerals in different solutions can be studied and evaluated. The activation energies on their own already suggest that the Al species are more prone to the leaching over the Si

species in pH-neutral water at least in the initial stage of the dissolution. Whereas at steady state the dissolution is expected to be congruent. As more and more of the octahedral sites leach, the lower the probability of a nucleophilic attack on the remaining octahedral sites. Since the tetrahedral sheets surround the cavities emerging from leached octahedral ions, the attack of nucleophilic agents on further octahedral sites is sterically hindered. This would eventually lead to close to stoichiometric Al/Si ratio and a congruent steady state dissolution. This has been confirmed by a number of experimental studies (Amram and Ganor 2005, Cappelli et al. 2018, Metz et al. 2005).

The simulation condition corresponds to the neutral pH. Most of the experimental studies are conducted either at acidic (Bosbach et al. 2000, Cappelli et al. 2018, Metz et al. 2005, Oelkers et al. 2008) or basic (Kuwahara 2008, Oelkers et al. 2008) conditions. Only a few experimental studies were done at neutral pH or in a range covering acidic to basic pH (Golubev et al. 2006, Marty et al. 2011).

The acidic or basic pH influences the proton activity and availability of more nucleophilic OH⁻ groups and thus have an impact on the reactivity of the clay species. Acidic conditions lead to activated complexes at the clays surfaces due to a higher possibility of protonated terminal oxygen groups. This changes the activation energies needed to dissolve the species and represents another setup that could be thoroughly investigated by ab initio simulations. In basic conditions the surplus of hydroxy ions lead to deprotonated sites at the edge surfaces, which again might change the activation barriers for the detachment of the terminal sites. In order to simulate the detachment of those protonated/deprotonated edge surfaces of the clay mineral, the initial surface structure exposed to solutions with different pH and ion activity needs to be known. A way to simulate that would be the grand canonical Monte Carlo method (Labbez and Jönsson 2007, Delhorme et al. 2010). With that initial surface structure, the influence of the pH on the activation barriers of the dissolution steps can be investigated. Further, it is possible that the interlayer ions in some types of clay minerals are influencing the activation barriers for reaction steps of nearby tetrahedral and octahedral species.

The differences of clays regarding their composition and origin as well as auxiliary phases add another level of complexity to the calculation of their reaction rates. In addition, interstratified clay minerals having differently stacked structural layers will also have influence on the reactivity of the involved species. Hence, in order to get a full understanding of the dissolution mechanism and reaction rates for the whole variety of 2:1 clay minerals further studies need to be done. Even if the elementary reaction steps might be comparable, the activation barriers of Al(O)/Si(T) in contrast to Mg(O), Fe(II)(O)/Al(T), Fe(III)(T) or other isomorphic substitutions and the local dependency on the nearest neighbours, could be different. Isomorphic substitutions in octahedral and tetrahedral sites are likely to increase the activation barriers, due to their additional attracting forces to the TOT layers.

With a full table of reaction events and corresponding activation barriers, a kinetic monte carlo (KMC) model (compare Kurganskaya and Lutge 2016, Schabernack et al. 2021) that predicts dissolution phenomena of a multitude of clay minerals would be possible. Recently, a KMC study for the dissolution of quartz was published (Martin et al., 2021) showing how closely the activation energies can be simulated when choosing the right mechanism (step-by-step

dissolution). Missing data, like the activation barriers for the detachment of ions substituting the tetrahedral or octahedral sites (e.g. Mg, Fe) or the different possible topologies of the surface sites (e.g. kinks or steps), could help to complete the rate catalogue and further define a general dissolution model for clay minerals. This kind of model would reduce the calculation time drastically while maintaining a fairly accurate representation of the actual dissolution rates of clay minerals compared to the time-consuming *ab initio* simulations. If combined with the ion incorporation into the clay mineral or even crystal growth/precipitation reactions, the model could determine the duration of the entrapment of dangerous elements like heavy metals, toxic elements or radionuclides. The kinetic model would enable predictions of the time passing until the pollutants return into the environment. But still, the amount of different structural setups is large and requires detailed investigation and probably years of simulations to include all relevant system parameters.

The next steps towards a comprehensible model for the prediction of the reaction mechanisms and kinetics for clay minerals should be focused on:

1. Investigation of surface protonation and ion adsorption by titration Grand Canonical Monte Carlo simulations considering the ion strength and pH of the solution.
2. Use the surface structure obtained for AIMD (metadynamics) calculations to investigate the reaction mechanism for relevant terminal sites and topologies. Additionally, the activation barriers of the step-by-step process are calculated as well.
3. Compile a rate catalogue with the activation barriers of the AIMD simulations for the Kinetic Monte Carlo simulations of dissolution and precipitation.

6.1 References

- Amram K. and Ganor J. (2005) The combined effect of pH and temperature on smectite dissolution rate under acidic conditions. *Geochimica et Cosmochimica Acta* **69**, 2535–2546.
- Bosbach D., Charlet L., Bickmore B. and Hochella M. (2000) The dissolution of hectorite: In-situ, real-time observations using atomic force microscopy. *American Mineralogist* **85**, 1209–1216.
- Cappelli C., Yokoyama S., Cama J. and Huertas F. J. (2018) Montmorillonite dissolution kinetics: Experimental and reactive transport modeling interpretation. *Geochimica et Cosmochimica Acta* **227**, 96–122.
- Golubev S. V., Bauer A. and Pokrovsky O. S. (2006) Effect of pH and organic ligands on the kinetics of smectite dissolution at 25 degrees C. *Geochimica et Cosmochimica Acta* **70**, 4436–4451.
- Kurganskaya I. and Luttge A. (2016) Kinetic Monte Carlo Approach To Study Carbonate Dissolution. *Journal of physical Chemistry C* **120**, 6482–6492.
- Kuwahara Y. (2008) In situ observations of muscovite dissolution under alkaline conditions at 25-50 degrees C by AFM with an air/fluid heater system. *American Mineralogist* **93**, 1028–1033.
- Labbez C. and Jönsson B. (2007) A new Monte Carlo method for the titration of molecules and minerals. In *Applied parallel Computing: State of the Arte in scientific Computing* (eds. B. Kagstrom, E. Elmroth, J. Dongarra, and J. Wasniewski). Lecture Notes in Computer Science. High Comp Sci Ctr N; Umea Univ, Dept Comp Sci. p. 66.
- Li Y., Pan H., Liu Q., Ming X. and Li Z. (2022) Ab initio mechanism revealing for tricalcium silicate dissolution. *NATURE COMMUNICATIONS* **13**.
- Martin P., Gaitero J. J., Dolado J. S. and Manzano H. (2021) New Kinetic Monte Carlo Model to Study the Dissolution of Quartz. *ACS EARTH AND SPACE CHEMISTRY* **5**, 516–524.
- Marty N. C. M., Cama J., Sato T., Chino D., Villieras F., Razafitianamaharavo A., Brendle J., Giffaut E., Soler J. M., Gaucher E. C. and Tournassat C. (2011) Dissolution kinetics of synthetic Na-smectite. An integrated experimental approach. *Geochimica et Cosmochimica Acta* **75**, 5849–5864.
- Metz V., Amram K. and Ganor J. (2005) Stoichiometry of smectite dissolution reaction. *Geochimica et Cosmochimica Acta* **69**, 1755–1772.
- Oelkers E. H., Schott J., Gauthier J.-M. and Herrero-Roncal T. (2008) An experimental study of the dissolution mechanism and rates of muscovite. *Geochimica et Cosmochimica Acta* **72**, 4948–4961.
- Schabernack J., Kurganskaya I., Fischer C. and Luttge A. (2021) Influence of Muscovite (001) Surface Nanotopography on Radionuclide Adsorption Studied by Kinetic Monte Carlo Simulations. *MINERALS* **11**.

Acknowledgements

I want to thank all persons that were important for the creation and finalisation of this thesis. First of all, many thanks to Prof. Sergey Churakov and also Dr. Inna Kurganskaya for giving me the opportunity to work on this very intriguing and interesting project. They helped me getting into the topic fast and we had fruitful discussions, when I didn't know how to proceed.

I am also thankful to all the colleagues in the IfG as well as the DCB, that made me feel welcome in Bern. Especially my office mate Dr. Georgia Cametti, with whom I had a lot of discussions and a lot of fun. The same goes for Michelle, Fabio, Giulia, Rebecca, Francesco, Stefano, Lars, Fulvio, Florian, Konstantinos and all that I might have forgotten. My many visits to the PSI were very insightful as well and I also want to thank some of the people I met there, like Leonardo, Annamária, Philipp, Dan, Gregor, Bart and other PhD students and colleagues from the LES Team, that always organized very special social events like the yearly Muschelessen.

A big thanks goes to my external examiner Prof. Andrey Kalinichev, whom I first met at the International Clay Conference in Granada 2017, especially, for being patient with me and still coming to my defense. I am also thankful to Prof. Jörg Hermann for sitting as the chairman and Dr. Maria Marques Fernandez for being an examiner at my defense.

I am very grateful for my family (Jatzke and Schliemann) that always supported me and my decisions. And last, but most important to me, I am thankful for my wife Karoline, that was always believing in me, even when I was struggling or lost track. She was the one that kept pushing me and without her I wouldn't have come this far. To her goes the major part of my gratitude.

Erklärung

gemäss Art. 18 PromR Phil.-nat. 2019

Name/Vorname: Schliemann, René Jens

Matrikelnummer: 16-124-349

Studiengang: Erdwissenschaften

Bachelor

Master

Dissertation

Titel der Arbeit: Towards understanding the dissolution mechanism of clay minerals
– An ab initio simulations study

LeiterIn der Arbeit: Prof. Sergey Churakov

Ich erkläre hiermit, dass ich diese Arbeit selbständig verfasst und keine anderen als die angegebenen Quellen benutzt habe. Alle Stellen, die wörtlich oder sinn-gemäss aus Quellen entnommen wurden, habe ich als solche gekennzeichnet. Mir ist bekannt, dass andern-falls der Senat gemäss Artikel 36 Absatz 1 Buchstabe r des Gesetzes über die Universität vom 5. September 1996 und Artikel 69 des Universitätssta-tuts vom 7. Juni 2011 zum Entzug des Dokortitels be-rechtigt ist.

Für die Zwecke der Begutachtung und der Überprüfung der Einhaltung der Selbständigkeitserklärung bzw. der Reglemente betreffend Plagiate erteile ich der Univer-sität Bern das Recht, die dazu erforderlichen Perso-nendaten zu bearbeiten und Nutzungshandlungen vor-zunehmen, insbesondere die Doktorarbeit zu vervielfäl-tigen und dauerhaft in einer Datenbank zu speichern sowie diese zur Überprüfung von Arbeiten Dritter zu verwenden oder hierzu zur Verfügung zu stellen.

Dresden, der 18.11.22

Ort/Datum



Unterschrift